Ionic diodes based on cellulose nanocrystals (CNC) and related rheological studies

by
PARYA KEYVANI

B.Sc., Shahrekord University, 2010

M.Sc., Polytechnic University of Milan, 2015

A THESIS SUBMITTED IN PARTIAL FULFILLMENT
OF THE REQUIREMENTS FOR THE DEGREE OF

Doctor of Philosophy

in

THE FACULTY OF GRADUATE AND POSTDOCTORAL STUDIES

(Chemical and Biological Engineering)

THE UNIVERSITY OF BRITISH COLUMBIA
(Vancouver)

August 2021

The following individuals certify that they have read, and recommend to the Faculty of Graduate and Postdoctoral Studies for acceptance, the dissertation entitled:

Cellulose nanocrystalline (CNC) based ionic diodes and related CNC hydrogel rheological studies

submitted by Parya Keyvani in partial fulfillment of the requirements for

the degree of Doctor of Philosophy

in The Faculty of Graduate and Postdoctoral Studies

Examining Committee:

Savvas G. Hatzikiriakos, Chemical and Biological Engineering, UBC
Co-supervisor

Parisa Mehrkhodavandi, Chemistry, UBC
Co-supervisor

Vagelis Harmandir's, Mathematics and Applied Mathematics, University of Crete
External Examiner

Alireza Noje, Electrical and Computer Engineering, UBC
University Examiner

David P. Wilkinson, Chemical and Biological Engineering, UBC
University Examiner

Additional Supervisory Committee Members:

Elod Gyenge, Chemical and Biological Engineering, UBC
Supervisory Committee Member

Joerg Rottler, Physics and Astronomy, UBC
Supervisory Committee Member

Abstract

In this thesis, cellulose nanocrystals (CNC) fibers were chemically modified to produce anionic (pCNC) and cationic (nCNC) polyelectrolyte hydrogels to fabricate ionic diodes. In the beginning, the rheological behaviour of cationic and anionic CNC was studied and compared to that of pristine CNC. It was demonstrated that in the sonicated state, anionic and cationic CNC form hydrogen bonding, which notably contributes to interparticle forces and gel strengths. These structures between individual rods defeat the purpose of flocculation and ultimately leading to a more stable suspension. Moreover, enhanced rheological properties were observed in the case of nCNC in comparison with the pCNC and this may be due to the extensive formation of hydrogen bonding.

In addition, the surface-modified cellulose nanocrystals were used to fabricate ionic diodes. Rectification behaviour from two oppositely charged hydrogels doped with cellulose nanocrystals with positive and negative surface charges was observed. It was found that the current−voltage characteristics of the CNC−hydrogel diode are influenced by several parameters including gel thickness, hydrogel concentration, applied voltage, and scanning frequency. Pronounced rectification ratio and high current densities in forward bias occurred as a result of the high surface area followed by a high charge density.

Analyzing the experimental data, we demonstrated that unidirectional current response originated from an anisotropic distribution of counterions at the interface between the two gels doped with oppositely charged CNCs. Moreover, the physical mechanism is described quantitatively by an electrochemical model. We investigated and validated the proposed electrochemical mechanism by the Yamamoto-Doi model using experimental data. We demonstrated that the diode works via a physical mechanism that involves the electrochemical generation of hydroxyl ions and protons at the electrodes to create current. Exponential currents (J) in the forward bias were observed while $J = A\sqrt{-V}$ in the backward bias, which is in agreement with predictions of the electrochemical model proposed by Yamamoto-Doi [1]. The results of this thesis can be directly utilized to fabricate biodegradable diodes of good, stable rectification performance. Also, this work provides insight on how to control ionic movement in ionic devices.

Lay Summary

In this thesis, nanocrystalline cellulose (CNC) fibers were chemically modified to produce anionic (pCNC) and cationic (nCNC) polyelectrolyte hydrogels to fabricate ionic diodes. Ionic diodes are devices that allow the passage of ions in only one direction. The fabricated diodes demonstrated excellent performance in terms of reproducible results, high rectification ratio, and reliable performance. Finally, for the first time, the principles/mechanism of operation of the diodes was explained based on a theory developed by Yamamoto and Doi, which consequently was validated based on the experimental results of the present work.

Preface

Several portions of this thesis have been published as original manuscripts in peer-reviewed journals with Parya Keyvani as the primary author:

Chapter 3 Most of this chapter has been previously published as "Cationic and Anionic Cellulose Nanocrystalline (CNC) Hydrogels: A Rheological Study" **Parya Keyvani**, Kudzanai Nyamayaro, Parisa Mehrkhodavandi, Savvas G. Hatzikiriakos, Physics of Fluids 33.4 (2021): 043102 (shared first co-authorship with Kudzanai Nyamayaro).

Chapter 4 Most of this chapter has been previously published as "Toward Biodegradable Electronics: Ionic Diodes Based on a Cellulose Nanocrystal–Agarose Hydrogel" Kudzanai Nyamayaro, **Parya Keyvani,** Francesco D'Acierno, Jade Poisson, Zachary M. Hudson, Carl A. Michal, John D. W. Madden, Savvas G. Hatzikiriakos, and Parisa Mehrkhodavandi, *ACS Applied Materials & Interfaces* **2020** *12* (46), 52182-52191 DOI: 10.1021/acsami.0c15601 (shared first co-authorship with Kudzanai Nyamayaro). Jade Poisson and Prof Zachary M. Hudson helped with AFM analysis. Francesco D'Acierno and Prof Carl A. Michal did the NMR characterization.

Chapter 5 Most of this chapter has been previously published as "The rectification mechanism in polyelectrolyte gel diodes" Kudzanai Nyamayaro, Vasilii Triadafilidi, **Parya Keyvani**, Joerg Rottler, Parisa Mehrkhodavandi, Savvas G. Hatzikiriakos, Physics of Fluids 33.3 (2021): 032010. (shared first co-authorship with Kudzanai Nyamayaro and Vasilii Triadafilidi).

Some parts of experimental observations reported in chapter 4 were conducted in conjunction with one other University of British Columbia graduate student at the Chemistry Department, namely Kudzanai Nyamayaro. The synthesis and characterization (Zeta Potential, FITR, Titration, TGA, and XRD) of the structures were done by Kudzanai Nyamayaro. The AFM results were done by Jade Poisson.

Some parts of chapter 5 were conducted in conjunction with Vasilii Triandafilidi, a graduate student at the Department of Chemical and Biological Engineering at the University of British Columbia. The data were analyzed and compared with theoretical models by Vasilii Triandafilidi. All work was supervised by Dr. Savvas G. Hatzikiriakos and Dr. Parisa Mehrkhodavandi.

Table of contents

List of Tables

List of Figures

List of Symbols

C_d	Capacitance (F)
C_d	Capacitance (F)
D	Diffusion constant (m/s)
D	Diffusion constant (m/s)
G"	Loss modulus (Pa)
G"	Loss modulus (Pa)
G'	Storage modulus (Pa)
G'	Storage modulus (Pa)
I	Electric Current density (A/m^2)
I	Electric Current density (A/m^2)
J	Exponential Current density (A/m^2)
J	Exponential Current density (A/m^2)
k_B	Boltzmann constant (m^2kg/s^2k)
k_B	Boltzmann constant (m^2kg/s^2k)
R_p	Polarization resistance ($\mu A/cm^2$)
R_p	Polarization resistance ($\mu A/cm^2$)
R_s	Solution resistance (S/m)
R_s	Solution resistance (S/m)
T	Temperature (°C)
T	Temperature (°C)
V	Voltage (V)
V	Voltage (V)
Z'	Real part of impedance (Ω)
Z'	Real part of impedance (Ω)

Z"	Imaginary part of impedance (Ω)
Z"	Imaginary part of impedance (Ω)

Greek Letters

$\dot{\gamma}$	Shear rate (s^{-1})
λ_D	Debye length (m)
η	Shear viscosity (Pa. s)
$\eta*$	Complex viscosity (Pa. s)
ξ	Zeta potential (mV)
ω	Angular frequency (rad/s)

Abbreviations

AC	Alternating Current
AFM	Atomic Force Microscopy
AG	Agarose
CNC	Cellulose Nanocrystal
DC	Direct Current
DI	De-Ionized
EIS	Electrochemical Impedance Spectroscopy
FTIR	Fourier Transform Infrared Spectroscopy
GTMAC	Glycidyltrimethylammonium chloride
ITO	Indium Tin Oxide
MD	Molecular Dynamic
MFC	Microfibrillated Cellulose

nCNC	Cationic Cellulose Nanocrystal
NMR	Nuclear Magnetic Resonance
pCNC	Anionic Cellulose Nanocrystal
PDAC	Poly(diallyldimethylammonium chloride)
PDMS	Polydimethylsiloxane
PE	Polyelectrolyte
PGD	Polyelectrolyte Gel Diode
PS	Poisson-Boltzmann
PSS	Poly(styrene sulfonate
TGA	Thermal Gravimetric Analysis
XRD	X-Ray Diffraction

Acknowledgments

First and foremost, I would like to sincerely thank my supervisor, Professor Savvas G. Hatzikiriakos for believing in me, introducing me to a fascinating research area, and providing me with work that has been important for my future career. I appreciate the continuous support, encouragement, and guidance he has given me over these years. I consider myself extremely lucky to benefit from his supervision as well as his mentorship.

It is my pleasure to acknowledge my co-supervisor, Professor Parisa Mehrkhodavandi for all of the useful discussions, for her kindness and encouragement.

I would like to take this opportunity to express my sincere gratitude to Professor John D. Madden for his constant help and support during these past three years.

I would also like to thank my supervisory committee members, Professor Elod Gyenge, and Professor Joerg Rottler for their insightful comments, helpful discussions, and guidance during these years.

I would like to acknowledge my research colleague Kudzanai Nyamayaro for his excellent cooperation and dedication towards the work. It has been my pleasure to work with and learn from him. Also, have him as my friend.

Working in the Rheology Laboratory and Advanced Materials Process Engineering Laboratory has been a privilege and I would like to thank all my colleagues for making these labs an inspiring and enjoyable place to work.

I would like to thank my dear friends Sara and Shamila who were available for me whenever I needed them.

From the bottom of my heart, I thank my dear friend, Nikoo who helped me as much as she could; for listening to my frustrations and celebrating my successes.

And finally, my most loving thanks to those who matter to me the most, my mother, Mehry, my sisters, Bahar, and Ghazal, and my niece, Parmin.

Dedication

This dissertation is dedicated to

My mother, Mehry, for her support, encouragement, and unconditional love

Chapter 1: Introduction

Nowadays, electronics have become a part of human life and due to constant technological advancement, large amounts of electronic waste are continually produced.[2] Thus, we need to make use of resources that are renewable and sustainable. The use of bioderived polymers to manufacture functional and sustainable material for advanced applications is an attractive approach to meet the need for light, flexible, biocompatible, and biodegradable[2] electronics such as ionotronics.[3]

Ionotronics are a class of electronics that are made from soft polymers and employ ions as charge carriers. These types of devices have been envisioned for bio-integratable devices. The materials that have previously been used to fabricate iontronic devices are anionic poly(styrene sulfonate) (PSS) and cationic poly(diallyldimethylammonium chloride) (PDAC), examples of olefin-based polymers.[4] However, they are not environmentally safe. As a result, biopolymers can be considered as an excellent solution. Cellulose is the most abundant natural polymer with unique mechanical properties, shape flexibility, and particularly biodegradability.[5]

These characteristics have enabled the incorporation of cellulosic material into flexible electronics as flexible and transparent substrates, electrolytes, wearable bioelectronics, ionic-electronic conductors, sensors, and conductive transistors. [5,6] However, cellulose mainly has been used as a substrate in these devices since it is nonconductive and has rarely served as the active component in the device. Cellulose can be tailored to obtain the desired functionality through modification of its surface hydroxyl groups. This approach has been previously employed to fabricate an ionic diode paper made from two oppositely charged microfibrillated cellulose (MFC) layers.[7] However, to achieve rectification ratios of ∼15 (cf. ∼40 for PSS/PDAC−AG diode), the MFC diode used up to 50wt% of cellulose.[4] We aimed to enhance these results using cellulose nanocrystals (CNCs), a highly crystalline form of cellulose with interesting mechanical properties, nanoscale dimensions, tremendous rigidity, and large surface area to fabricate biodegradable electronic diodes with properties approaching those of polyolefin-based analogues.[4]

In this work, a diode was fabricated by combining the attractive properties of CNCs and hydrogels. Chemical modification of cellulose nanocrystal was carried out on the hydroxyl groups on the crystalline backbone of CNCs to produce cationic (nCNC) and anionic (pCNC) cellulose

nanocrystals. The synthesized nCNC and pCNC were incorporated into an agarose matrix to form stable and mechanically strong hydrogels. We showed that ionic diodes, created from low quantities of a high surface area composed of two slabs of p- and nCNC-doped agarose hydrogels, outperformed both the PSS/PDAC−AG and the MFC diodes.

Based on experimental data, rectification is achieved when there is an anisotropic distribution of anionic and cationic counterions between two oppositely gels. Additionally, the mechanism was explained quantitatively through an electrochemical model. Here, we compared and verified the electrochemical model proposed by the Yamamoto-Doi by using our experimental data.[1] Our findings confirmed that the ionic diode operates via a physical mechanism that involves generation of proton and hydroxyl ions at the electrodes to create current. In the forward regime, exponential currents (J) were observed while $J = A\sqrt{-V}$ (A is a proportionality constant and V is the potential) in the backward bias, which is in agreement with predictions of the electrochemical model proposed by Yamamoto-Doi.[8] Moreover, based on the electrochemical model, we also confirmed that current in the backward bias depends on the dopant concentration.

Furthermore, to extend our investigation as well as to have more insight into the performance of the diode, rheological properties of cationic and anionic CNC hydrogels in relation to unmodified CNC suspensions were studied. The rheological properties of CNC suspensions have been extensively studied[9-10], in the presence of electrolytes [11,10] and surfactants. [12,13] However, few studies exist on the rheological behavior of anionic and cationic CNC hydrogels, especially when it comes to unmodified CNC suspensions [14]. In the present work, we also investigated the effect of concentration and ultrasound treatment on the microstructure and rheological response of these CNC suspensions. Herein, we attempted to explain how the anions and cations affect the rheological properties as they are expected to affect the double layers formed around the CNC particles differently.

In summary, the main objective of this work is to fabricate a diode based on CNC and to optimise its performance by varying the concentration of the CNC hydrogels (positive and negative), the applied voltage, and the mechanical and rheological properties of the various hydrogels used (details of the objectives can be found in section 1.2)

1.1 Literature Review

1.1.1 Structure of Cellulose

Cellulose is found as the main structural component of plant cell walls. Moreover, it is also present in living species such as algae, bacteria and tunicates.[5] Cellulose is a linear homopolysaccharide composed of repeating units of β-D-glucopyranose molecules that are covalently bound by glycosidic bonds (Figure 1.1). Due to the presence of three hydroxyl groups on each of the monomers, the chains associate through hydrogen bonding. The extensive van der Waals forces and hydrogen bonding induce parallel stacking of the cellulose chains. This stacking results in formations of fibrillar and semicrystalline packing in the hierarchical structure.[15]

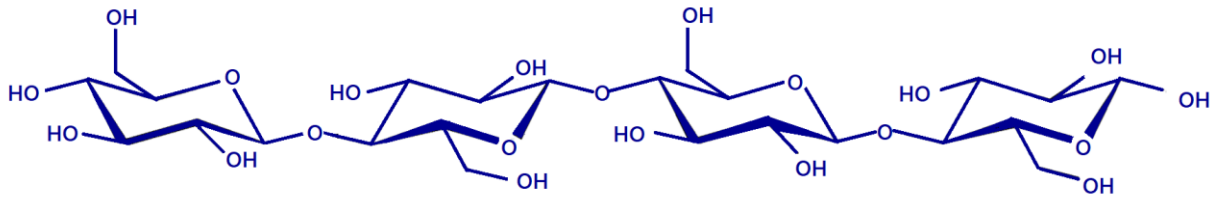

Figure 1. 1 Chemical structure of cellulose

1.1.2 Prepration of cellulose nanocrystals (CNC)

Cellulose nanocrystals can be produced by the isolation of CNCs from cellulose fibers through acid hydrolysis. Disordered or amorphous regions of cellulose are preferentially attacked, while crystalline regions remain intact due to higher resistance to acid attack (Figure 1.2).[15] These rod-shaped crystallites are shorter and stiffer particles than the microfibrils are called cellulose nanocrystal. They also sometimes referred to as nano-rods or whiskers. [9]

For cellulose fibre production, typically hydrolysis with sulfuric acid (H_2SO_4) is used. This results into crystalline particles with anionic sulfur half ester groups on their surfaces, which ultimately leads to colloidal stability and dispersion in water.[16,17] Different acids can be used for isolation of cellulose nanocrystals, while the most common type of acid is sulphuric acid. Other researchers investigated the use of different types of acids like hydrochloric acid, hydrobromic acid, and phosphoric acid,[18–21] which generally result in less stable suspension due to lack of surface charges on the produced CNC fibers, thus tending to aggregate.[22]

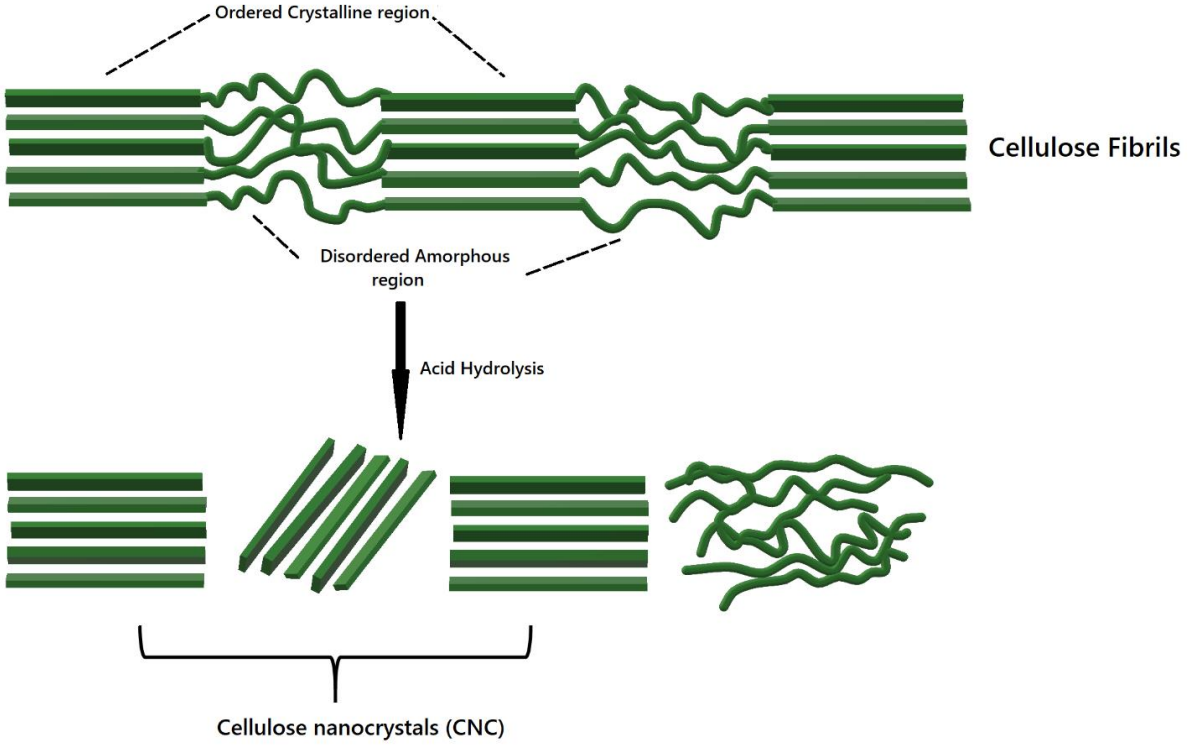

Figure 1. 2 Part of a cellulose fibers where the ordered crystalline and amorphous regions are shown. Acid hydrolysis removes the non-crystalline regions and crystalline parts stay intact (CNC).

1.1.2.1 Surface modification of CNCs

Depending on the desired application, chemical functionalization of cellulose nanocrystals can be conducted at the hydroxyl groups at the surface of CNCs. It is noted that CNCs possess an abundance of hydroxyl groups at their surface. In general surface modification can be classified into sulfonation [23], oxidation[24], silylation [25] , cationization[26], polymer grafting.[27]

The main challenge for the surface modification of CNCs is to carry out the process in a way that only changes the surface of CNCs, while maintaining the original morphology to avoid any polymorphic conversion and to preserve the integrity of the crystal. [28]

1.1.3 Applications of CNC

Figure 1.3 lists several applications for CNC, which are possible due to their interesting mechanical, morphological, optical and rheological properties as well as their high surface area and colloidal stability.[16] Two other important characteristics of cellulose nanocrystals are

biodegradability and biocompatibility that makes their use attractive in many applications as already discussed. These two factors are making CNCs a good candidate for biomedical applications as nanofillers in tissue engineering and carriers in drug delivery. [29,30]

Aqueous solution at certain concentrations of CNCs are able to form chiral nematic ordered phases in concentrated suspensions (discussed in the next section at it is relevant to the present work). Films with optical properties of chiral nematic liquid crystals can be prepared by casting CNC on the cellulosic surfaces. These films provide examples of some current security applications including certificates, passports and security papers.[31]

Another interesting application of CNC is in iontronic systems such as fabrication of sensors, actuators, capacitors and diodes (more details in later section). [32–34]

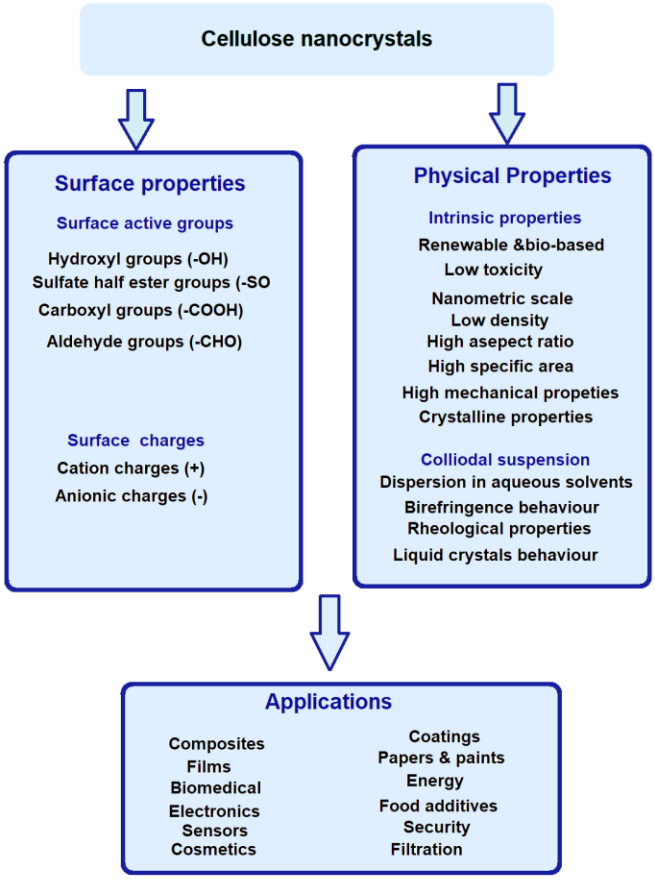

Figure 1. 3 Surface and physical properties of cellulose nanocrystals and their applications

1.1.4 Rheology of CNC

The rheological response of CNC suspensions depends on various parameters including microstructure, concentration, surface charge and the interaction between rods and the solvent or matrix in a composite system. Therefore, by changing morphology and composition of suspensions, their resistance to flow or viscosity will be affected. [15]

Many researchers have investigated the rheological properties of cellulose nanocrystals through studying the CNC microstructure change, and understanding the challenges during processing, handling, and applications.[35,36] In 1961, Marchessault was the first one who demonstrated the hydrodynamic properties of the CNCs and directly related its rheological properties to the size and length distributions of the particles in aqueous solutions.[37] Then, in 1980 Onogi and Asada [38] showed three distinct regions in the viscosity profile of liquid crystalline polymers in solution. These results were reproduced for unsonicated suspensions.[9,38,39]

This three-region viscosity profile is depicted in Figure 1.4. These three regions are typical of lyotropic liquid crystals. In the first region, the shear rates are low enough to continue reduction in viscosity with shear rate due to the alignment of the chiral nematic liquid crystal domains. Region (II) appears at intermediate shear rates, where under the influence of shear all the domains have been aligned along the shear direction. Finally, region (III) appears at high shear rates and represent a second shear thinning behaviour. This may due to the distortion of the liquid crystal domains and orientation of individual rods along the shear flow as the applied shear stress/shear rate increases.[9,38]

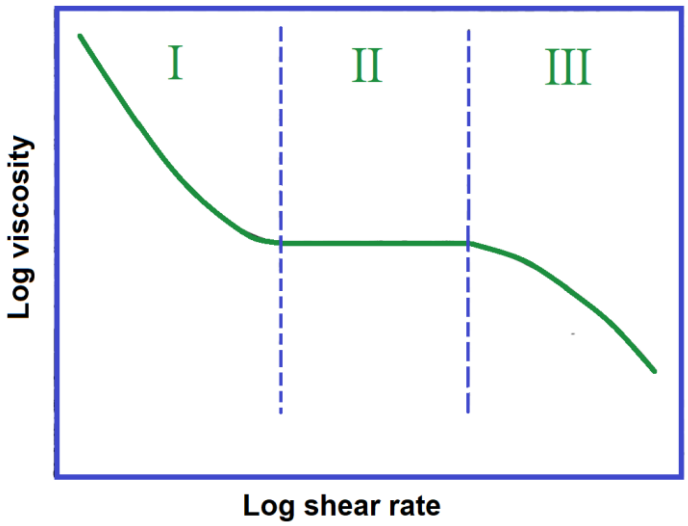

Figure 1. 4 The typical graph for the apparent viscosity as a function of shear rate for liquid crystals

Figure 1.5 shows the effect of concentration on the viscosity profile of the CNC aqueous solutions. At low concentrations, the three-region viscosity profile is observed (1 to 4wt.%). As the concentration increases the three regions are no longer observed. Instead, for 5 to 7wt% only a single shear thinning behavior region is observed over the entire range of shear rate. It is worthwhile to note that by increasing the concentration from 1wt% to 7wt%, the viscosity in the low shear regime increases by 10^4. This points out to the high sensitivity of the rheological properties on concentration, an observation that plays a significant role in optimizing the performance of electronic devices such as diodes that are fabricated in the present work.

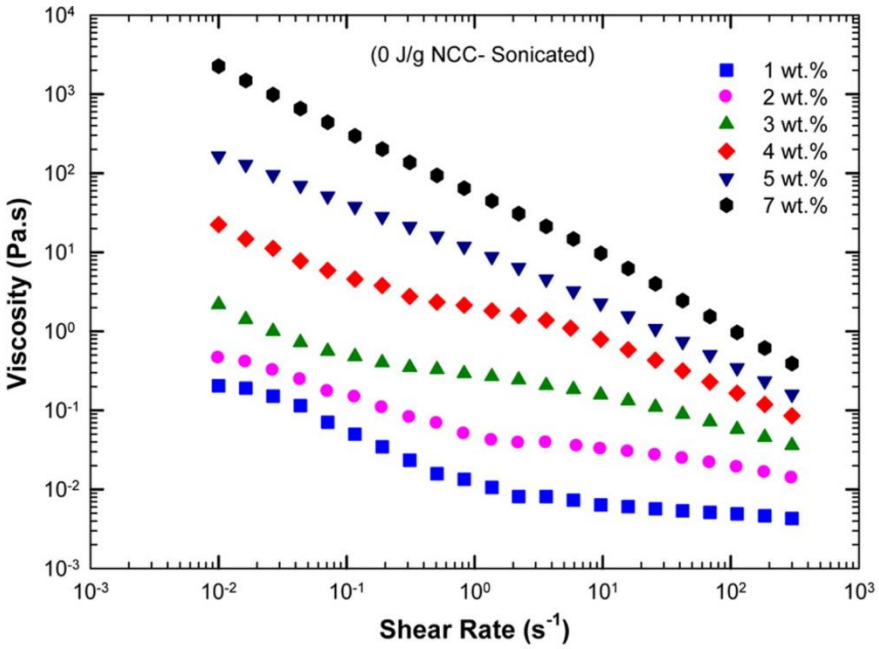

Figure 1. 5 Steady-state viscosity versus shear rate for aqueous solution of CNC at different concentrations [10]

1.1.5 Iontronics

In this section, the unique features of iontronics and their various applications will be discussed. In iontronics, the performance of the system relies on the migration of ions.[40] Ions are transported through ionically conductive solutions due to an applied electric voltage between electrodes. The ionic conductors form the foundation of diodes, transistors and resistors.[41]

1.1.5.1 Ionic conduction

In ionic devices, anions and cations perform similar functions as electrons and holes in electronics.[42] Ionic transport which occurs by applying electric fields is referred to as ionic conduction. In an artificial system the ionic current can be generated by electric fields, while in biological systems the vast majority of signaling is caused by gradients of concentration.[40]

Mainly, there are two-phase matrices for ionic systems, namely solid and liquid. In the case of solid-state ionics, ceramic compounds like ionic crystals enable the displacement of ions. However, in liquid-phase matrices, such as polar solvents (water, dimethyl sulfoxide), and ionic

liquids, ions migrate at nearly room temperature. Ionic-conductive hydrogels (the subject of the present work) behave like ionic liquid-phase conductors.

1.1.5.2 Adaptability to Biointegration

Conventional electronic devices are demonstrated by metals and semiconductors, which are stiff and brittle. However, ionic devices can be produced from various types of soft materials (polymers and gels) with ion conductivity. Through the adoption of flexible and stretchable ionic conductors, soft ionic devices can be developed.[4,43,44] Furthermore, ionic devices that are adaptable to bio-integration can likely be developed using biocompatible materials which can be used for implants in the medical sector.

1.1.6 Types of Ionic Conductions

In iontronic, anions and cations are the charge carriers instead of electrons as discussed. Lee [40] categorize two forms of ionic conduction, depending on aspects of ionic currents in media, namely "non-restrictive ionic conduction" and "selective ionic conduction". The former is the typical electrolyte-base system, where both cations and anions can pass through the media. In selective ionic conduction, only one type of ions transport is realized due to applied voltage.

1.1.6.1 Non-restrictive ionic conduction

In non-restrictive ionic conduction, there is no barrier to prevent the movement of ions. When a mixture of different ions dispersed into a polar solvent like water promotes the production of electrically conducting solution, this is referred to as electrolyte. Therefore, due to the existence of floating cations and anions in an electrolyte, upon applying a voltage, ions migrate toward the cathode and anode with different signs respectively. (Figure 1.6a).

1.1.6.2 Selective ionic conduction

Ion selectivity is another noticeable characteristic used in ionic devices. Ionic selective materials are composed of fixed charged polycationic or polyanionic molecular chains in addition to their mobile counter ions to satisfy charge neutrality[40] (Figure 1.6b). Ion-selective membranes (network

of the entangled polymeric chains) have a broad range of applications including electro-deionization and energy harvesting devices.

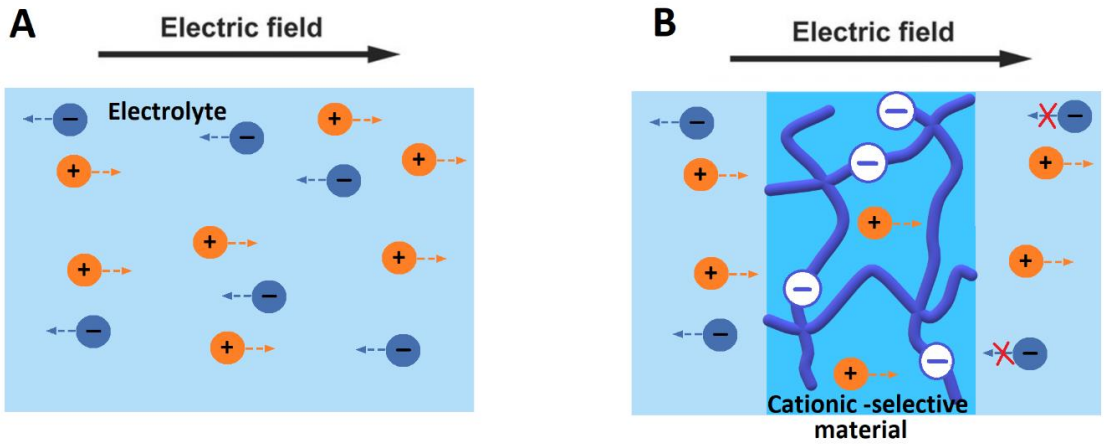

Figure 1. 6 Two different types of ionic conduction

1.1.7 Ionically Conductive Hydrogels

1.1.7.1 Gels as ionic conductors

Ionic conductors are classified into two categories, namely, liquid and solid types. Ionic liquids and electrolyte solutions are the most representative examples of liquid-type ionic conductors. Despite the faster response of ionic liquid and electrolyte solutions in comparison to solid ionic conductors, the "liquid" nature itself would be a strong challenge for their use in the fabrication of devices due to the possibility of evaporation.[45] Employing a mold is essential for the manufacturing of liquid ionic conductors to maintain their shapes (Figure 1.7a). Unlike liquid ionic conductors, a solid-phase electrolyte is dimensionally stable and easier to fabricate (Figure 1.7b).

Hydrogels are a promising class of materials for the manufacturing of future bioelectronic applications due to their ionic conductivity together with other properties such as stretchability, flexibility, optical transparency. [46] A hydrogel is a 3D network of polymeric chains with a high level of water content, whose mechanical properties result from the crosslinked polymer network. Although they exhibit fluid-like (in fact viscoelastic) properties, they can retain their shape in polymeric networks. Therefore, they are distinguishable from purely liquid-phase electrolytes.[46] Mechanical properties of hydrogels are affected by various factors, mainly the type of raw

materials, including monomers, their amounts as well as the synthesis method. Moreover, the mechanical properties of hydrogels are affected by various factors, mainly the type of the raw materials, their mounts as well as the synthesis methods.[40]

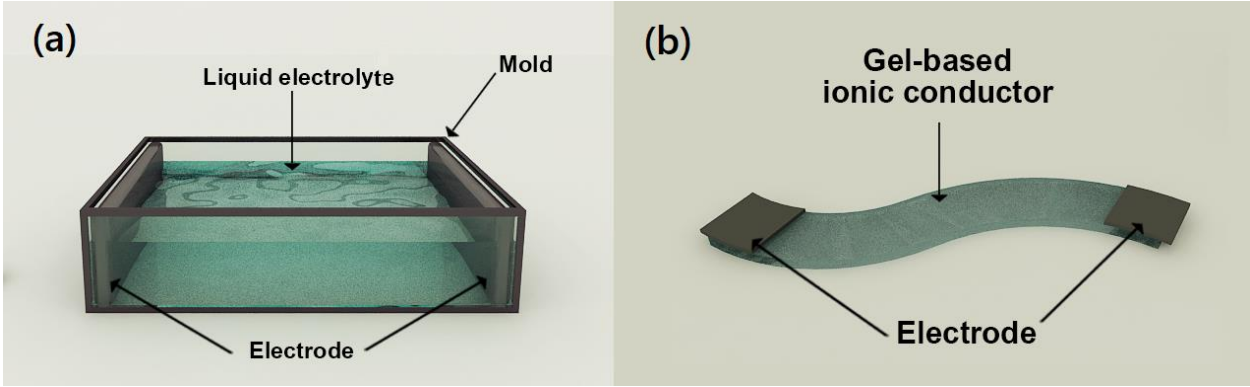

Figure 1. 7 Gels for stretchable Iontronics. A) liquid electrolyte ionic conduction. B) Ionic conductor based on a gel

1.1.8.1 Dehydration of hydrogels

One of the requirements for hydrogels is the storage of a large amount of water while maintaining their structure. This is essential due to the dependency of mechanical and ionic conductivity of the hydrogel to water. Hydrogels have the tendency to absorb and retain water in a dry environment or under shear stress. To maintain the 3D network structure as well as to prevent dehydration of hydrogels different techniques at the material and device level have been employed. Hygroscopic elements such as glycerol, salt, sugar, and cellulose are able to retain water in dry environments. Also, silane coupling agents let the thin elastomeric coating keep moisture.[46]

1.1.9 Ionic diodes

To fabricate iontronic devices (diodes), anions and cations should be asymmetrically distributed in the system. To achieve this, charged nonporous structures are used e.g., polyelectrolytes. Cations and anions selectively flow through structures. A two-layer stack containing polyanions and polycation is referred to as a bipolar membrane (BM). Bipolar membrane (BM) was first

proposed by Frilette in 1956 [47]. Like semiconductors, such structures act as rectifiers of current. [3,41,48]

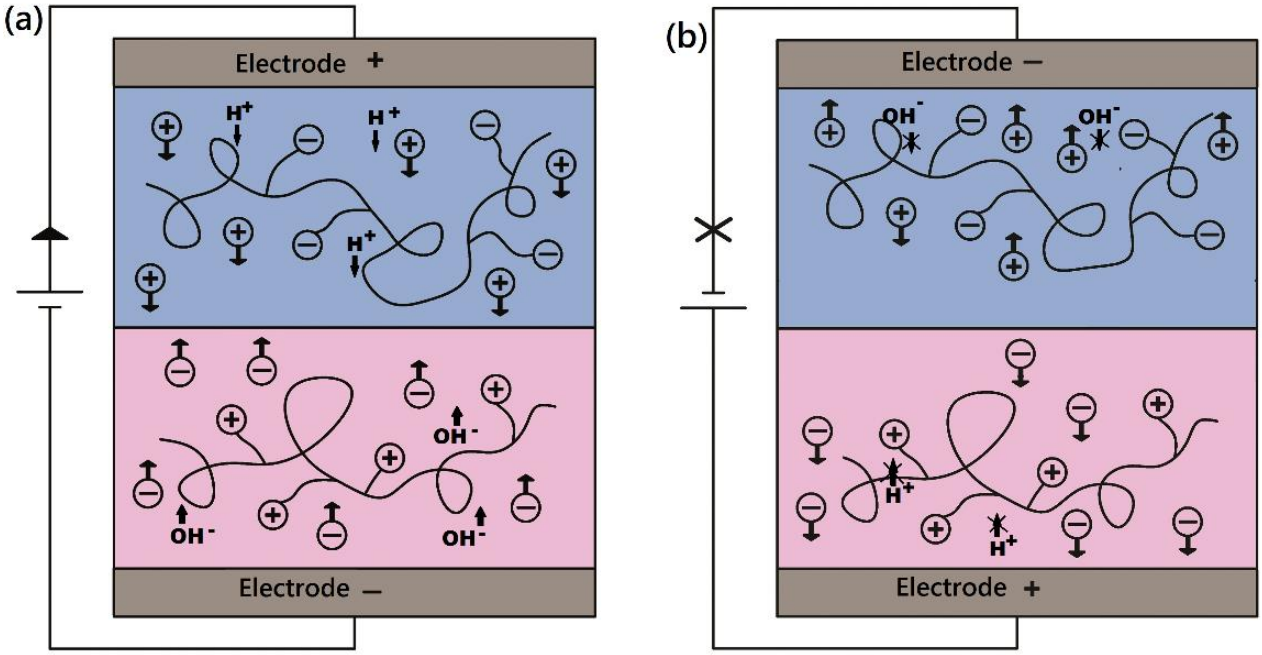

Figure 1. 8 Schematic representation of working principle of ionic diode. (a) In forward (b) backward regime

In forward bias, charged carriers at both sides of the diode move toward the junction (Figure 1.8a) located in the middle. Polarity change at the junction inhibits mobile ions from crossing the junction into the oppositely charged layers and therefore results in an accumulation of ions at the junction. However, due to the increase of the ion concentration at the junction, some cations and anions cross into the other side. In backward bias, (Figure 1.8b) the counter ions move to the nearest electrode, away from the junction. In this manner, the BM works as an iontronic diode.[41]

1.1.9.1 Fundamentals of the iontronic modulation process

Iontronics is a term used for the technology that electronic functions are controlled by the movement of ions. In general, the operation of the iontronic fields and responses are explained through three types of processes (Figure 1.9): 1) electrochemical reaction 2) formation of electrical double layer (EDL) 3) ion diffusion. [49]

1.1.9.1.1 Electrochemical reaction

Ions are massive particles, and their transport can be considered as a form of mass transfer. By applying a voltage, an electrostatic potential gradient is created which controls the ion transfer. An electrochemical reaction can happen when the applied voltage is above the electrochemical window. Electrochemical reactions occur at the interface between electrodes and ionic media.[40]

1.1.9.1.2 Electrical Double Layer (EDL)

Ionic current injected at the electrode-electrolyte interface can be divided into two major categories: Faradaic and capacitive processes i) Faradaic process involves direct electron transfer across an interface (surface-confined electrochemical reactions). The electrochemical oxidation and reduction reactions can occur between species in solution and solid or solid-solid reactions. [50,46] ii) Capacitive involves accumulation of oppositely charge carrier in the conductor and capacitive charge injections work based on charging and discharging of the electrode-electrolyte interface.[46] In most bioelectronic devices, Faradaic currents are undesirable since this mechanism inevitably involves oxidation and reduction of electrodes leading to a change in the chemical composition of the electrolyte and may create toxic by-products.[48]

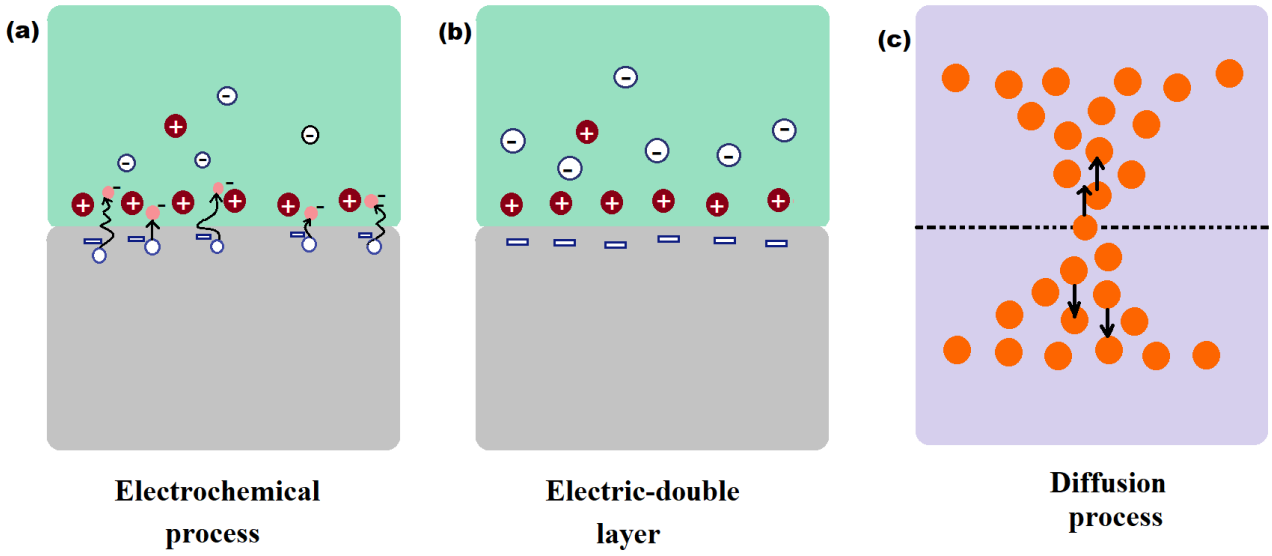

Figure 1. 9 Schematic representation of iontronic processes: a) electrochemical process, (b) electric-double-layer (EDL) formation, and (c) diffusion process.

The mechanism of the majority of hydrogel iontronic devices relies on the non-Faradaic coupling between mobile ions and mobile electrons.[51] Most conductors in contact with the electrolyte acquire electronic charges on their surfaces to maintain their charge neutrality. The attracted electrons and ions form an electrical double layer at the interface (EDL) (Figures 1.9b and 1.10). The electrical double layer acts as a capacitor [40]

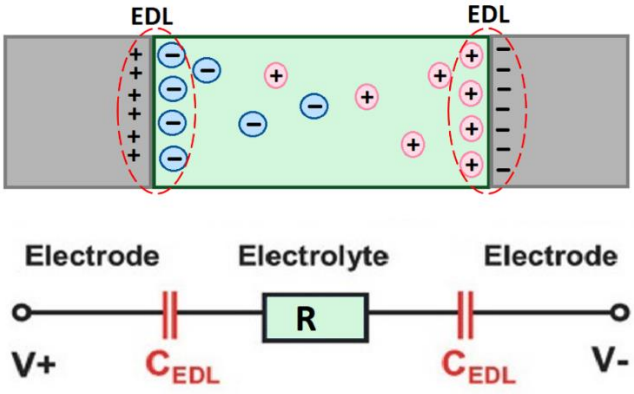

Figure 1. 10 The electrical double layer (EDL) forms at the interface of the electrolyte and electrode. The EDL acts like a capacitor

The real structure of the double layer is more complicated than the simple form which is presented in Figure 1.10. A more accurate schematic view is shown in Figure 1.11. Water molecules surrounded the ions in the solution form a solvent sheath or a hydration layer. Water molecules are polar and due to their dipole nature, they tend to align at the interface. The inner Helmholtz plane (IHP) is the plane of the centers of molecules or ions that are adsorbed directly to the surface of the electrode. This may happen due to van der Waals and Coulombic interactions. The outer Helmholtz plane (OHP) corresponds to the location of fully hydrated ions associated with the surface, where the solvent sheath prevents adsorption. The last part of the double layer is referred to as the diffuse double layer. It is made of free ions that move in the medium under the influence of Brownian motion and Coulombic forces.[52]

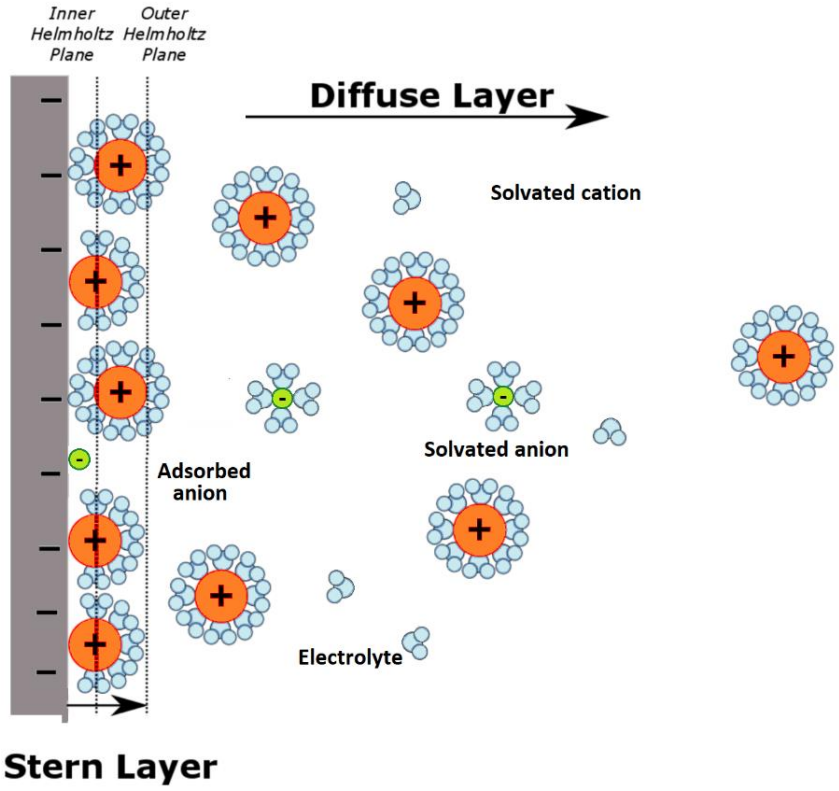

Figure 1. 11 Detailed structure of the electrical double layer

1.1.9.1.3 Diffusion

The process of transport of ions is divided into three different mechanisms i.e., diffusion, migration, and convection. ((Figure 1.12). Diffusion can occur through transport across the membrane due to a concentration gradient. Diffusion is known as passive transport since it does not require an external source of energy to move charged particles. Diffusion is attributed to the thermally activated Brownian motion of the molecules. Migration is defined as the movement of ions in the presence of an applied electric field and is known as active transport. The last contribution is from the bulk movement of the electrolyte known as convection (Figure 1.12).

As mentioned, diffusion is the movement of molecules or ions from a region of a greater concentration to a region with a lower concentration. The simplest description of diffusion is by Fick's first law of diffusion

$$J = -D\nabla C \qquad (1.1)$$

Where *C* is the concentration of the diffusing particles, *J* is the molar flux (concentration per square meter per second), and *D* is the diffusion coefficient, which has units of m^2 /s.[52]

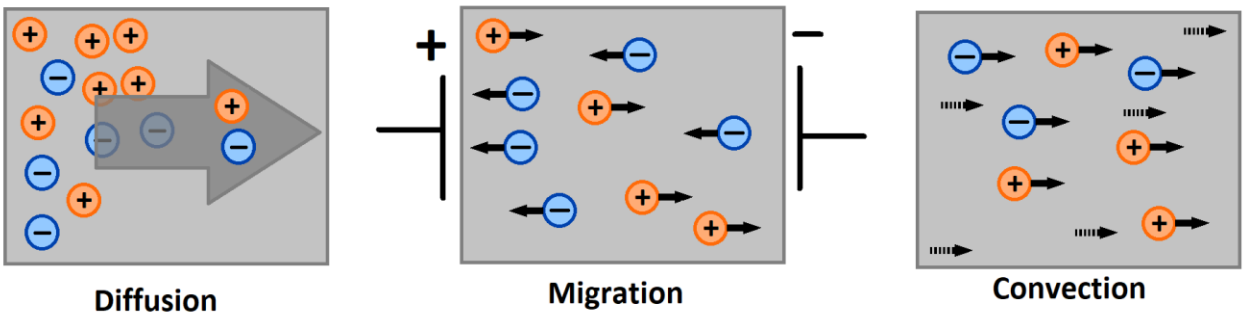

Figure 1. 12 Three modes ion transport for an electrochemical system: a) passive transport due to concentration gradient (diffusion) b) active transport due to an electric field (migration) , c) and convection that is defined as the movement of ions in a fluid

Mobility (μ) is the ability of ion transport through an electrolyte when an electric field is applied. Mobility can be defined by equation (1.2).

$$\mu = V_d/E \tag{1.2}$$

Where V_d is the drift velocity (unis in SI m/s) and E is the electric field (V/m).

The mobility of charges in an ionic solution and diffusion is directly related by the Einstein relation

$$D = \mu K_B T \tag{1.3}$$

Where K_B represents the Boltzmann's constant and *T* is the absolute temperature in Kelvin.

Collecting all data, a general expression for the flux of charged species *i* includes contributions from migration, diffusion, and convection, an equation known as the Nernst-Planck equation

$$N_i = \underbrace{-z_i\mu_i F c_i \nabla\emptyset}_{migration} \underbrace{- D_i \nabla c_i}_{diffusion} + \underbrace{c_i V}_{convection} \tag{1.4}$$

Where for species i the force caused by the applied electric field is equal to $-z_i F \nabla \emptyset$ and z_i is defined as a charge on a species and can be either positive or negative.[52]

1.2 Objectives and Thesis Organization

1.2.1 Objectives

The main objective of this research is to develop/fabricate CNC-based polyelectrolyte diodes using two oppositely charged cellulose nanocrystals.

The detailed objectives of this Ph.D. study include:

- Characterize the newly synthesized modified cellulose nanocrystals in the Chemistry Department (UBC) having positive and negative counter ions using various analytical techniques.
- Study the rheological properties of various CNC hydrogels used in the fabrication of diodes to understand effective/optimum ways of their gelation. Fabricate and investigate the performance of flexible and stretchable diode composed of modified cellulose nanocrystals.
- Investigate the performance of diodes in terms of maximizing their rectification. Therefore, the current response as a function of the applied voltage for different concentrations of pCNC and nCNC will be assessed. The effects of thickness of each layer of the diode and sweep scan rates on the diode will be studied to optimize their performance.
- Investigate the rectifying behavior of the gel diodes under AC signal of different frequencies and different applied voltage.
- Investigate the principles/mechanism of diode function based on a theory developed by Yamamoto and Doi.

1.2.2 Thesis organization

This thesis is organized as follows. Chapter 1 is a brief introduction to the subject of the present work that is diodes and their significance. It also briefly discusses the significance of polyelectrolyte hydrogel (PG) in different research fields and their adaptability to various applications. It also discusses the properties of hydrogels and CNCs as PGs to fabricate a

biodegradable fixed rectifying junction. This discussion naturally leads to the basic motivation of this research. Section 1.1 consists of a thorough literature review on previously reported research conducted on the use of CNCs, their surface modifications, and their applications in different technological areas. Section 1.1 also includes a detailed discussion of iontronic devices and the fundamentals of their function. The objectives and organization of the thesis are discussed in section 1.2. This is followed by chapter 2 that describes the materials and methodologies used to prepare and investigate the bridgeable diodes and the related rheological behavior of modified CNC. In chapter 3, the rheological behavior of cellulose nanocrystals (CNCs), anionic CNCs (pCNCs), and cationic CNCs (nCNCs), was comparatively studied using several different rheological tests. The focus of chapter 4 is on the fabrication of the ionic diodes based on Cellulose Nanocrystal−Agarose Hydrogels. Their fabrication process is described and the resultant current response when voltage is applied in terms of different concentrations of modified CNCs, different diode thicknesses, and different sweep scan rates are discussed in detail. Chapter 5 discusses the experimental finding and validation of the experimental data using the Yamamoto-Doi theory.[1] The conclusions and significance of this research work are summarized in chapter 6. Recommendations for future work are also presented in chapter 6.

Chapter2: Materials and Methods

2.1 Materials

Cellulose nanocrystals were purchased from CelluForce (Montreal, Quebec, Canada) in the form of sprayed dried sodium salts (CNC- Na^+). The sulfur content was reported 0.89 % by a supplier, with the particle size and the average hydrodynamic diameter 1-50µm (powder) and 70 nm respectively. Indium tin oxide (ITO)-coated glass electrodes (2.5 × 2.5 × 1.1 mm^3 with surface resistivity of (8 Ω sq^{-1}), Glycidyl trimethylammonium chloride (GTMAC), sodium hydroxide, sodium periodate, agarose (AG) (type I, low EEO), and silver nitrate were provided from Sigma-Aldrich. Sodium bisulfate was purchased from Fischer. All compounds were used as received without any further purification.

2.2. Sample preparation

2.2.1 Synthesis of n-Type CNCs

Cationic CNCs (nCNCs) were synthesized by Kudzanai Nyamayaro from the Chemistry Department at UBC. The process of synthesis is a modified methodology.[26,53] CNCs (5 g) were dispersed into 30 mL of 1.5 M NaOH and then stirred at room temperature for 30 min. Glycidyl trimethylammonium chloride (3 mol equivalent per anhydroglucose unit (AGU)) was added, and the reaction mixture was stirred at 85 °C for 6 h. After the reaction was complete, the excess NaOH was neutralized using HCl; the product was washed, isolated by centrifugation, and dialyzed against distilled water for 3 days.

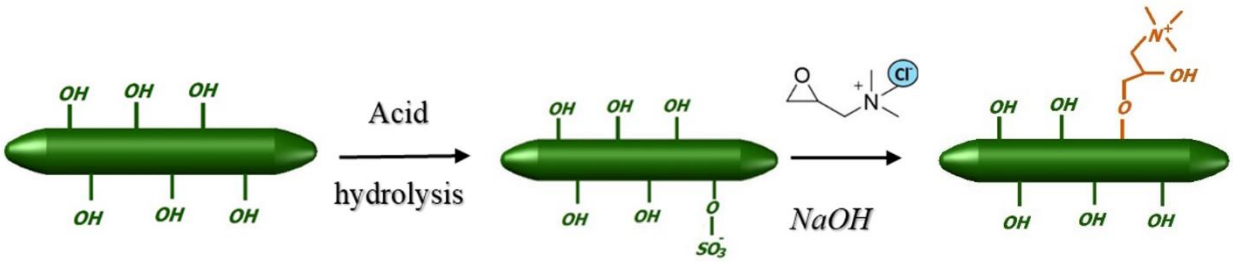

Figure 2. 1 Schematic illustration of synthesis of cationic CNC (nCNC)

2.2.2 Synthesis of p-Type CNCs

Anionic CNCs (pCNC) were synthesized with two different routes by Kudzanai Nyamayaro from the Chemistry Department at UBC. These are discussed below and shown schematically in Figures 2.2 and 2.3.

The first route including a two-step reaction.[54] Initially, CNCs were oxidized by sodium periodate; CNCs (5 g) were dispersed in 200 mL of aqueous $NaIO_4$ (0.1 mol equiv. per AGU), covered with aluminum foil, and stirred at room temperature for 24 h. The reaction was quenched with ethylene glycol, and the 2,3-dialdehyde was isolated in a gel form by washing and centrifugation. It was not dried further. The product was dispersed into an aqueous solution of sodium bisulfate (1 mol equiv. per AGU) and stirred at room temperature for 24 h to obtain the corresponding 2,3-sulfonate. The product was precipitated in ethanol and filtered to isolate the final compound.

The second mechanism was composed of a single reaction. The negative surface charge of the CNC was increased by surface sulfation using chlorosulfonic acid (ClSO3H. [55-56] The CNC (5 g) was dispersed in 200ml of DMF. A complex of ClSO3H in DMF (2mol eq/anhydrous glucose unit) was added dropwise to the CNC suspension and stirred at room temperature for 30min. The reaction was quenched using ethanol, and the resulting product was purified by dialyzing against water for 5 days.

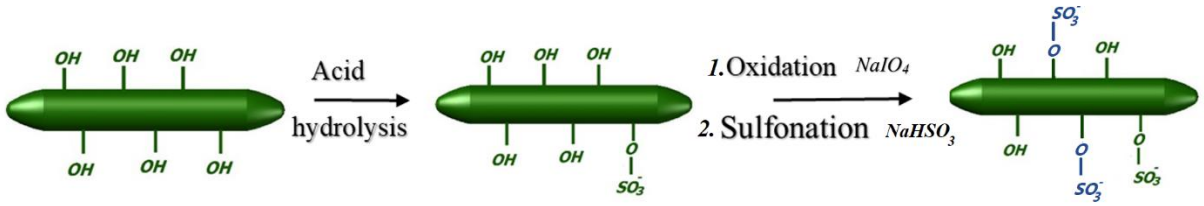

Figure 2. 2 Schematic illustration of synthesis of anionic CNC (nCNC) through oxidation followed by sulfonation

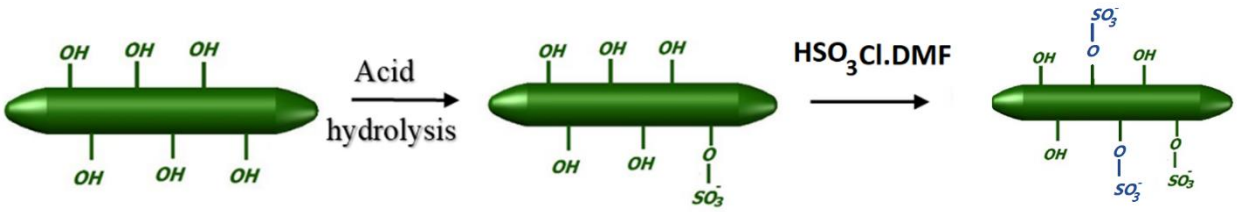

Figure 2. 3 Schematic illustration of synthesis of anionic CNC (nCNC) by sulfonation

Therefore, pCNC was synthesized through two different methods. We showed that we can use different synthesis routes to get materials with similar characteristics suitable for the sought applications (fabrication of diodes). Additionally, in the next chapter, we show that oxidation followed by sulfonation resulted in a cleavage of CNC crystals which affects its crystallinity. However, it is noted that the second method does not affect the crystallinity of the product.

2.3 ζ Potential

Brookhaven Instruments was used to characterize the zeta potential and particle size of CNC, nCNC, and pCNC. Typically, 0.1wt. % samples were prepared from the dried samples. The reported results are an average of three independent measurements of each sample. The reported zeta-potential values are sensitive to the particle size, ionic strength, surface charge, degree of dilution, and to the ionic strength of the sample. Therefore, these results have been presented to prove the surface modifications for all three samples.

2.4 Fourier Transform Infrared (FTIR) Spectroscopy

Thermo Scientific Nicolet 6700 FTIR spectrometer in transmission mode was used to analyze the structures of unmodified, cationic, and anionic modified CNCs. All the spectra were collected from 550 to 4000 cm^{-1} with a resolution of 4 cm^{-1} and 50 scans.

2.5 Titration

The surface charge was determined by conductometric titration, using previously reported methods.[26,57] Approximately 0.5 g of dried nCNC was suspended in 50 mL of 1 mM NaCl in a

100 mL three-neck flask. The conductivity was monitored during the titration with 10.11 mM AgCl from a dropper set to disperse 0.1 mL min^{-1}. The sulfate content in pCNC was determined by titrating 0.5 g of pCNC in 50 mL of 1 mM NaCl with 101.5 mM NaOH.

2.6 Thermogravimetric Analysis (TGA)

Thermogravimetric analysis (TGA) was carried out on a Netzsch TG 209 F3 Tarsus system. Samples weighing 10–20 mg were heated in a ceramic crucible at a heating rate of 10°Cmin^{-1} from 30 to 600 °C under a nitrogen atmosphere.

2.7 X-ray Diffraction (XRD)

X-ray diffraction measurements were performed on a Bruker AXS D8 Advance diffractometer, using a scan rate of 5° min^{-1} and a Cu Kα radiation source (λ = 1.5406 Å) operated at 40 kV and 30 mA. The samples were measured over the angular range of 2θ = 10−50°. Relative crystallinity indices (RCIs) were calculated using the Ruland−Rietveld approach. [58,59]

2.8 Atomic Force Microscopy (AFM)

Atomic force microscopy (AFM) images were obtained using an Asylum Instruments Cypher S AFM system in tapping mode at a scan rate of 0.49 Hz. Samples were prepared by spin-coating 0.01wt % solutions on a freshly cleaved mica surface. Images were obtained using Ti/Ir-coated silicon cantilevers with a resonant frequency of 300 kHz and a spring constant of 42 N m^{-1}.

2.9 Ultrasonic treatment (sonication)

The ultrasonic processor (sonicator) VCX-130 (Sonics & Materials Inc.) was used to sonicate the various samples in order to break agglomerations and flocs into individual components if possible. This sonicator is composed of a 6 mm probe to apply ultrasound energy (in Joules per gram (J/g) of CNC).

Ultrasound energy helps to improve the dispersion of the particles in solutions and typically 4000J/g has been used in the present work. This amount of ultrasonic energy has been reported as the minimum dosage required to break most flocs in CNC suspensions. [39] To prevent overheating

an ice bath has been used, since the surface charges are sensitive to temperature, and de-esterification of the sulfate groups on the surface of the crystal can occur due to an increase in temperature.[60,61,62]

2.10 Rheological measurements

The rheological properties were studied by using a rotational rheometer (MCR 502 Anton Paar) equipped with parallel-plate geometry (diameter of 50mm). To avoid sample evaporation during experiments, a thin film of mineral oil was applied on the periphery of the sample. All measurements were performed at room temperature of about 23 °C.

To study the viscoelastic properties of suspensions, a pre-shear of 500 s^{-1} for 1min was applied to all samples. The complex viscosity after this initial pre-shearing reaches a certain level (measured by using a time sweep at a small frequency of 1 rad/s and a strain amplitude of 1%), which implies that the suspension is in a nearly fully destructed state. A 60 min rest time was considered after pre-shearing to allow the suspension to rebuild its structure. Rest times longer than 30min did not increase the complex viscosity further. This was detected by using a time sweep test at a small frequency of 1 rad/s and a strain amplitude of 1%. Pre-shearing at low levels of shear rate such as <10 s^{-1} does not lead to reproducible results.

Steady shear was performed over the shear rate range from 0.01 to 1000 s^{-1} to study the visco-elasto-plastic behavior of CNC hydrogels. The viscosity value at each shear rate represents a steady-state, and once this is obtained, the rheometer shears the sample to the next shear rate. This test was performed from low-to-high shear rates to study network destruction with an increase in the shear rate.

Amplitude sweep experiments were also performed at the angular frequency of 1 rad/s to determine the range of strain amplitudes over which the samples exhibit linear viscoelastic behavior. Linear viscoelastic (LVE) frequency sweep tests were performed over angular frequencies in the range from 0.1 to 100 rad/s in order to determine the viscoelastic properties of pristine (CNC), cationic (pCNC), and anionic (nCNC) suspensions.

2.11 Diode Assembly and Measurements

Spacers were made using an Objet 30 three-dimensional (3D) printer via Polyjet printing using VeroWhite material. Cylindrical slabs were cut from CNC–AG hydrogels and inserted into 10 mm holes in the VeroWhite spacers. The characteristic *I–V* curves were obtained using a computer-controlled Solartron 1287A potentiostat/galvanostat, Hampshire, U.K. The performance of the agarose CNC-based diode was investigated as a function of sweep scan rate, gel thickness, and nCNC/pCNC concentration.

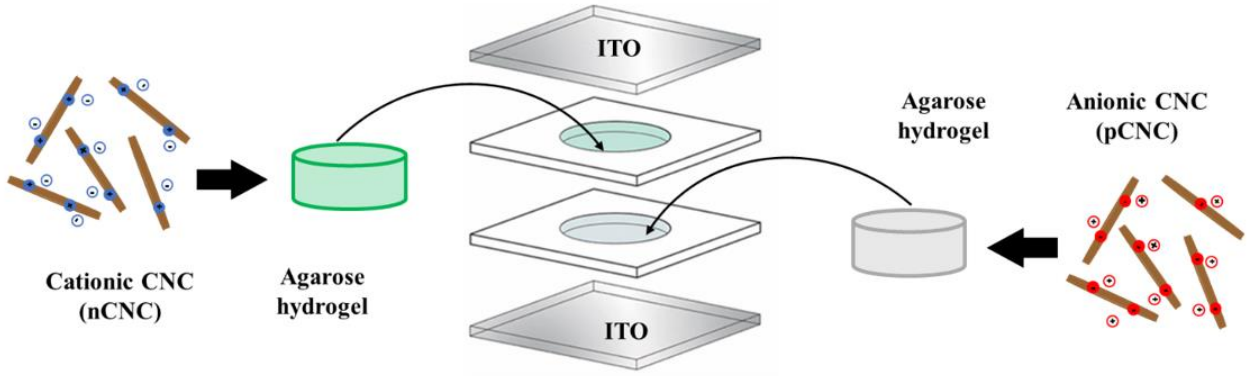

Figure 2. 4 Schematic of the gel diode device fabrication. Cationic CNC (nCNC) and ionic CNC (pCNC) were incorporated into an agarose hydrogel, placed into a spacer, and sandwiched between two ITO electrodes

Chapter 3: Cationic and Anionic Cellulose Nanocrystalline (CNC) Hydrogels: A Rheological Study

The rheological properties of CNC suspensions has been extensively studied [10,39,63–68], in the presence of electrolytes [10,11] and surfactants.[69,70] However, limited information exists on the rheological properties of cationic and anionic CNC hydrogels in relation to unmodified CNC suspensions [14]. Since positively and negatively CNCs are prepared for the fabrication of the diodes, a rheological study is necessary to perform before. It becomes important to identify factors that contribute to gelation of such systems as a critical factor/requirement for the fabrication of diodes. An important question is how the cations and anions affect the rheological properties as they are expected to affect the formed double layers around the CNC particles differently. Interaction forces (van der Waals and electrostatic) between individual CNC particles are expected to be different in the presence of different positively or negatively charged groups. The effects of concentration, and ultrasound treatment on the microstructure and rheological response of these CNC suspensions is of particular interest. For example, how the positive and negative surface charges of CNC affect the gelation at different concentrations and sonication levels.

3.1 Synthesis and characterization of the modified CNCs

In order to preserve the morphology and properties of the CNC, cationic (n-type) and anionic (p-type) CNCs were synthesized via surface modification. The cationic CNCs (nCNCs) were synthesized through nucleophilic substitution of NaOH activated alcohol groups on the surface of the CNC with glycidyltrimethylammonium chloride (GTMAC) as discussed in chapter 2. The analogous anionic CNCs (pCNCs) have a high degree of negatively charged groups.

The surface charges and the particles sizes of the CNC, pCNC, and nCNC were measured; the zeta potential values and the effective diameters are summarized in Figure 3.1. The unmodified CNC has a zeta potential of 41.13 mV because of the sulfonate groups introduced on the surface during sulfuric acid treatment. The negative surface charge was increased by increasing the amount of sulfonate groups. After surface modification, pCNC fibers maintain a negative surface charge and a zeta potential of –50 mV. This results in increased electrostatic repulsions that increase the colloidal stability of the pCNC. As seen from Figure 3.1, the effective (hydrodynamic) diameter is about half compared to those of the CNC and nCNC. Conversely, the nCNC has a positive

surface potential of 44.2 mV due to the introduction of quaternary ammonium salts from GTMAC. Due to the reversal of the surface potential, cationic cellulose nanocrystals have been reported to have significantly different colloidal behaviors compared to the negatively charged CNC. The hydrodynamic diameter is slightly higher to that of the CNC, indicating that the particles of the nCNC aggregate more.

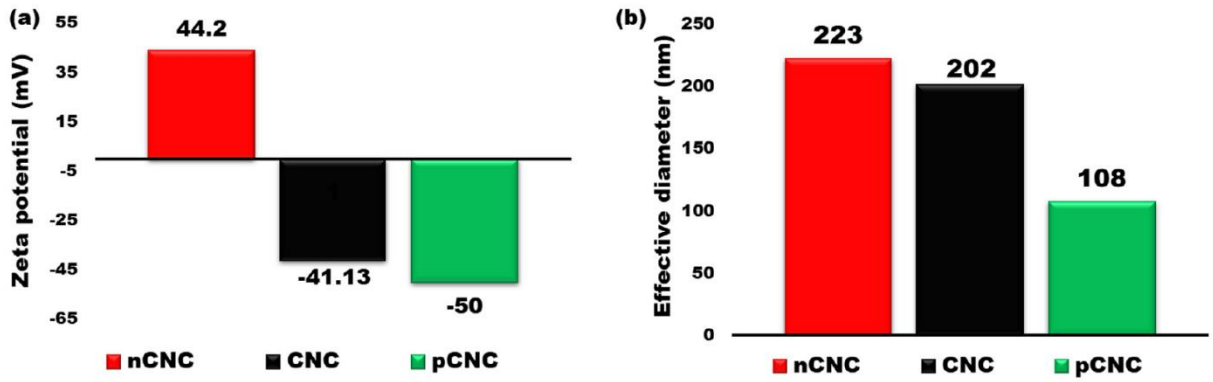

Figure 3. 1 Zeta potential (a) and DLS (b) of the unmodified CNC, nCNC, and pCNC.

3.1 Effect of pre-shear level

Charged rod-like colloidal particles such as CNC have a plethora of ways they can orient. They assemble into structures based on the interplay between electrostatic, van der Waal, hydrophobic and hydrogen bonding forces. Thus, to efficiently characterize these materials using rheology, it becomes crucial to control their structure before any rheological testing begins. This can be achieved by applying a certain level of pre-shear. The shear breaks up the aggregated particles (flocs) and positions the particles into a preferred orientation. Therefore, it is important to determine the amount of shear and the duration that is required to achieve this steady state get reproducible results.

First, steady-shear experiments on unsonicated CNC samples show that the shear stress settles to its steady-state value quickly, within a few seconds (Figure 3.2). The stress typically starts at a high value, and the breakage of flocs gradually leads to a much smaller value and levels to a constant value, indicating that a steady-state structure is obtained. However, we presume that not

all aggregations have been broken. It takes a longer time at a higher shear rate to settle to a steady-state value, indicating that significant structural changes continue (gradual breakdown of flocs) at higher shear rates. Therefore, any pre-shear should use a high shear rate in order to achieve a true steady state.

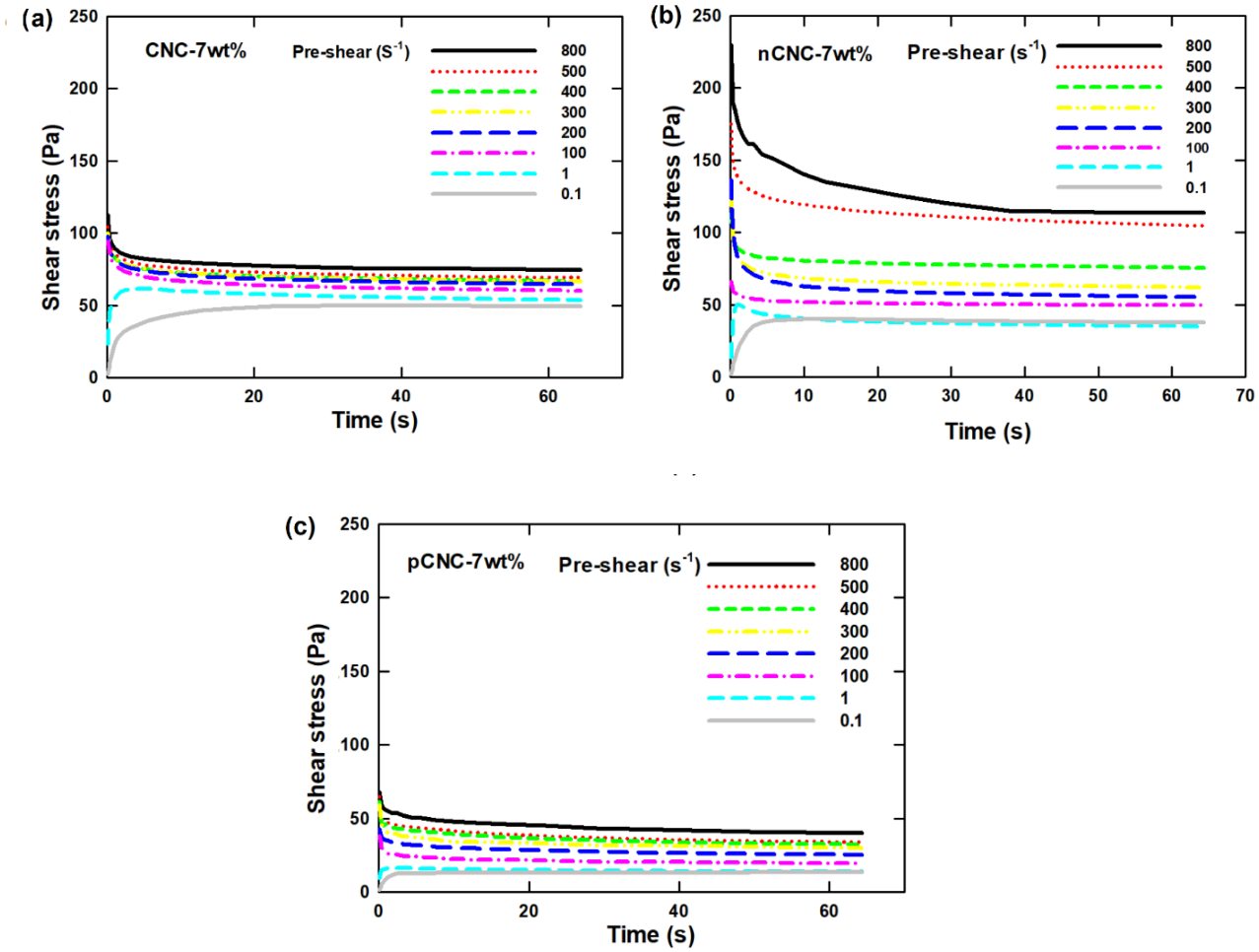

Figure 3. 2 Pre-shear test at different shear rates for the unsonicated 7 wt. % (a) unmodified CNC, (b) cationic CNC (nCNC), and (c) anionic CNC (pCNC). The shear stress decreases to its steady-state value, indicating that flocs break within a few seconds (10–20 s)

After pre-shear, the sample immediately starts ordering into a constant structure (recovery) directed by the interaction forces between the individual fibers (van der Waal, electrostatic, and hydrogen) present in the material. In all cases, after pre-shearing, a recovery time of at least 60 min has been required (in some cases, longer times have been used) for the suspension to recover its structure in a reproducible way. This was checked by performing a time sweep experiment at a small frequency (1 rad/s) and shear strain amplitude (1%), i.e., conditions within the limits of linear

viscoelasticity, which are not far from their equilibrium state due to the presence of Brownian motion that "corrects" deviations. Within this time period, the structure recovers to an equilibrium state in a reproducible way.

Unsonicated CNC samples always have a higher modulus compared to the sonicated samples at a given pre-shear protocol [Figure 3.3(a)]. In contrast, the sonicated samples show a transition (rather a sudden increase in modulus) after a certain period of pre-shear, which is an indication of the increased rate of flocculation. Sonication breaks up flocs into individual rods, and due to electrostatic repulsion, these particles are prevented to form flocs again. After pre-shear, these CNC particles self-organize into a nematic phase, resulting in the drastic/sudden increase in the modulus. Figure 3.3(b) shows time sweep tests for sonicated (4000 J/g) and unsonicated nCNC samples pre-sheared at various levels for 6000 s. It seems that a long time is needed to obtain complete structure recovery. However, for practical reasons, 1 h of recovery is enough to start any rheological testing at relatively high shear rates, as high shear will break flocs rapidly, leading to its equilibrium state structure [Figure 3.3(b)]. However, it is important to highlight the influence of the pre-shear rate. For the nCNC (both the unsonicated and sonicated samples), pre-shear at higher shear rates leads to a smaller modulus, indicating that the pre-shear of 0.1 s^{-1} is not enough to break flocs and rearrange the suspension into a homogeneous flocculated state. This is the reason for the large fluctuations at the beginning of the recovery test for the unsonicated samples. Pre-shearing at high shear rates of 300 s^{-1} and 500 s^{-1} leads to about the same equilibrium modulus. Sonication of samples at the beginning (before pre-shear) leads to individual rods that form hydrogen bonding retaining a relatively strong structure. In this case, the modulus of the sonicated samples is higher than that of the unsonicated sample at a given pre-shear rate, respectively. [Figure 3.3(b)]. The latter observation is not the case for unmodified CNC suspensions due to much less hydrogen bonding between the individual rods of sonicated samples.

Finally, Figure 3.3(c) depicts recovery results for the pCNC at various pre-shear levels. Pre-shearing at high shear rates of 300 s^{-1} and 500 s^{-1} leads to a similar equilibrium modulus. The level of modulus for these pCNC suspensions is about one order of magnitude lower than those of the nCNC and unmodified CNC. This is due to the higher charge density leading to increased electrostatic repulsion, resulting in less agglomerations/flocs. The increased modulus in the nCNC

[sonicated state in Figure 3.3(c)] is due to the effects of hydrogen bonding between individual fibers, which forms a relatively stronger structure.

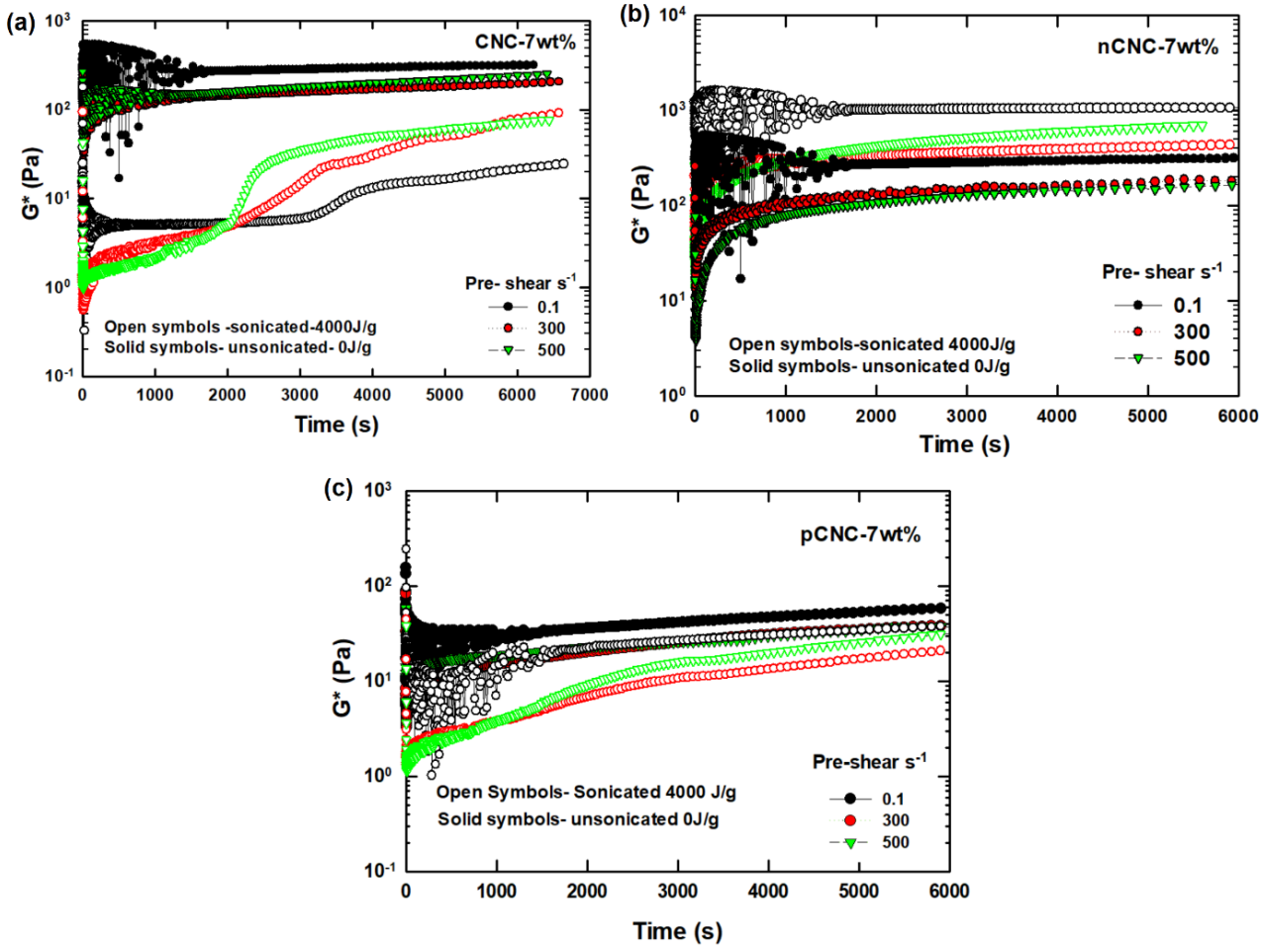

Figure 3. 3 Recovery test for about 2h after applying pre-shear rates of 0.1, 300, and 500 s^{-1}, a shear strain of 1%, and an angular frequency of 1 rad/s for 7 wt. % of (a) CNC, (b) cationic CNC (nCNC), and (c) anionic CNC (pCNC) samples with and without sonication (4000J/g)

3.2 Effect of the shear direction

When deciding a particular pre-shear value and subsequent recovery time, the material's response in both directions should be considered. This is to ensure the complete elimination of any pre-shear history from viscoelastic materials. If successfully eliminated, the response should be identical in both directions.[71] We investigated such an influence for modified and unmodified CNC samples and demonstrated that the pre-shearing used in the present study complies with the

experimental protocol established by Choi and Rogers [71] to address the extremely important effect of pre-shearing in producing reproducible rheological results. The following three tests were performed for 7wt. % unsonicated CNC suspensions with pre-shear at 500 s^{-1} for 1min in both directions [positive (P) and negative (N)] to ensure that all structures have been broken down followed by a steady shear rate of 0.5 s^{-1} in both directions (P and N) for various levels of recovery/rest times between the pre-shear and steady-shear (no recovery time, 20min of recovery time, and 60min of recovery time). Figure 3.4(a) explains the experimental protocol where all possible combinations of pre-shear (P and N) followed by steady shear (P and N) with no recovery/rest time in between are given. Note that the cases P–P and N–N, as well as the cases P–N and N–P, are identical. As such, the response of the material is identical in P–P and N–N and in P–N and N–P. However, the different response of N–N and P–P with those of N–P and P–N shows that a different strain history has been induced in each case, which caused the structure biased in each direction. [71,72] When the rest time between pre-shear and start-up of steady-shear increased, the bias of the shearing direction on the material structural changes decreases (Figure 3.5) and eventually is eliminated for a rest/recovery time of 60min (Figure 3.6).

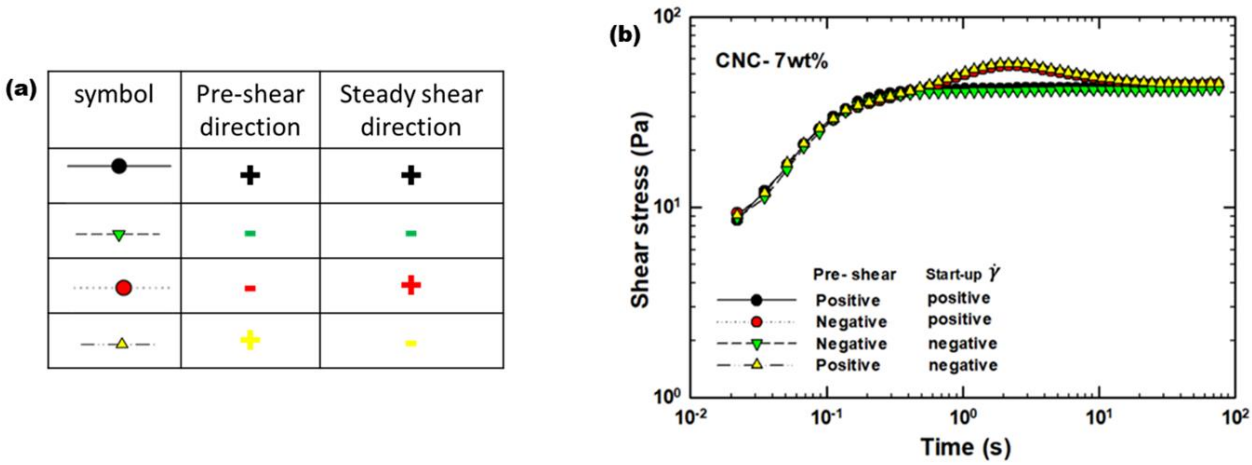

Figure 3. 4 (a) Table explaining the pre-shear protocol. (b) Four experiments carried out with a pre-shear rate of 500/s for 1min and a steady shear rate of 0.5 s^{-1} without rest/recovery time between pre-shear and start-up of steady shear. The shear stress responses of the 7 wt. % CNC suspension in the four cases of start-up of steady shear of 0.5 s^{-1} showing the different responses of the P–P and N–N cases compared to those of N–S and S–N are shown, indicating that a different strain history has been induced in each case, which caused the material structure biased in each direction.

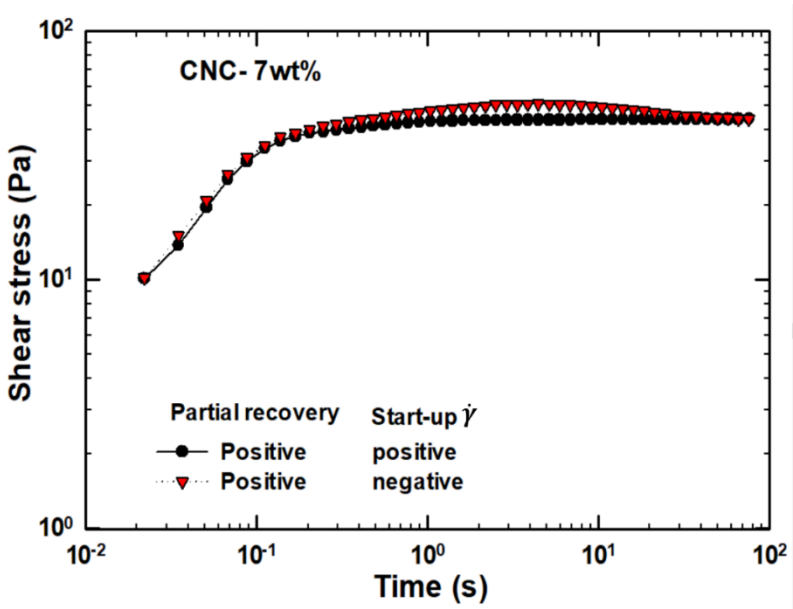

Figure 3. 5 The shear-stress responses of the 7 wt. % CNC suspension in the start-up of steady shear of 0.5 s^{-1} showing the different responses of the P–P case compared to those of P–N, indicating that a different strain history has been induced in each case, which caused the material structure biased in each direction. The rest time of 20 min between pre-shear and start-up of steady shear has decreased the bias of the shear direction on the material structural changes.

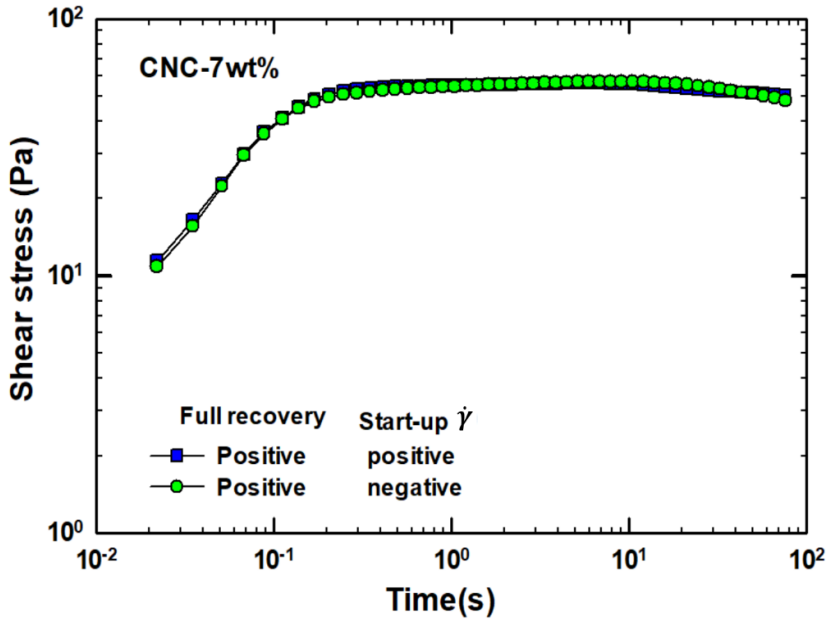

Figure 3. 6 The shear-stress responses of the 7 wt. % CNC suspension in the start-up. The shear-stress responses of the 7 wt. % CNC suspension in the start-up of steady shear of 0.5 s^{-1} showing the different responses of the P–P case compared to those of P–N, indicating that a different strain history has been induced in each case, which caused the material structure biased in each direction. The rest time of 60 min between pre-shear and start-up of steady shear has eliminated the bias of the shear direction on the material structural changes.

These results demonstrate that a pre-shear of 1 min at a high enough shear rate, i.e., 500 s^{-1}, followed by a recovery time of about 60 min may eliminate any preferential strain history, leading to nearly a complete, equilibrium recovery of the material, which can lead to reproducible and reliable rheological results.

3.3 Steady shear

The influence of pre-shear on the rheological behavior of CNC suspensions was investigated by measuring the steady-state shear viscosity. The liquid crystal phase of CNCs is formed when the aggregated particles are broken up into individual CNC rods. This formation is evident from the rheological analysis from the appearance of three distinct regions in the viscosity profiles. Sonication has been shown to achieve this effect for concentrated CNC samples. Here, the pre-shear of different CNC samples was investigated to show if pre-shear sufficiently breaks aggregates for the lyotropic phase to be observed and how the different surface modification aids the process of dispersion and ordering. These exhibit a Newtonian plateau at low shear rates, a shear thinning region at intermediate shear rates, and a second plateau at high shear rates.

Samples were pre-sheared at 500 s^{-1} for 1min and rested for 30min. Figure 3.7 depicts the steady-state shear viscosity and remove the corresponding shear stress vs shear rate curves of unsonicated CNC, nCNC, and pCNC suspensions as a function of shear rate at four different concentrations (1, 3, 5, and 7wt. %). For the CNC [Figure 3.7(a)], we observe the three-region viscosity profile for samples of 1 and 3wt. %, characteristic of lyotropic polymer liquid crystals. At higher concentrations (5 wt. % and 7wt. %), only a single shear thinning behavior is observed over the entire range of shear rates. This indicates the absence of the chiral nematic ordered phase, likely due to the gel like behavior of the material at this concentration, which inhibits ordering. These results agree with previously reported results for the CNC at similar concentrations. [27]

The viscosity profiles of cationic cellulose nanocrystals at concentrations of 3–7wt. % exhibit only shear thinning behavior [Figures 3.7(c) and 3.7(d)]. The material forms a gel at low concentrations; this is because the nCNC has low surface charge density, and thus, the material is less colloidally stable and aggregates easily. In addition, due to the new functional group, a hydrogen bonding forms, which causes an ordered structure at lower concentrations. Consequently, the cationically modified CNC (nCNC) has a tendency to form thixotropic gels.[26,14] Only at low concentrations,

1wt. %, the nCNC exhibits the three-region viscosity profile, highlighting that the lyotropic phase can be formed in the absence of significant aggregation.

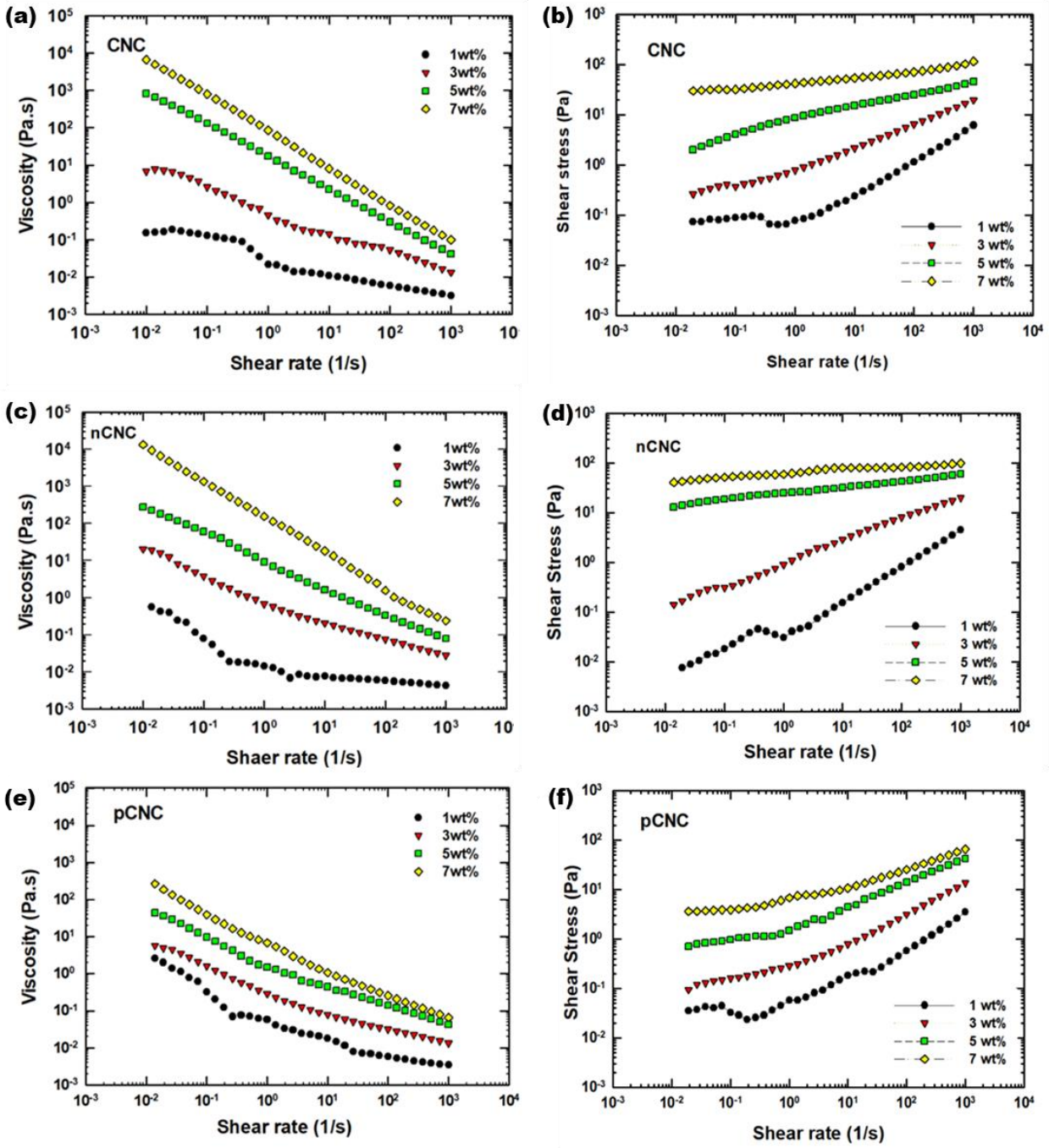

Figure 3. 7 Steady-state viscosity vs shear rate with a concentration varying from 1% to 7% for the unsonicated u (a) CNC, (b) nCNC, and (c) pCNC.

Figure 3.7(e) depicts the viscosity profile of the pCNC. This material is anionic cellulose nanocrystals with high negative surface charge density. The viscosity of the pCNC decreased drastically compared to that of the unmodified CNC and nCNC at all concentrations. Due to the significant electrostatic repulsion between the particles of the pCNC, the material easily flows, which results in a much lower viscosity. It has been reported that the pCNC with large charge density enhances the water solubility properties.[73] Therefore, the pCNC that contains more sulfonate will result in lower viscosity. The three-region viscosity profile is observed at all concentrations of the pCNC due to the high colloidal stability of the particles, which enhances the formation of the lyotropic phase.

The yield stress observed in the viscosity profile (Figure 3.7) can be calculated using the Herschel–Bulkley model (Figure 3.8), [73,74]

$$\tau = \tau_y + m\dot{\gamma}^n \tag{3.1}$$

Where $\tau, \dot{\gamma}, \tau_y, m$ and n are known as shear stress, shear rate, yield stress, consistency index and power law exponent, respectively. Typical results of the curve fitting are shown in Table 3.1 for 7wt. %. Clearly, the nCNC possesses the highest yield stress due to hydrogen bonding. The effect of the concentration on yielding of the various suspensions is examined below.

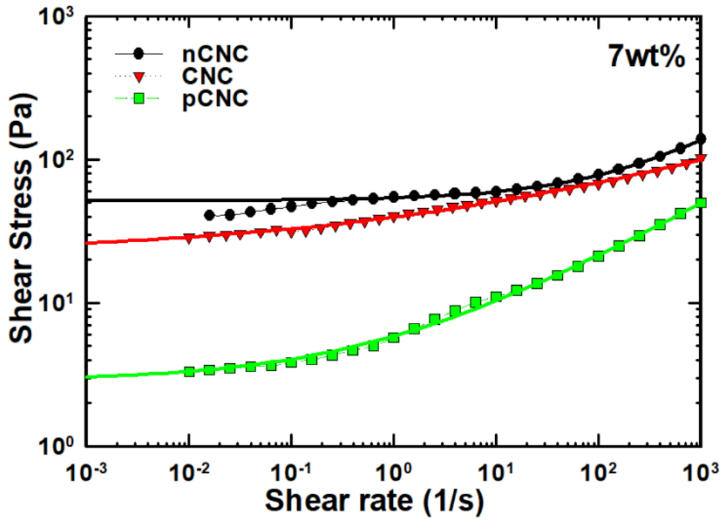

Figure 3. 8 The flow curves of 7 wt. % of the unmodified CNC, cationic (nCNC), and anionic (pCNC) of unsonicated samples. The continuous lines are the best fit of the HB model to determine the yield stress of these suspensions in order to compare them with the values obtained from strain amplitude sweep experiments.

Table 3. 1 Fitting parameters of the Herschel–Buckley model for suspensions having a concentration of 7wt%

Samples	τ_Y (Pa)	m (Pa.s^n)	n	R^2
7wt % CNC	22.3	17.32	0.2167	0.9954
7wt% nCNC	45.7	5.093	0.4148	0.9856
7wt% pCNC	2.9	3.013	0.3973	0.9991

3.4 Linear viscoelasticity limit and yield stress

The yielding behavior of the CNC suspensions can be assessed by strain amplitude sweep tests at a fixed frequency (typically 1 rad/s is used). From these experiments, the limiting value of strain for transition from a linear to a nonlinear viscoelastic response and the stress for shear yielding/melting (initiation of flow) can be obtained. [72,75,76,66] Figure 3.9 plots the results for the CNC, nCNC, and pCNC of 3, 5, and 7wt. % at the frequency of 1 rad/s. In all cases, at small strains, G′ > G′′', indicating gel-like behavior. At progressively higher strain amplitudes, G′′ > G′, which indicates the initiation of flow. Moreover, at a specific strain amplitude, a weak maximum appearing in G" (clearer for the nCNC at higher concentrations) is observed, which is related to the onset of flow (shear melting). The existence of this maximum (known as the Payne effect) is an indication of the existence of yield stress. In fact, a sequence of processes starts at the point where G′′ starts increasing (increase in dissipation showing flow initiation),which is also the point where the stress ($|G^*|$)-strain γ relationship deviates from linearity.[61,60,77] The stress at the maximum value of G′′ has also been interpreted as yield stress. The maximum stress is shown clearly in Figures 3.9 (b)(d)(f), where the data of Figures 3.9(a), (c) and (e) are plotted as stress-strain curves ($\sigma \equiv |G^*| - \gamma$). Table 3.2 summarizes the calculate yield stress value in two ways: (i)as the stress value when G′ and G′′ reduce to their 90% of their limiting linear viscoelastic values labelled in Table 3.2 as $\sigma_{y(90)}$ and (ii) the stress that corresponds to local maximum G′′ value, labelled in Table 3.2 as $\sigma_{y(\max)}$. From Table 3.2, it can be seen that the pCNC possesses the weakest

network and thus smaller yield stress, while that with the nCNC the strongest. Also, for all samples, the yield stress increases significantly with an increase in the concentration. These results agree with those listed in Table 3.1 obtained from steady-shear experiments.

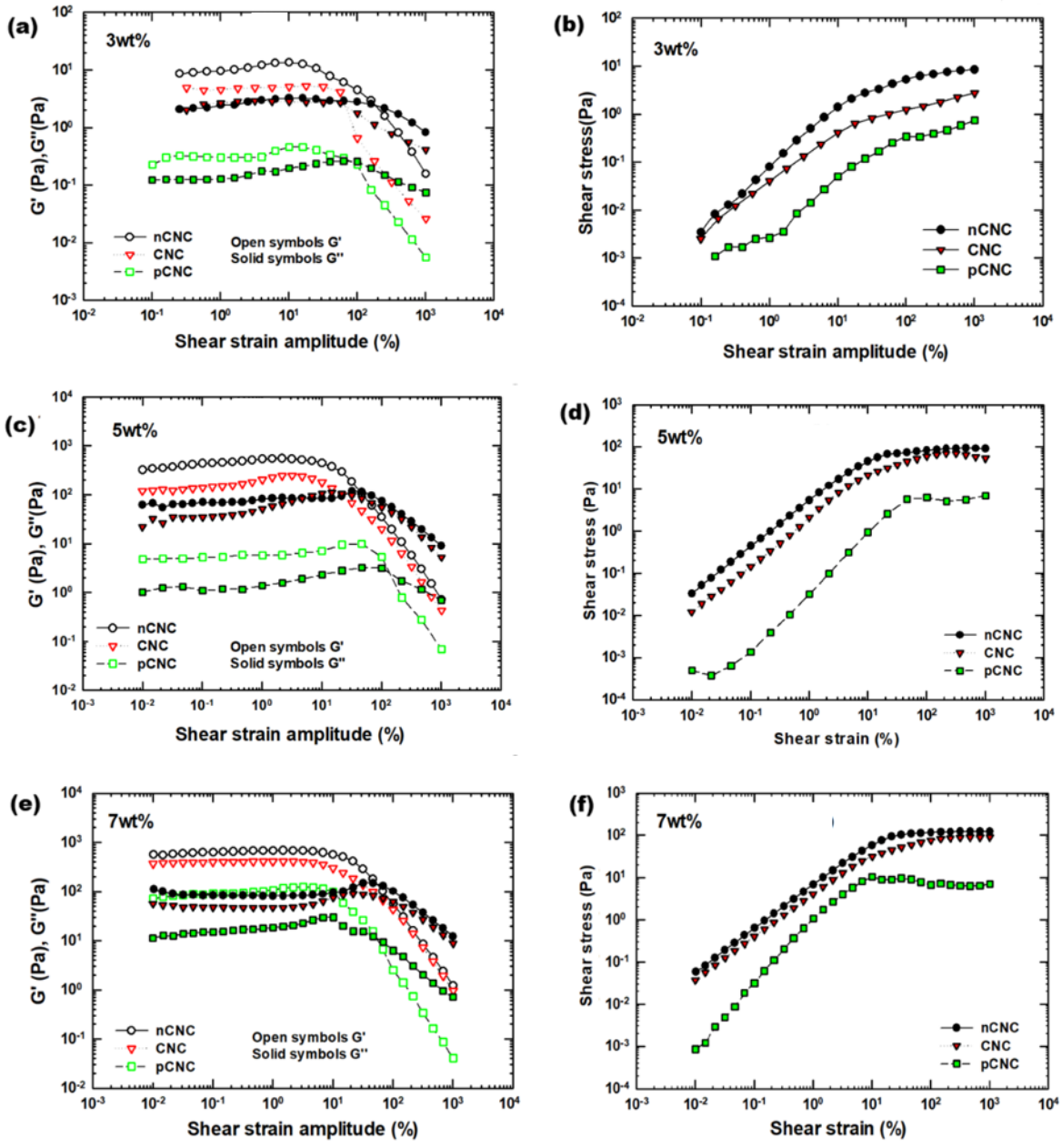

Figure 3. 9 Strain amplitude sweeps of 3 wt. % (a) and (b), 5 wt. % (c) and (d), and 7 wt. % (e) and (f) for unmodified, cationic, and anionic CNC suspensions at 25 C and ω=1 rad/s.

Table 3. 2 Yield stress values calculated from strain amplitude sweep tests plotted in Figures 3.9 for unsonicated suspensions of CNC, nCNC and pCNC

Samples	Concentration (wt%)	$\sigma_{y(90)}$ (Pa)	$\sigma_{y(\max)}$ (Pa)
CNC	3	2.5	-
	5	19	22
	7	25	44
nCNC	3	3	-
	5	40	63
	7	49	76
pCNC	3	0.3	-
	5	5	7
	7	9	10

3.5 Linear viscoelasticity (SAOS)moduli: The effect of sonication

While sonication can break flocs in the CNC producing a stable suspension, Brownian motion and van der Waals forces eventually might recreate these flocs after significantly long time—defined as aging. In the case of the nCNC, the presence of hydrogen bonding retains its structure in the suspensions, which increases the rheological properties significantly as will be discussed below. Isothermal frequency sweep tests were conducted for 5wt. % unmodified cellulose nanocrystals (CNCs) and for nCNCs and pCNCs. The results before and after sonication for each case are shown in Figure 3.10. In Figure 3.10(a), the 5wt. % CNC suspension before sonication behaves like a gel since G′ and G″ overlap over a wide range of frequencies. After sonication, G″ > G′ defining a viscoelastic liquid with G′ and G″ significantly lower for the sonicated samples. The viscosity significantly decreases due to the CNC particle size reduction [breakup of flocs as shown in the schematic besides Figure 3.10(a)].

Figure 3.10(c) shows 5wt. % nCNC with positive surface charges (nCNC), the behavior of which resembles that of a viscoelastic solid where G′is higher than G″ over the whole range of frequencies. Interestingly, after sonication, G′ and G″ increase [opposite to the case of the CNC plotted in Figure 3.10(a)]. This is due to the formation of significant hydrogen bonding between individual fibers after the application of ultrasound energy. These results agree with the pre-shear results discussed in Section 3.1. Hasani et al. reported that the cationically modified CNC showed a tendency to form thixotropic gel in concentrated aqueous suspensions of the cationically modified CNC. A lower electrostatic repulsion was mainly responsible for the observed gelation.[26] Finally, in Figure 3.10 (e) ,(f) negative surface charges had lower viscosity in comparison with the pristine CNC. After sonication, the viscosity drops further by about one order of magnitude. Sonication breaks up the gel structure of high concentration samples and disperses the individual nanorods. Stronger electrostatic repulsions in the case of the pCNC compared to the CNC make the suspension more stable (preventing hydrogen bonding), and thus, its viscosity becomes lower than that of the unmodified CNC.

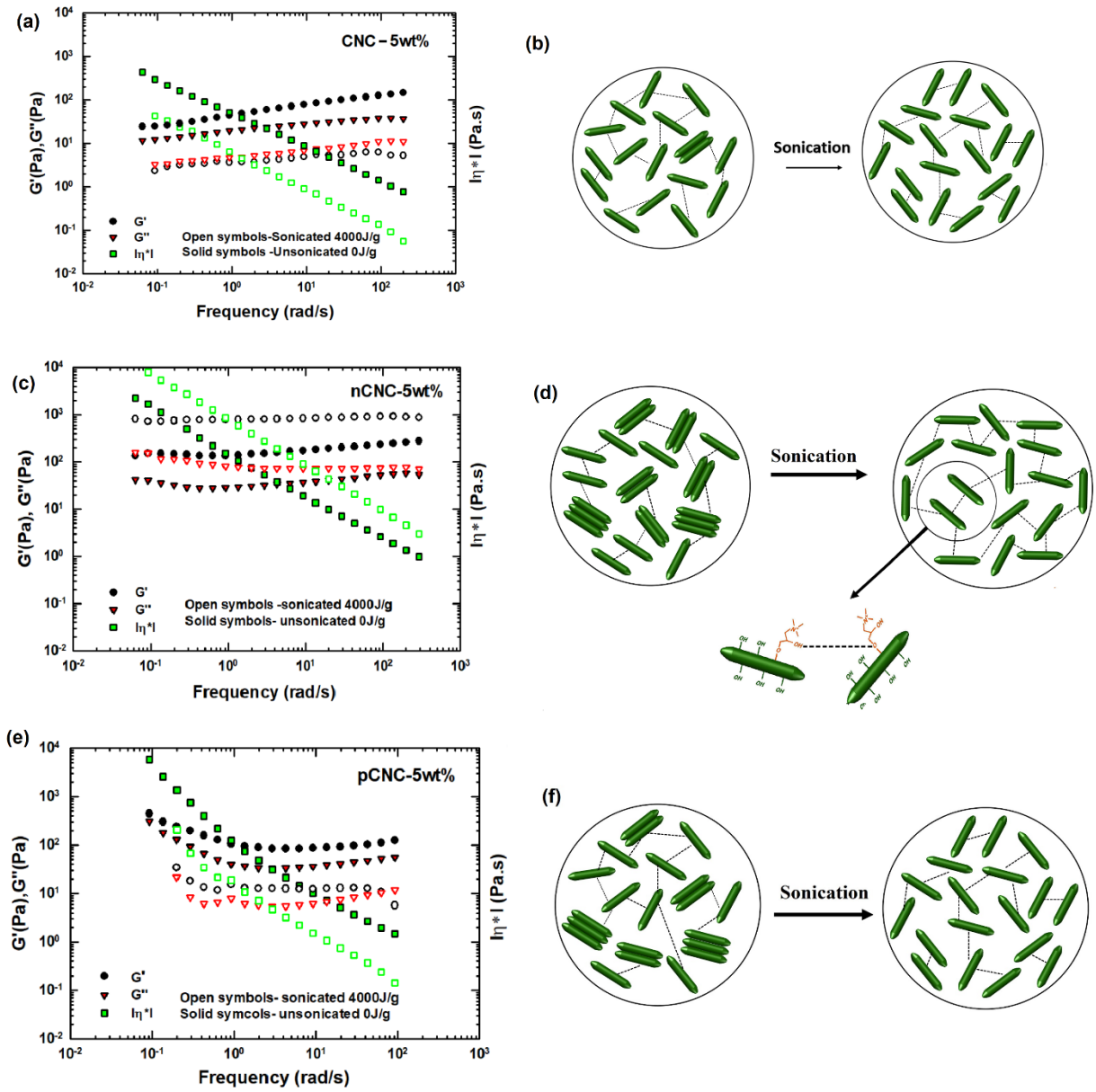

Figure 3. 10 The storage modulus G', loss modulus $G''$and complex viscosity l $\eta^*(\omega)$ l versus the frequency of (a) unsonicated (solid symbols) and sonicated at 4000 J/g (open symbols) of 5 wt. % CNC and (b) schematic showing the effect of sonication on the CNC. (c) Unsonicated (solid symbols) and sonicated at 4000 J/g (open symbols) of 5 wt. % nCNC, (d) schematic showing the effect of sonication on the nCNC, (e) unsonicated (solid symbols) and sonicated at 4000 J/g (open symbols) of 5 wt. % pCNC, and (f) schematic showing the effect of sonication on the pCNC.

3.6 Summary

Cationic and anionic cellulose nanocrystalline were successfully prepared by Kudzanai Nyamayaro at the chemistry Department (UBC). These materials were used to produced hydrogels in order to study their rheological behaviour. The importance of applying pre-shear on cellulose nanocrystals was investigated and a pre-shear protocol was established to obtain accurate and reproducible results. It has been shown how the application of ultrasound energy (sonication) affect the pristine and modified (negatively and positively charged) CNC. After sonication, in CNC and pCNC reduction in G´ and G″ was observed. On the contrary, the values of G´and G″ in sonicated nCNC increase over the whole range of the frequencies compared to unsonicated ones. This was found to be due to the stronger hydrogen-bonding interactions between the individual fibers that form in the case of nCNC. The rheological results confirmed that in the case of the anionic surface modification (pCNC suspensions), electrostatic repulsion stabilize these suspensions (absence of flocs) and result in much lower viscosities compared to their nCNC and CNC counterparts. However, cationic surface modification of CNC, makes the suspensions to behave like a gel, essentially a stronger gel-like behaviour compared to the pristine CNC aqueous suspension.

Finally, linear viscoelastic measurements have also shown that nCNC produces a stronger gel due to the presence of hydrogen bonding compared to those of unmodified CNC and pCNC. The yield stress values determined for several suspension at various concentrations corroborate these observations that (i) hydrogen bonding in the case of nCNC increase the rheological properties of these suspensions compared to those of pCNC and nCNC (ii) due to the formation of bonding between individual rods, the rheological properties of sonicated nCNC samples are much higher that those of unsonicated ones (the opposite is true for CNC and pCNC (iii) pCNC sonicated samples at given concentrations possess the lower rheological properties (including yield stress) due to the stronger electrostatic repulsions that decrease their hydrodynamic diameters significantly.

Chapter 4: Toward Biodegradable Electronics: Ionic Diodes Based on a Cellulose Nanocrystal−Agarose Hydrogel

In this chapter, the fabrication and testing of diodes are presented using the modified CNCs whose synthesis was presented in chapter 2 and their rheological characterization in chapter 3. Here, the attractive properties of hydrogels and CNCs are combined to fabricate a biodegradable fixed rectifying junction. Cationic (nCNC) and anionic (pCNC) cellulose nanocrystals synthesized via surface modification (see chapter 2) were incorporated into an agarose matrix to form mechanically strong and stable hydrogels. The successful fabrication of ionic diodes is demonstrated in this chapter which are created from low quantities of high surface area n- and pCNC doped agarose hydrogels. Moreover, it is further demonstrated that these diodes outperform both the MFC and the PSS/PDAC-AG diodes.

4.1 Characterization of the Modified CNCs

To preserve the morphology and properties of CNC, cationic (n-type) and anionic (p-type) CNCs were synthesized via surface modification as has already been discussed and presented in chapter 2. In this section, the results from several characterization techniques are presented.

The surface charges of CNC, pCNC, and nCNC were measured; the ζ potential values are summarized in Table 4.1. Unmodified CNC has a ζ potential of −48 mV because of the sulfate half ester groups introduced on the surface during the sulfuric acid treatment.[55] After surface modification, pCNC maintains a negative surface charge and a ζ potential of −39 mV. Conversely, nCNC has a positive surface potential of +50 mV due to the introduction of quaternary ammonium salts from GTMAC.

The charged groups on the surface of the material were quantified using conductometric titration (Table 4.1). The charge density determined by conductometric titration for pCNC was found to be 1.40 mmol g^{-1} and was significantly higher than that for CNC of 0.198 mmol g^{-1}.

Table 4. 1 Zeta potential, relative crystallinity index (CI) and charge density from conductometric titration of unmodified CNC, nCNC and pCNC.

Entry	Sample	ζ [a]	RCI[b]	Titration charge density (mmol g^{-1}) [c]
1	CNC	–48 ± 2	81	0.198 ± 0.003
2	nCNC	+50 ± 1	60	0.131 ± 0.001
3	pCNC	–39 ± 10	45	1.40 ± 0.01

[a] Average of three independent measurements ± standard deviation. [b] Relative Crystallinity Index (RCI) determined via the Ruland−Rietveld approach using DiffracPlus Topas software. [c] Average of two titrations ± standard deviation. [d] Average of three independent measurements ± standard deviation

FTIR was used to screen for the successful modification of CNC. (Figure 4.1) The spectrum for nCNC exhibits increased intensity of the ether absorption bands in the region between 1030 and 1065 cm^{-1}, which is indicative of the formation of new ether bonds from grafting of GTMAC onto CNC. Additionally, there is a band at 1424 cm^{-1} , which can be attributed to the CH_2 or CH_3 bending mode of the GTMAC substituent. [53]

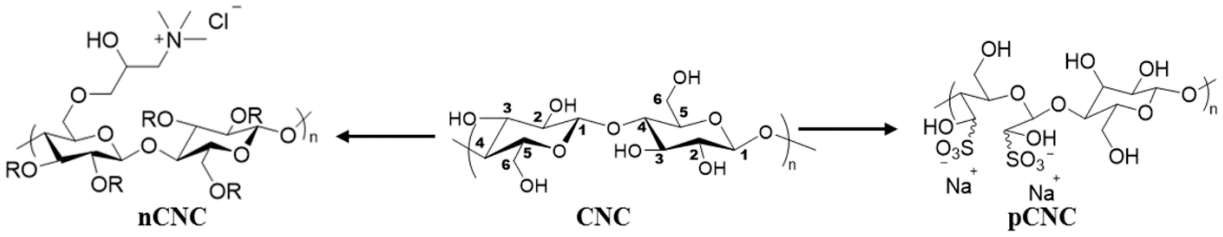

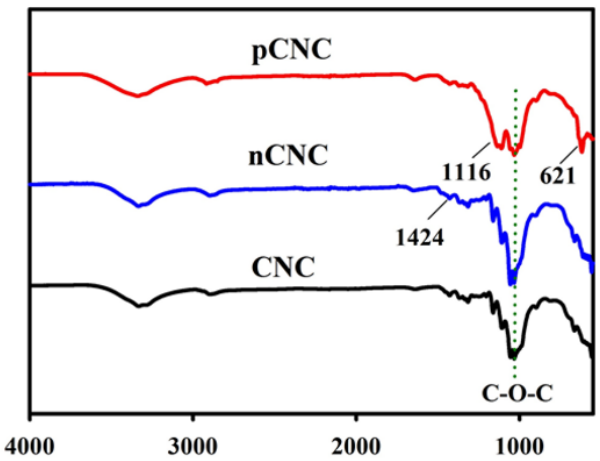

Figure 4. 1 FTIR of unmodified CNC, cationic CNC (nCNC) and anionic CNC (pCNC).

However, these features are not pronounced enough to give clear evidence of modification, likely due to a low degree of substitution. The formation of pCNC is more apparent from FTIR, where the spectrum of pCNC shows characteristic bands at 1116 and 621 cm^{-1} due to SO2 vibrations of the sulfonate group.[78]

The morphology and structural integrity of CNC after modification were analyzed using XRD and thermal analysis (Figure 4.2 a). Unmodified CNC showed typical peaks for the crystal structure of cellulose I, and the diffraction peaks at 2θ = 15.1, 17.5, 22.7, and 34.3° represent cellulose I crystal planes (101), (10$\bar{1}$), (002), and (040), respectively.[36] The XRD patterns of nCNC and pCNC possess the characteristic diffraction peaks of cellulose I, indicating that the original crystalline structure of CNC is retained after modification. However, there is a reduction in the Relative Crystallinity Index (RCI), in both cases, after modification (Table 4.1). The minor reduction in RCI for nCNC is due to mercerization from concentrated alkali treatment during modification.[79] The RCI for pCNC drops from 81% in unmodified CNCs to 41%, indicating pronounced structural changes. This has been attributed to the mechanism of periodate oxidation of CNC, which involves cleavage of the CNC diols resulting in peeling of the nanocrystals. [24,54]

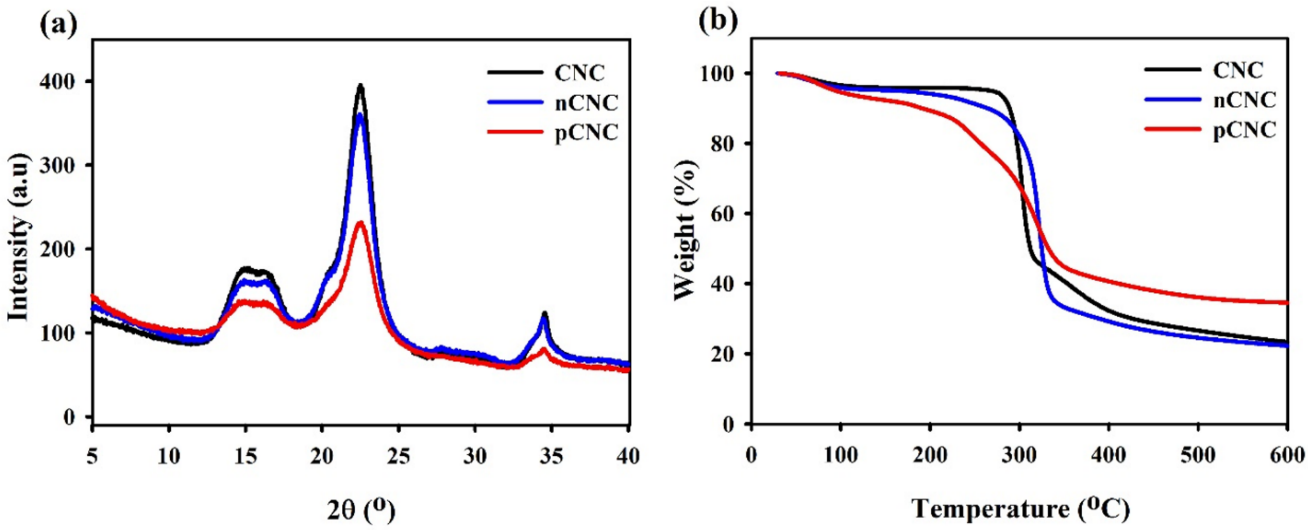

Figure 4. 2 (a) XRD and (b) TGA curves of unmodified CNC, cationic CNC (nCNC) and anionic CNC (pCNC)

The thermograms of nCNC and pCNC showed a minimal difference from unmodified CNCs (Figure 4.2b), indicating that the high thermal stability of CNC was maintained. Decomposition of unmodified CNCs starts at about 295 °C, accompanied by a 48% weight loss between 220 and 330 °C, and continued heating results in a gradual weight loss until 600 °C, which is characteristic of sulfonated CNCs. (45,46) In contrast, nCNC starts decomposition at around 314 °C and a weight loss of 57% between 220 and 330 °C, with significant weight loss up to 600 °C (residual char yield of 21% at 600 °C). The thermal degradation of pCNC started at a lower temperature (181 °C) and occurred over a broader temperature range (180−310 °C). Moreover, the residual char was higher (32% at 600 °C), which signifies increased sulfonate content. [80] nCNC and pCNC exhibit thermal properties similar to pristine CNC, with minor differences in the onset of thermal degradation and residual char. Overall, the changes in the thermal stability of the modified CNCs provide evidence of the surface modification of CNCs while maintaining the stability. The AFM images of CNC, nCNC, and pCNC (Figure 4.3) indicate that all samples have rod-like morphology. However, pCNC has additional spherical particles, suggesting that a fraction of the crystalline particles has been transformed into a different morphology with amorphous characteristics, which agrees with observations from XRD, and TG.

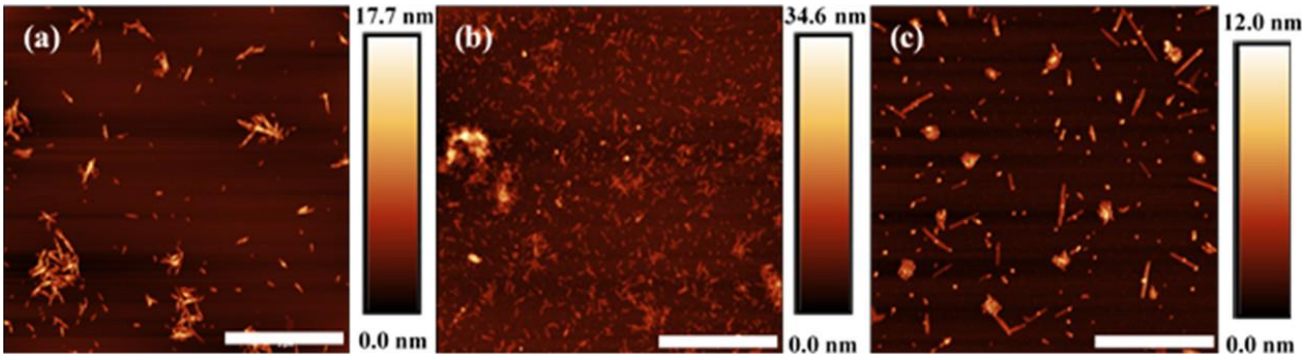

Figure 4. 3 AFM images of 0.01% wt. % solutions of CNC samples on mica: (a) unmodified CNC, (b) nCNC, and (c) pCNC (scale bar = 2 μm).

4.2 Formation and Characterization of CNC–Agarose Hydrogels

Cellulose nanocrystals have been extensively employed as reinforcing agents in hydrogels and other polymers.[81] Hence, the modified CNCs were incorporated into an agarose hydrogel to make

nCNC–AG and pCNC–AG gel layers for the diode. (Figure 4.4) To make the gels, the desired weight percent of nCNC or pCNC was dispersed in deionized water by mechanical stirring and sonication (4000 J g^{-1}), then 3 wt. % agarose was added, and the temperature was increased to 90 °C. Solutions were placed in Petri dishes or vials and cooled to room temperature to form the gels. Rheological characterization was performed after 24 h. This strategy is highly transferrable and can be employed in various hydrogels depending on the intended application. As a starting point, we employed agarose because of the easy gelation process and since it is also an abundant natural polysaccharide. Sulfonated CNCs and agarose–CNC composites have been shown to be biodegradable.[82,83] Coupled with ongoing research on 3D-printable cellulose materials and flexible electrodes, a fully flexible and biodegradable diode can be realized. [84,85]

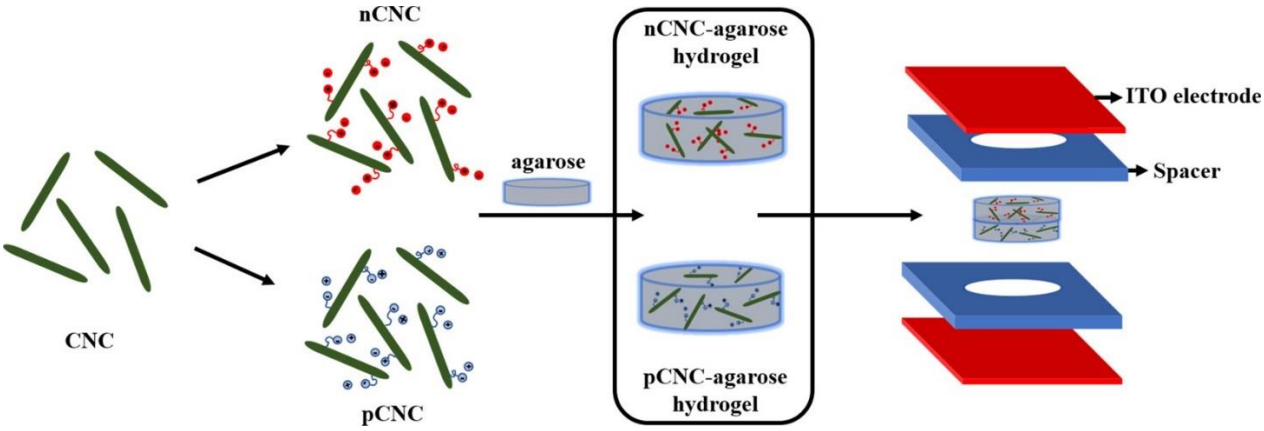

Figure 4. 4 Schematic representation of the ionic diode fabrication. Cationic CNC (nCNC) and anionic CNC (pCNC) were incorporated into two separate slabs of agarose. The agarose gels with oppositely charged CNCs were placed into spacers and sandwiched between ITO electrodes

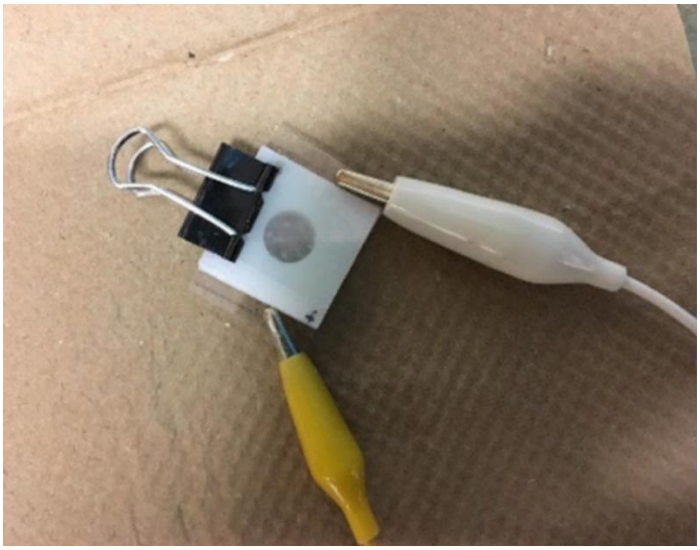

Figure 4. 5 Diode setup used to run electrochemical experiments

Rheology was used to evaluate the strength and stability of the agarose gels doped with the CNC, nCNC, and pCNC (most presented in chapter 2). Here we provide some additional relevant to the fabrication of diodes. Strain sweep oscillatory shear tests were carried out to determine the limiting value of the strain for a linear viscoelastic response and the stress for shear yielding (initiation of flow). The critical strain indicating the transition from a linear to nonlinear viscoelastic response for the filled hydrogels is slightly lower (Figure 4.6), which indicates that the doped hydrogel is stiffer than that of pure agarose. This is the case for high loadings of CNC; the particles disrupt the agarose network, reducing the connectivity and hence lowering elasticity.[86] Frequency sweep oscillatory shear carried out in the linear viscoelastic region and in the frequency range of 0.01–100 Hz is shown in (Figure 4.7 a,b). For all samples (CNC–AG, nCNC–AG, and pCNC–AG), the storage modulus (G') is always larger than the loss modulus (G'') by at least 1 order of magnitude, and both G' and G'' exhibit a weak frequency dependence in most cases. This indicates that the hydrogels exhibit soft solid-like viscoelastic behavior or strong gel-like behavior over the entire scanned frequency range. Dynamic time sweeps were conducted at 22 °C and a fixed frequency of 1 rad s^{-1} (Figure 4.8). The storage and loss moduli remain constant for over 3 h, indicating the excellent structural stability of the gels. As such, the gels have a network-like structure with a storage modulus on the order of 10^4 Pa, which is stable under the applied shear; hence gels are suitable for diode fabrication.

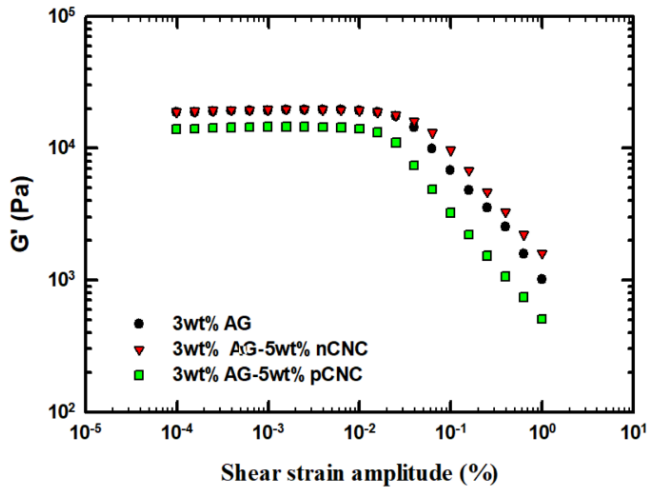

Figure 4. 6 Strain sweeps oscillatory shear tests of 3 wt.% agarose hydrogels doped with 5 wt.%

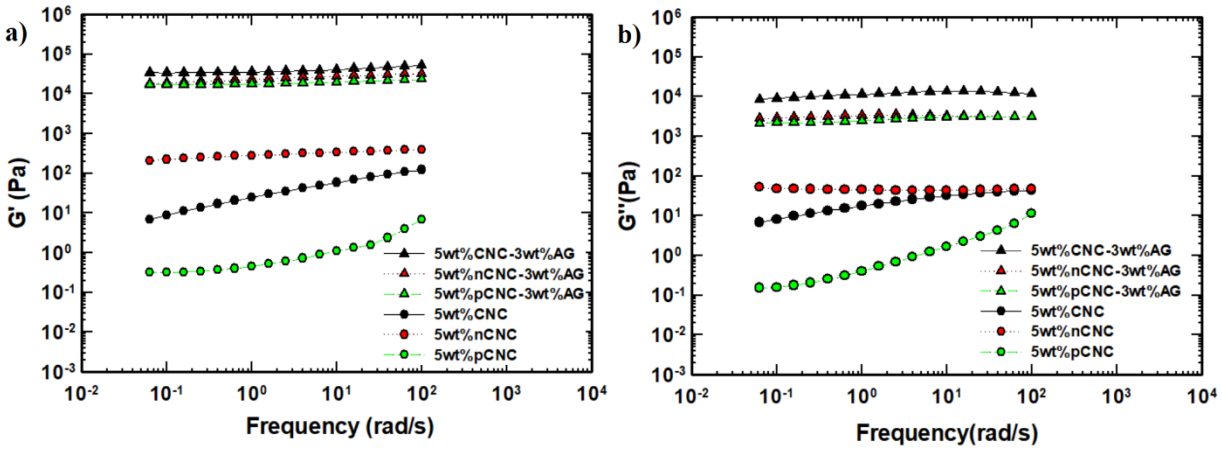

Figure 4. 7 Frequency sweep tests for different sample concentrations a) G′ vs. frequency b) G″ vs. Frequency

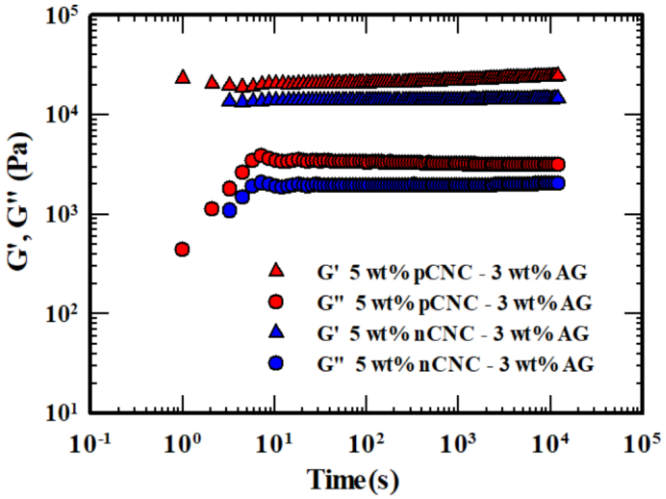

Figure 4. 8 Dynamic time sweep test results of 3wt% agarose doped with 5 wt.% pCNC and nCNC

4.3 Working Principle of Ionic Diodes

The diode itself is fabricated when two cylindrical agarose hydrogels, one doped with nCNC and the other with pCNC, are brought into contact and sandwiched between two ITO electrodes (Figure 4.4). The spacers are readily and precisely fabricated by 3D printing. The cellulose nanocrystals are entangled in the agarose matrix and cannot migrate when a potential is applied. The migration of nonreactive counterions (Cl^-, Na^+) controls the potential drops within the system,[87,88] which aids or suppresses the reduction/oxidation of water.[1]

In the forward bias (Figure 4.9a), water is reduced at the cathode ($2H_2O + 2e^- \rightarrow 2OH^- + H_2$, E^0 = 0 V) and oxidized at the anode ($2H_2O \rightarrow 4H^+ + O_2 + 4e^-$, E^0 = 1.23 V). The proton and hydroxide ions migrate toward the gel/gel junction where they combine to form H_2O completing the circuit. The nonreactive counterions also migrate toward the gel/gel interface, causing a large potential drop at the gel/electrode interface and accelerating oxidation and reduction of H_2O. In addition, the unhindered passage of H^+ and OH^- through the pCNC–AG and nCNC gel layers, respectively, results in a substantial increase in current.

In contrast, for reverse bias (Figure 4.9 b), the non-reactive ions migrate to the nearest electrode, resulting in a large potential drop over the region near the gel/gel interface. The applied potential is localized near the gel/gel junction, where a region analogous to a depletion region in a solid-

state semiconductor diode is formed. This greatly reduces the rate of oxidation/reduction at the electrode/gel interface, resulting in significantly less current than in the forward bias.

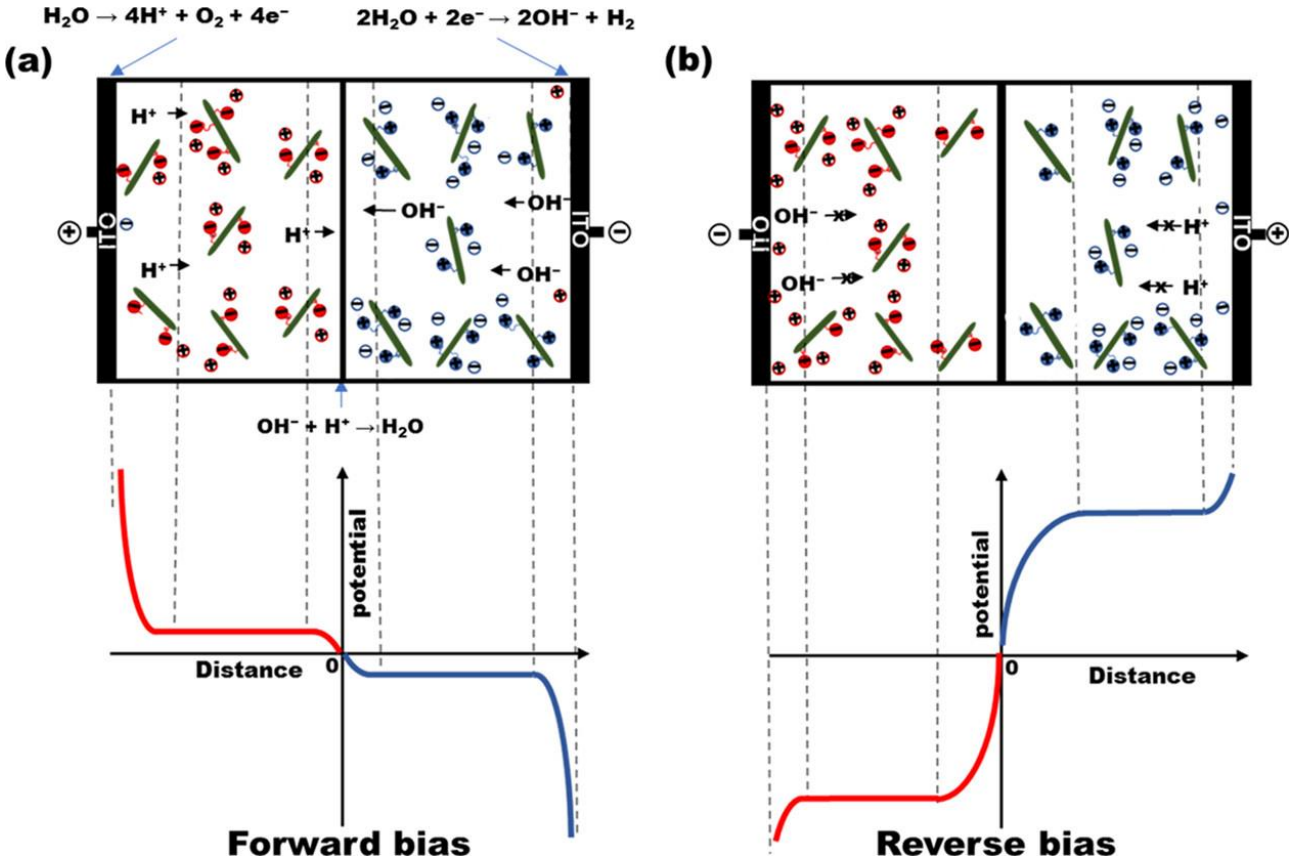

Figure 4. 9 Illustration of the rectification mechanism of the nCNC/pCNC–agarose ionic diode under (a) forward bias and (b) negative bias.

4.4 Rectification Behavior of Diodes

In the absence of an asymmetric junction, the current–voltage curves of either nCNC–AG or pCNC–AG have high conductivity under both positive and negative bias (Figure 4.10). Once an asymmetric junction is formed by bringing the two gels into contact, pronounced rectification is observed (Figure 4.11). The distribution of the ions in the hydrogel has a strong influence on the rectification.[1]

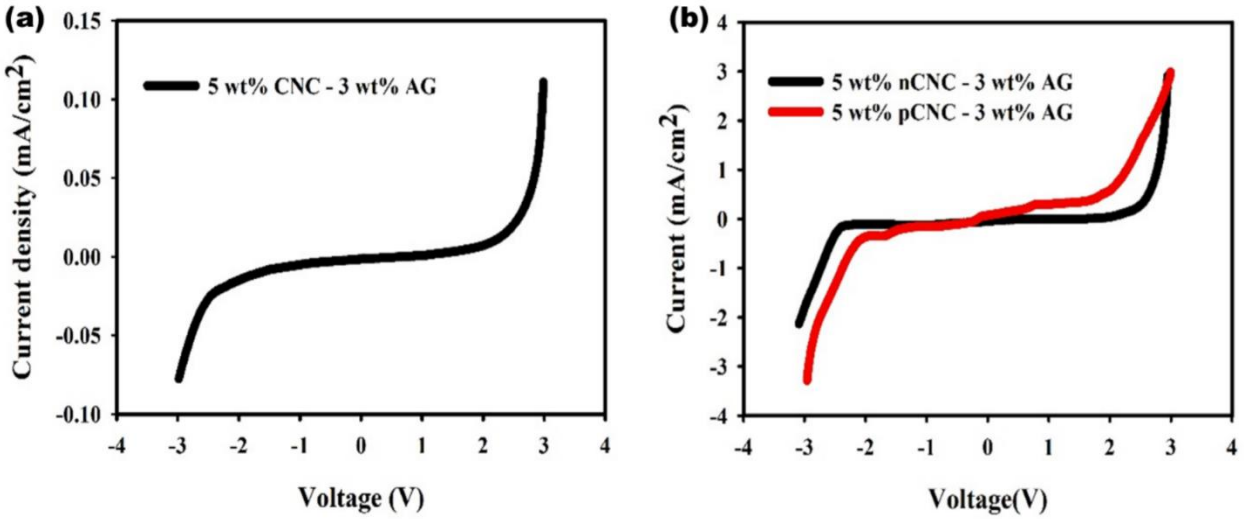

Figure 4. 10 Current as a function of applied bias for single layers of (a) CNC-AG, (b) nCNC-AG and pCNC-AG. Each gel layer was 1.2 mm in thickness and the scan rate was 10 mV/s

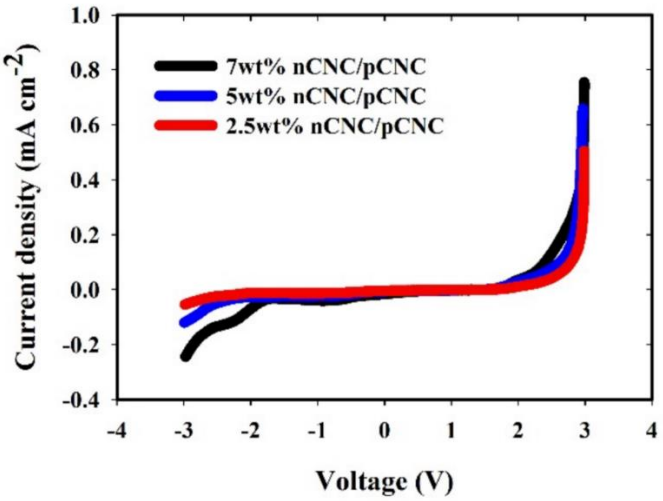

Figure 4. 11 Rectification behavior of the ionic diode prepared by loading agarose with different wt% of nCNC/pCNC before applying a fixed negative bias prior to measurement. the total gel layer was 1.2 mm in thickness and the scan rate was 10 mV/s.

Initially, the rectification of the diode system was evaluated by placing the gel between the electrodes and waiting 5 min before obtaining the *I–V* curve. However, it takes time for the ions to redistribute back to their equilibrium state after each measurement. If not enough time is allowed, the counterions in the system are in a nonequilibrium state before each subsequent measurement. Under such conditions, moderate rectification ratios (ratio of the current at +3 V to the current at −3 V) and current densities were observed (Figure 4.11) The diode system was

pretreated by applying a fixed negative bias of −3 V for 5 min immediately before each measurement, hence driving the migration of ions in gel layers toward the nearest electrode such that each measurement starts from the same state of ion distribution. Consequently, we observed higher current densities of up to 4.5 mA cm^{-2} and rectification ratios of up to 40 (Figure 4.12a).

We investigated several factors that have been shown to influence the rectification behavior of ionic diodes (Figure 4.12). The concentration of nCNC and pCNC in the agarose gel of the asymmetric junctions influenced the observed current density, which subsequently affected the rectification ratio (Figure 4.12a, b). The current density and the rectification ratio increased with a higher concentration of nCNC and pCNC. According to previous studies, increasing the concentration raises the nonreactive counterions in the system,[4] which induce larger potential drops at the electrodes, and higher current densities are achieved in the forward bias, while no change occurs in the negative bias. As a result, there is a significant improvement in rectification. Also, we found that higher current density and rectification ratios are achieved at lower material weight percent compared to the ionic diode generated with microfibrillated cellulose (MFC).[7] This is due to the higher surface area associated with CNCs, which leads to higher charge densities (1.4010 mmol g^{-1} for pCNC and 0.1305 mmol g^{-1} for nCNC) achieved from the surface modification of CNC compared to that of MFC (cf. ∼0.0804 mmol g^{-1} for nMFC and 0.1107 mmol g^{-1} for pMFC), which means that more charge carriers are introduced into the diode system from less material. Hence, smaller quantities of CNCs are required to fabricate a functional ionic diode compared to MFCs.

The scan rate was also found to significantly influence the rectification behavior of the junction diode (Figure 4.12c, d). At 2 mV s^{-1}, the diode exhibited exceptional performance, with maximum current densities in the range of 6 mA cm^{-2} and rectification ratios of 70, which clearly demonstrates a superior performance compared to that of MFC and PDAC/PSS–AG diodes. When the scan rate was increased, the maximum current in the forward bias decreased, which resulted in lower rectification ratios (Figure 4.12d). The observed trend demonstrates the characteristic behavior of ionic current. At low scan rates, the ions have enough time to respond to the applied voltage and the system approaches a steady state, resulting in higher current density and rectification ratios. In contrast, at high sweep scan rates, the movement of ions lags, fewer ions migrate, thus resulting in low currents and rectification ratios.

Similarly, the thickness of the diode, determined by the distance between the electrodes, influenced the performance of the diode (Figure 4.12 e,f). The current density and the rectification ratio decreased as the thickness increased. It is expected that for shorter distances, more charge carriers traverse the entire distance. [4,7]The response time is dependent on the diffusion of ions across the gel and can be estimated by the diffusion time constant (τ_D) = L^2/D_i where L is the distance and D_i is the diffusion coefficient.[1] Hence, the response improves over shorter distances. The CNC–AG ionic diode showed similar behavior, with shorter distances having higher current in the forward bias with no significant change in the conductivity in the reverse bias. As a result, the rectification increased with thinner gel layers.

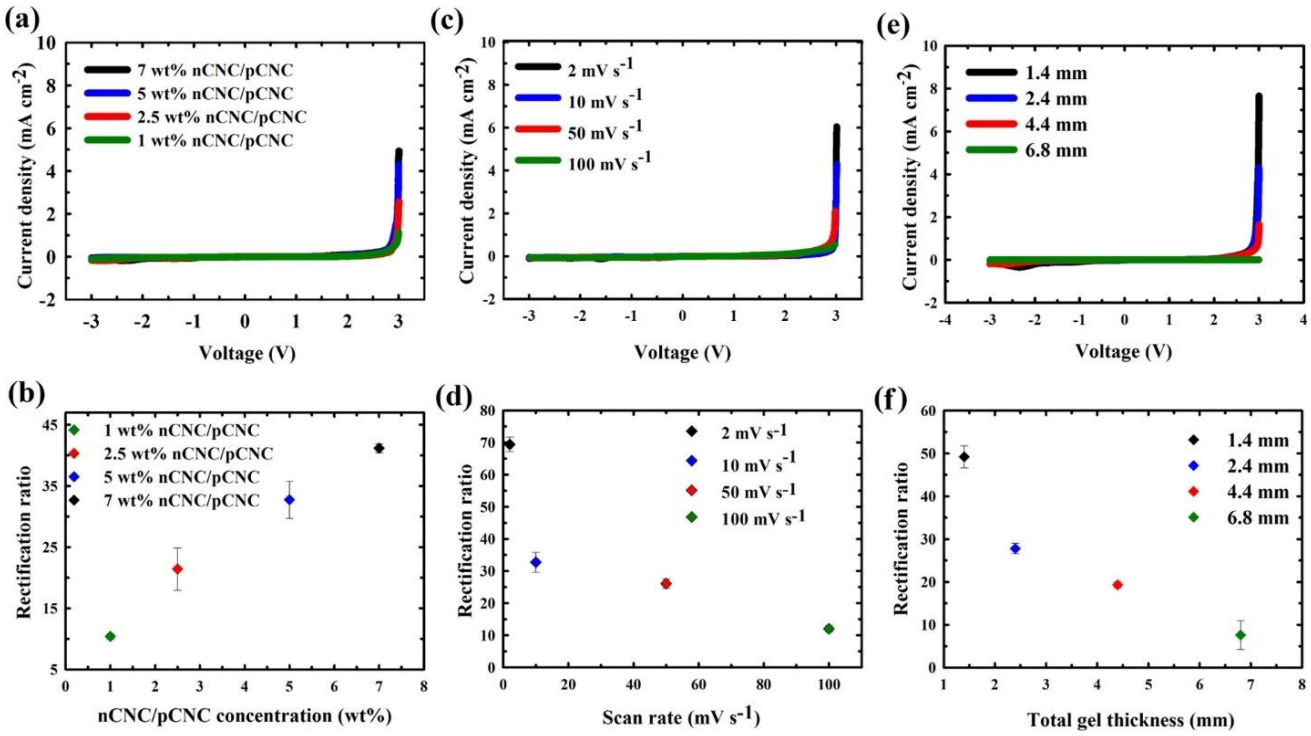

Figure 4. 12 Current–voltage characteristics and the corresponding change in the rectification ratio as a function of wt. % of nCNC/pCNC (a, b), different sweep scan rates (c, d), and gel thicknesses (e, f). Unless otherwise specified, the gel layers had 5 wt. % nCNC or pCNC and a total gel layer thickness of 2.4 mm and the scan rate was 10mV/s.

The influence of background electrolytes was also investigated. nCNCs and pCNCs were purified by dialysis for 10 days to ensure the complete removal of background electrolytes (residual NaOH and $NaHSO_3$ from CNC modification). We then monitored the current response of the ionic diode at varying sweep scan rates and showed that the maximum current density in the forward bias

dropped to 2 mA cm^{-2} from 4.5 mA cm^{-2} before desalination (Figure 4.13), we still observe a rectification ratio of 30, highlighting that the rectification effect is due to nCNC and pCNC.

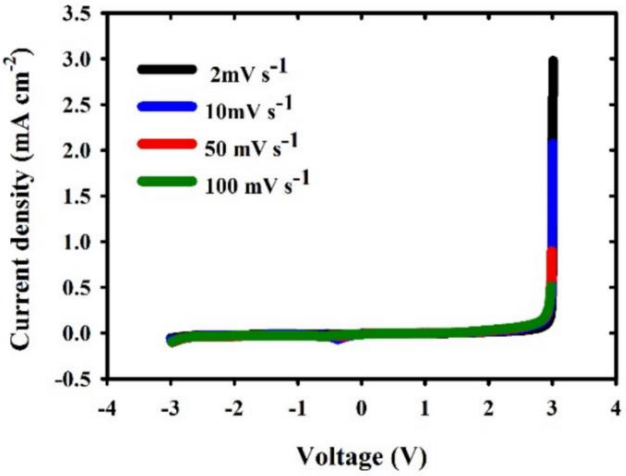

Figure 4. 13 The current-voltage characteristics as a function of different sweep scan rates after desalination. Each gel layer was 1.2 mm in thickness and the scan rate was 10mV/s.

To evaluate how long the device takes to reach a steady-state, the current was monitored as a function of time for a constant forward bias (+3 V) and negative bias (−3 V) (Figure 4.14a). In the first 100 s of the forward bias, the current density decreases abruptly and stabilizes at approximately 0.2 mA cm^{-2}. On the other hand, for the reverse bias, the current deteriorated rapidly (10–15 s) to less than 10 μA. Also, when the same hydrogel was tested in intervals of a week, the rectification behavior of the diode was maintained so long as the hydrogel was prevented from drying (Figure 4.14). These observations indicate the potential long-term performance of the diode. Several parameters need to be considered to get reliable and reproducible results. For instance, the synthesized pCNCs and nCNCs should have consistently the same surface charges from batch to batch. In this respect, Zeta potential measurements can be used to assure consistent surface charges. Sealing the samples as much as possible is another critical factor in order to eliminate evaporations. Finally, the ITO electrodes should be replaced with new ones once degraded.

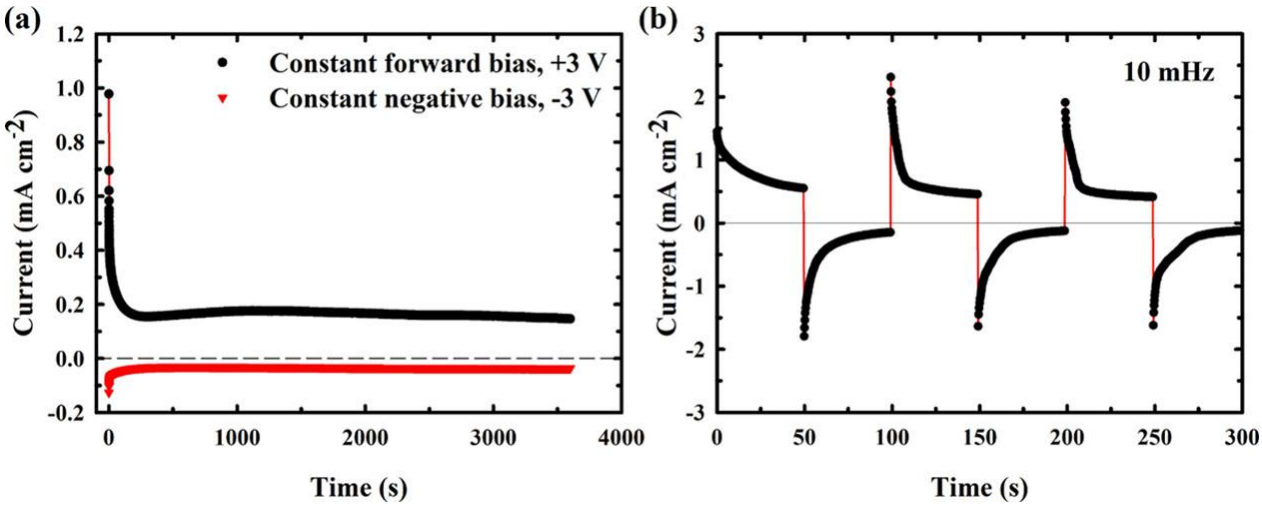

Figure 4. 14 a) Time dependence of the current density under a fixed positive potential of +3V and a constant negative bias of −3 V. (b) Current response of the ionic diode under an AC field of 10 mHz. The total thickness was 2.4 mm, and gel layers had 5 wt % nCNC or pCNC.

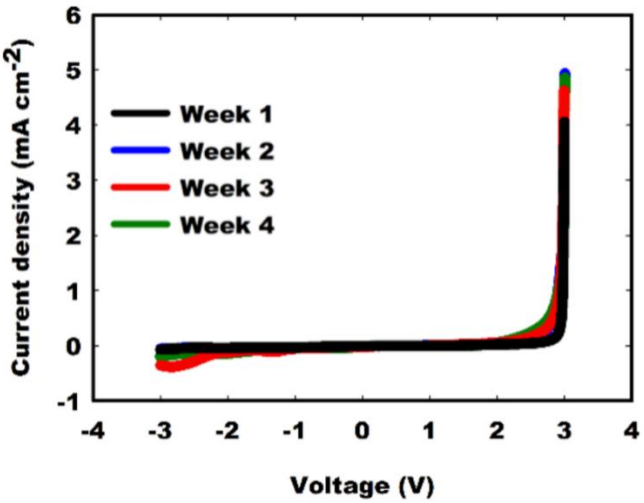

Figure 4. 15 The current-voltage characteristics of the diode tested over four weeks. The total thickness was 2.4mm and gel layer had 5wt% of nCNC or pCNC using a scan rate of 10mV/s.

The transient response of the nCNC/pCNC–AG ionic diode under an alternating electric field was investigated, and the current response was recorded (Figure 4.14b). The diode exhibited good rectification performance for frequencies under 10 mHz. For every alternating cycle of the positive and negative bias, there is a surge in current, which decays and approaches zero in the negative bias and gradually tends to a constant value in the forward bias. As such, poor rectification behavior is observed upon switching between positive and negative bias; however, once the current reaches a steady-state in both directions, the strong rectification of ionic diode performance is

restored. The observed current might be a result of the delayed diffusion response of the ions upon switching the voltage. The duration taken to reach a steady-state is shorter at a lower frequency, effectively restoring the rectification behavior rapidly. This delayed response is an inherent problem in iontronic devices, which relates to how slowly the ions diffuse through a matrix. [3] Nevertheless, given the time to equilibrate, the nCNC/pCNC–AG ionic diode shows steady rectifying behavior.

Additionally, the nCNC/pCNC–AG ionic diode was tested at different applied voltages to investigate potential applications in different power regimes (Figure 4.16a). Rectification behavior was maintained throughout, and no breakdown was observed for voltages up to 5 V. When the applied voltage was increased, the maximum current in the forward bias increased, but there was also a significant increase in the current in the reverse bias, resulting in a decreased rectification ratio.

The transient behavior of the ionic diode at different applied voltages at a fixed frequency of 10 mHz can be estimated from Figure 4.16c,d. The transient response deteriorates as the applied potential is increased. At a lower applied potential, the diffusion-controlled response can keep up with the alternating cycles of positive and negative bias. As such, the nCNC/pCNC–AG ionic diode is suitable for use in low-energy-consumption devices, which is ideal for biointegrated electronics.

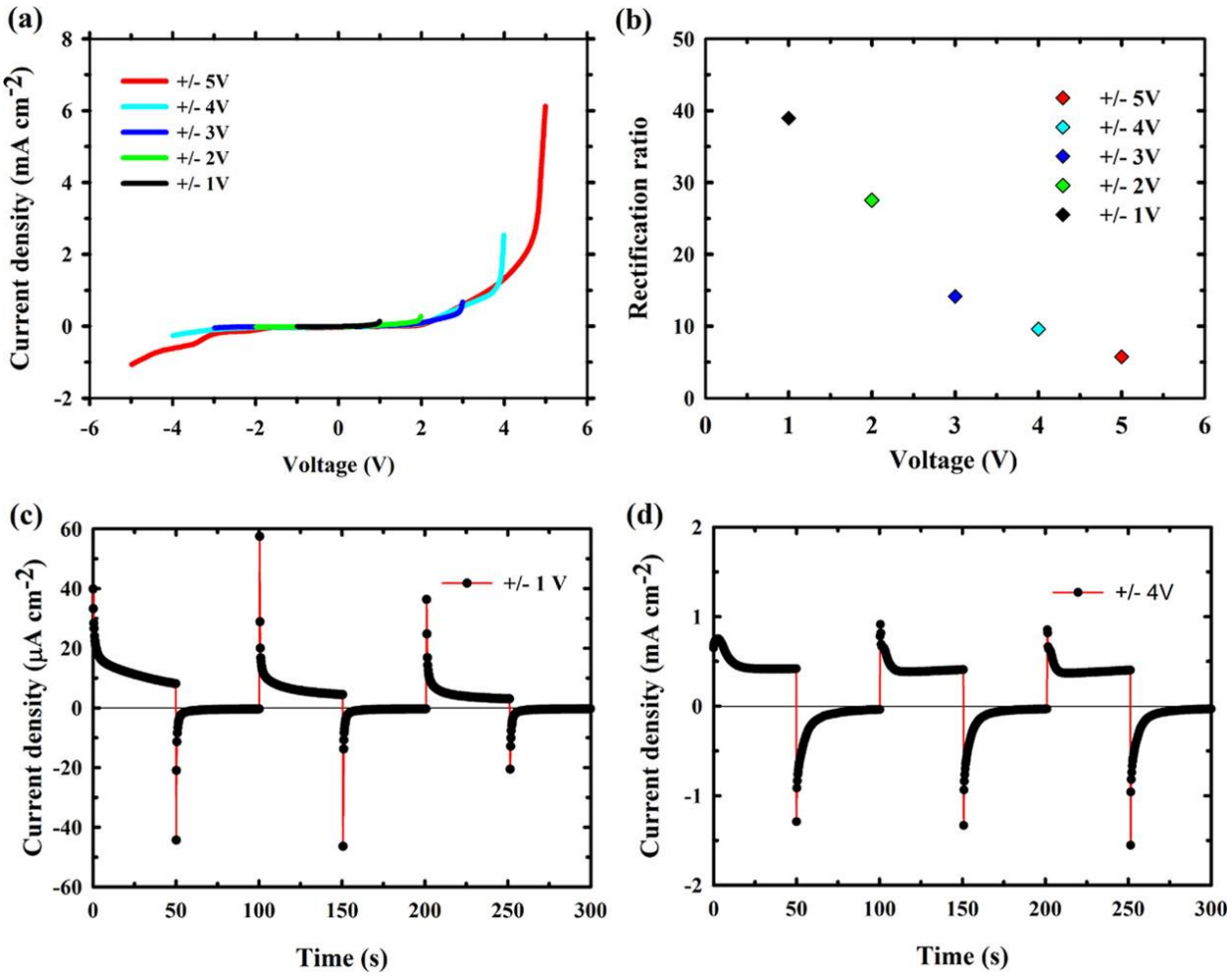

Figure 4. 16 (a) Current–voltage characteristics of the ionic diode under different applied potentials and (b) change in the rectification ratio (gel layers had 7 wt. % nCNC or pCNC, and the scan rate was 10 mV s–1). The observed transient behavior of the diode at applied potential of (c)±1V and (d) ±4V.

Although different parameters have been used in the reported rectification ratios of different ionic diodes, the rectification ratio obtained in this work is unusually high, with values up to 70. On the other hand, the observed current densities are in the range normally observed for ionic junctions (0.1–10 mA cm^{-2}). The performance of the diode in terms of maximum rectification is on par or in some cases better than that in ionic diode devices that employ the commonly used nonbiodegradable polyelectrolytes.

High rectification ratios are ideal for ionic diodes as they signify efficient control of ions. This control is essential to realize logic units or to perform effective delivery of chemicals/ions in integrated ionic circuits. In addition, this enables the control of ionic currents in actuators, energy

converters, and wearable devices. Iontronics are far from outperforming silicon-based electronics; however, they possess advantages such as potential for low-cost, flexible, low weight, and in particular environmentally friendly microelectronic devices.[51,4] The results presented here highlight the potential application of surface-functionalized cellulose nanocrystals as building blocks in biodegradable, cheap, biosourced, and biocompatible electronics.

4.5 Summary

In this chapter enhanced rectification behavior has been demonstrated from a system composed of two agarose hydrogels doped with surface-modified cellulose nanocrystals (CNCs). The advantageous properties of CNCs enabled fabrication of a functional, stable diode. By combining stretchable hydrogels and CNCs, a mechanically strong biodegradable hydrogel ionic diode was designed. The high surface area of CNC resulted in high charge density after surface modification, which in turn resulted in good rectification behavior from only small amounts of dopant material. As such, we have shown how CNC, a bio-sourced, biodegradable, inexpensive, and renewable material, can be a potential replacement for the conventional polymers that have been employed for the fabrication of polyelectrolyte ionic diodes. The significance of this development is envisaged in the use of surface-modified cellulose nanocrystals as functional components in biodegradable electronics such as sensors, energy harvesters, or logic gates.

Chapter 5: The Rectification Mechanism in Polyelectrolyte Gel Diodes

In the previous chapter, the fabrication of a cellulose nanocrystal (CNC)–agarose (AG) polyelectrolyte gel diode was presented exhibiting exceptional rectification behavior.[89] In this chapter extensive electrochemical characterization of this diode via potentiometric and impedance spectroscopic methods is presented to test the Yamamoto and Doi theory. [1]

Yamamoto and Doi [1] offer a comprehensive model for the working mechanism behind PGDs. The model is quite remarkable given the relative simplicity of its assumptions such as the immobility of the polyelectrolyte network and the presence of a sharp boundary interface. Triandafilidi et al previously studied the assumptions and results of the theory via molecular dynamics (MD) simulations of asymmetric polyelectrolyte gel networks. [90] The MD simulation employed a coarse-grained model of a PGD in the static regime, with a movable and stretchable network to analyze ion density and electric field distribution in the system. They have shown that the electrical field distribution predicted by the Poisson–Boltzmann (PB) model used in the Yamamoto and Doi theory still holds for the case of a movable network, provided the system is in the entropy dominated regime with low Bjerrum lengths. These MD results have stress-tested some assumptions of the Yamamoto and Doi theory in the static regime. However, these simulations did not study the applicability of the theory to predict experimental PGD behavior, especially in the dynamic regime with water electrolysis at the electrodes.

Herein, an attempt is made to bridge the gap between the theoretical models and experimental data and provide additional insight into the mechanisms involved in the current rectification in polyelectrolyte gel diodes.

5.1 Theoretical background: Yamamoto & Doi theory

The electrochemical model presented by Yamamoto and Doi provides a thorough explanation of the operation of PGDs. (28) The main argument lies in the electrochemical reactions at the electrodes, where water is split into two ions, H^+ and OH^-, and their subsequent transport to the interface between the gels. To explain the operation of the PGD, we will first look at the static

regime, when the electrochemical reactions at the electrodes are suppressed, followed by the regime when water can dissociate and, due to this, currents appear.

In the static regime (Figure 5.1a, b), floating counterions in the bulk of the gel remain close to their respective backbone to preserve the local electroneutrality, generating a bulk potential ψ_f. At the interface between the electrode and the gel, as well as the gel-gel junction, they re-equilibrate themselves and follow a Boltzmann distribution. When a reverse bias is applied ($V < 0$) the free anionic and cationic counterions migrate from the gel-gel interface towards the nearest electrodes to minimize the Helmholtz free energy and form an electric double layer at the electrode-gel interface (Figure 5.1a). Since the neutralization of the electrode surfaces occurs at the expense of the ions present at the gel-gel interface, the number of counterions at the junction decreases. This results in large potential drops that are felt at the interface between the gels, as well as small potential drops at the electrodes also referred to as overpotentials (ΔV).

When a positive bias is applied ($V > 0$) the electrodes repel the counterions in the vicinity of the electrode-gel interface towards the gel-gel interface (Figure 5.1b). This creates a large potential drop that is felt at the surface of the electrode. The migrating counterions populate the "depletion zone" at the gel-gel interface and lower the bulk potential ψ_f. The magnitude of the overpotentials that are "felt" at the electrode surfaces becomes fundamentally important when the PGDs are studied in the non-static regime.

In the non-static regime (Figure 5.1 c-d), currents are no longer suppressed and the electrochemical reactions at the electrodes generate additional charges, i.e., electrolysis of water occurs. Water is oxidized at the anode when the applied voltages reach +1.23 V; generating H^+ ions ($2H_2O \rightarrow 4H^+ + O_2 + 4e^-$). Similarly, at the cathode water is reduced at applied voltages lower than -0.83 V to produce OH^- ions ($2H_2O + 2e^- \rightarrow 2H_2 + 2OH^-$). The rate of H^+/OH^- generation follows Butler-Volmer kinetics (equation 5.1) and takes the form of equations 5.3 and 5.4 in the electrochemical model.

Equation 5.1 is the simple form of the Butler-Volmer equation. If the polyelectrolyte solution is well mixed and stirred, or currents passing through the device are kept low so that the concentrations at the electrodes do not differ appreciably from the concentration in the bulk of the

polyelectrolyte, then this equation gives a good representation of the current as a function of the potential.[91]

$$J = J_0[e^{-\alpha\Delta V} - e^{(1-\alpha)\Delta V}] \tag{5.1}$$

$$J = J_{cathode} + J_{anode} \tag{5.2}$$

$$r_H = J_o\left[e^{\Delta V} - 1\right] \tag{5.3}$$

$$r_{OH} = J_o\left[e^{-\Delta V} - 1\right] \tag{5.4}$$

Where J_0 is the exchange current density (the rate of reactions at equilibrium $\Delta V = 0$ on one side (forward or backward bias), α is the charge transfer coefficient and in most experiments, α appears to be constant. In most electrochemical systems, α has the value between 0.3 and 0.7, and in the absence of actual measurement can be considered equal to 0.5, F is the Faraday constant, R is the universal gas constant, T is absolute temperature and ΔV are overpotentials (defined as V-V_o) r_H and r_{OH} are the rate of the reaction and the reaction rates respectively which can be described as

$$Rate(mol\ s^{-1}cm^{-2}) = \frac{J}{nF} \tag{5.5}$$

Where n is the number of electrons transferred in the electrode reaction.

Due to the appearance and the consequent diffusion/migration of H^+/OH^- ions, the current generation process becomes limited by both the kinetics (due to the oxidation/reduction) as well as the transport of these ions.

It is noted that equation 5.1 consists of two components, the first term represents the cathodic contributions, and the second term the anodic components. For large positive overpotentials, the cathodic component is negligible, and the total current is the same as J_{anode}. As known, the oxidation occurs at the anode and causes the generation of H+. Therefore, equation 5.3 is only effective for $\Delta V > 0$. The same applies for equation 5.4. For large negative overpotential, the anodic component is negligible, and therefore the overall current is equal to $J_{cathode}$. At the cathode, the reduction reaction take place resulting into the generation of OH-. Therefore, hydroxide ions are

produced at electrodes to which negative voltages are applied and ultimately equation 5.4 is only valid for $\Delta V < 0$.[91]

Without loss of generality, we orient our gel to have positive backbone (negative mobile counterions) at the anode (where H^+ ions are generated), and negative backbone (positive counterions) at the cathode (where OH^- ions are produced). In reverse bias, overpotentials (ΔV) "felt" at the electrodes are small resulting in inhibited kinetics. The few H^+ that appear at the anode migrate to the interface between the gels to associate with OH^- (a similar reaction takes place on the opposite electrode). The migration, however, is heavily screened by the negatively charged mobile floating counterions, thus inhibiting the currents in the reverse bias regime.

When a positive bias, $V > 0$ is applied, counterion density profiles, as well as the potential profiles remain similar to the static regime, where the electrochemical reactions were suppressed, with large potential drops at the electrode surfaces, catalysing the kinetics. This produces large amounts of OH^- ions (and H^+ on the opposite electrode) at the surfaces of the electrodes. Also, the migration and diffusion of produced OH^- ions are no longer inhibited as there are no floating counterions to be able to screen them effectively (as they bear the same charge), hence this function is being performed by the positively charged fixed ions (at least for small voltages) resulting in exponential currents.

In the negative bias, for applied voltages ($-V$) that are smaller than the bulk potentials i.e., $-V < 2\psi_f$ (whereby the bulk potentials are approximately equal to $10k_BT/e$, the currents are independent of the gel ionization. This is because, for small voltages, the migration of OH^- and H^+ ions is largely influenced by the negatively and positively fixed ions, respectively. This results in significant screening (hindering the movement) which results in small currents. In contrast, when the applied bias becomes larger than the bulk potential i.e., $-V > 2\psi_f$, the attractive electrostatic force is sufficient to drive the migration; even in the presence of repulsive forces from the stationary/fixed ions. As such, from that point the current is dependent on the ionization.

In summary, the electrochemical model can be summarized by three hypotheses behind the ion generation and flow. First, ion generation occurs at the electrodes due to the electrolysis of water. The current rectification occurs due to subsequent ion flow through an asymmetric media (e.g., p-

type and n-type). Second, in forward bias the theory predicts exponential currents, independent of concentration of dopants, and smaller currents for higher concentrations. Lastly, in backward bias the theory predicts $J = A\sqrt{-V}$, with A inversely proportional to the gel ionization

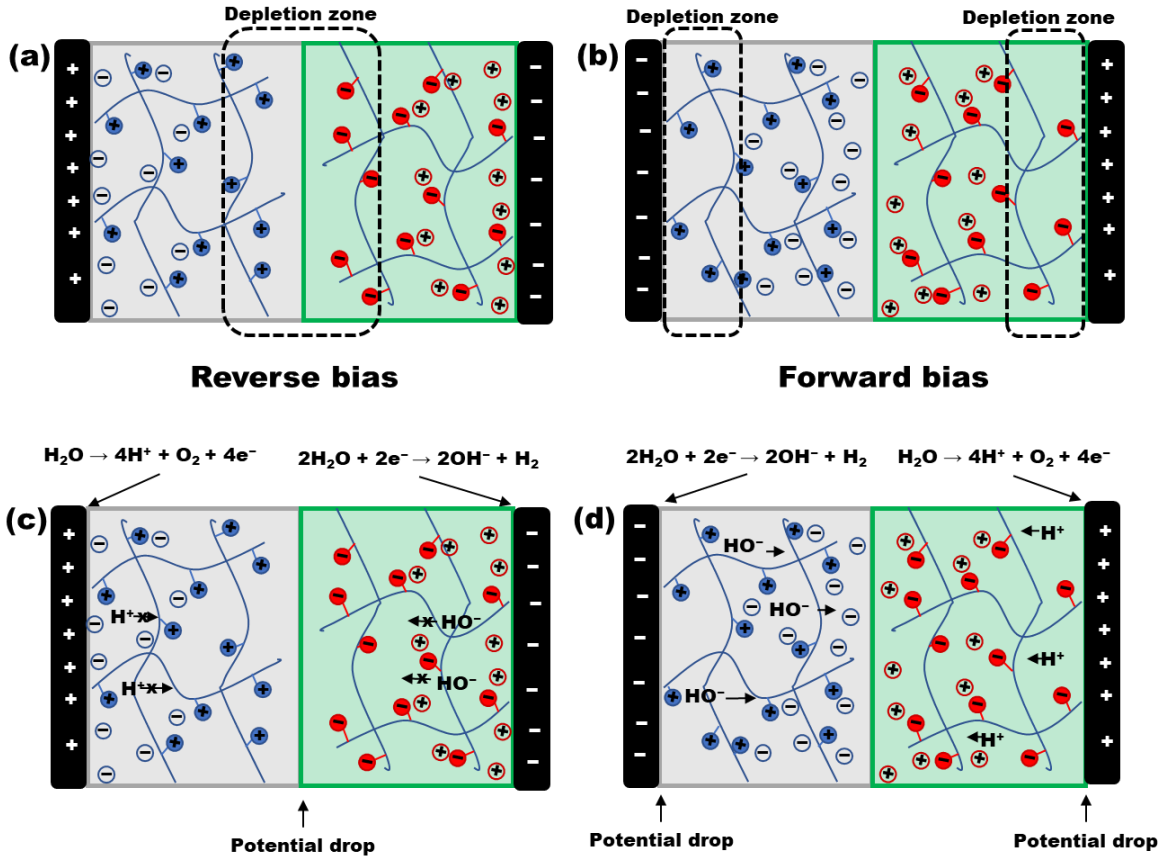

Figure 5. 1 Rectification mechanism of polyelectrolyte gel diodes under (a) backward bias and (b) forward bias under static regime; (c) and (d) under non-static regime.

5.2 Generation and asymmetric distribution of ions

Electronic Impedance Spectroscopy (EIS) was used to understand the electrochemical behavior of the polyelectrolyte gel diode by providing evidence for the occurrence of Faradaic current due to the electrolysis of water. A sine curve is applied to the material, varying the frequency from 0.01 Hz to 1 MHz at an amplitude of 40 mV or 1V. To fit the data, the Randles equivalent circuit model for an electrode immersed in an electrolyte is used (Figure 5.2b), which assumes the presence of both Faradaic and non-Faradaic currents. Faradaic current is accounted for by the polarization resistance (R_p) and the solution resistance (R_s), while the non-Faradaic current resulting from

charging the double layer is represented by the double layer capacitance (C_d). The mass transport of the products of the electrochemical reaction dictates the amount of the observed current and is represented by the Warburg impedance (W).

The obtained EIS results (Figure 5.2c) highlight the presence of the double layer capacitance, indicating that non-Faradaic processes are occurring. At low frequencies, the real part of an impedance of the capacitor C_d is infinite. As the frequency is increased, the current going through the capacitor increases as its impedance decreases until it is fully short-circuited indicated by the onset of a half-circle. In addition, the low frequency feature (straight line) highlights the mass transport characteristic of the Faradaic current. These observations confirm the underlying assumption in the electrochemical model that the observed currents are due to the electrolysis of water.

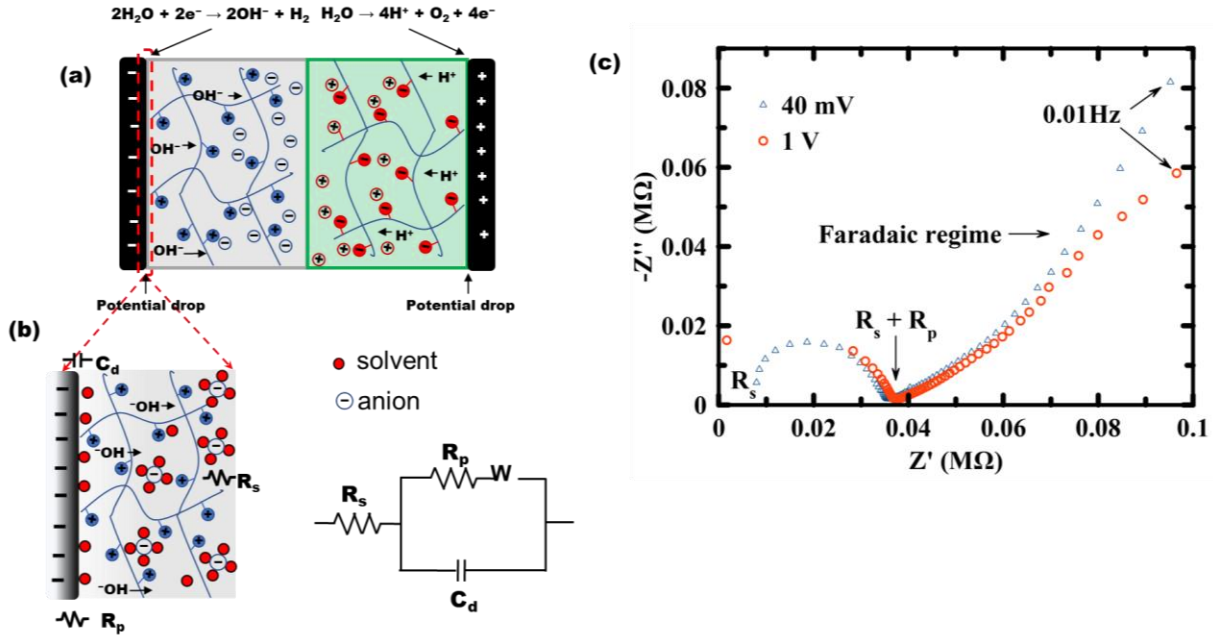

Figure 5. 2 (a) Schematic elastration of the CNC-AG diode and (b) the interface between the electrode and polyelectrolyte hydrogel and the corresponding Randles equivalent circuit. (c) Experimental impedance spectra for CNC-AG diode.

5.3 Rectification under voltage sweep

Having demonstrated that charges appear due to electrolysis, the importance of asymmetry in the gel network was investigated to show its importance for rectification. Linear sweep of applied voltages produces current-voltage *J(V)* curves shown in Figure 5.3. In the case of a gel containing only one type of charged dopant, the *J(V)* curve is symmetric (Figure 5.3). In contrast, when we interface two gels containing a cationic dopant on one side and an anionic dopant on the other (Figure 5.3), a pronounced current is observed in the forward bias and very little current in the reverse bias. Figure 5.3 shows the rectifying mechanism of the PGD, whereby there is a large exponential increase in current for the forward bias and small currents in the reverse bias regime. This characteristic behaviour has been reported for polyelectrolyte gel diodes that operate by the same mechanism. [92-93] The exponential increase in the current only starts after an applied bias of 1.23 V, which corresponds to the standard electrode potential for the electrolysis of water. This is in accordance with the EIS results whereby the presence of Faradaic current was observed, confirming that the mechanism of current generation in aqueous based PGDs involves water splitting. When the applied voltage is smaller than 1.23 V, we observe small negative electric currents. These currents increase in magnitude as we increase the negative bias and at a bias of ~ –2V, the *J(V)* curve becomes steeper. The increase in the slope of the curve is due to the breakage of the diode.

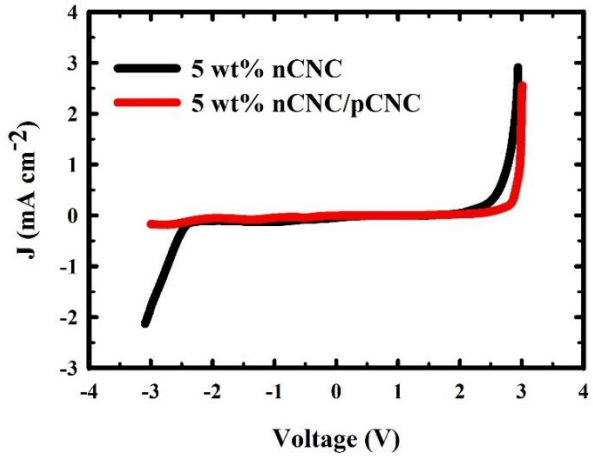

Figure 5. 3 The resulting symmetric J(V) curve (black) for a gel layer with one charge and the asymmetric J(V) curve (red) characteristic of rectification for two oppositely charged gel layers. Obtained by sweeping through voltages –3 to 3 V at a scan rate of 10 mv s^{-1}.

The rectification mechanism is dependent on the gel–gel and gel–electrode interfaces. These interfaces significantly influence the functionality and performance in hydrogel bioelectronics. Factors that affect interfaces must be carefully considered for optimum performance. These include good adhesion and prevention of interface separation due to dehydration.[93] Strong adhesion at the gel–gel interface has been shown to result in diodes with improved performance. [92,88] This could be due to better distribution of the electric field under positive or negative bias, which would result in better control of the potential drops at the interfaces.

Another essential factor that influences the operation of PGD is the distribution of counterions present in the system. These influence the electrostatic potential drops, either at the interface between the gels or the electrode gel interface.[94] In turn, they control the rate at which H^+ and OH^- ions are generated by the electrochemical reactions. Using molecular dynamic simulations of asymmetric polyelectrolyte gel networks, a coarse-grained model of a PGD in the static regime with a movable and stretchable network has been used to analyse ion density and electric field distribution in the system, while the electrical field distributions predicted by the PB model have been verified.[90]

Experimentally, the importance of ion distribution can be clearly seen by measuring the J(V) curves of the diode starting from steady state or non-steady state ion distribution. The non-steady state sweep experiments were conducted by connecting the diode and immediate application of scanning voltage from +3 V to −3 V (Figure 5.4 run 1-3). Initially, the ions are randomly distributed in the system (run 1), and due to the time lagging of the ions with respect to the applied potential field, a significant amount of current is observed in the backward bias. The successive measurements of the same diode (run 2 and 3) exhibit improved performance as the ions distribute closer to steady state. Thus, a steady state ion distribution can be achieved by applying a constant reverse-bias voltage before each sweep experiment. As such, a fixed negative bias of −3 was applied initially for 5 min followed by the sweep experiment (Figure 5.4 run 1-3 with bias). Since the ions are initially in a steady-state distribution, the diode performance is superior compared to the first non-steady state run (Figure 5.4 run 1 vs. run 1 with bias). Subsequent measurements are also improved as the ions again move towards their steady state (run 2 and 3 with bias). The maximum current in the forward bias decreases for both run 1-3 and runs 1-3 with bias. This is

reminiscent of the observations in step experiments (Figure 5.5), whereby there is a large increase in the current followed by reduction to a constant value; indicating the system has moved towards its steady state. These observations indicate how the current is generated only from limited ions that can interact in the time frame of the potential sweep scan.

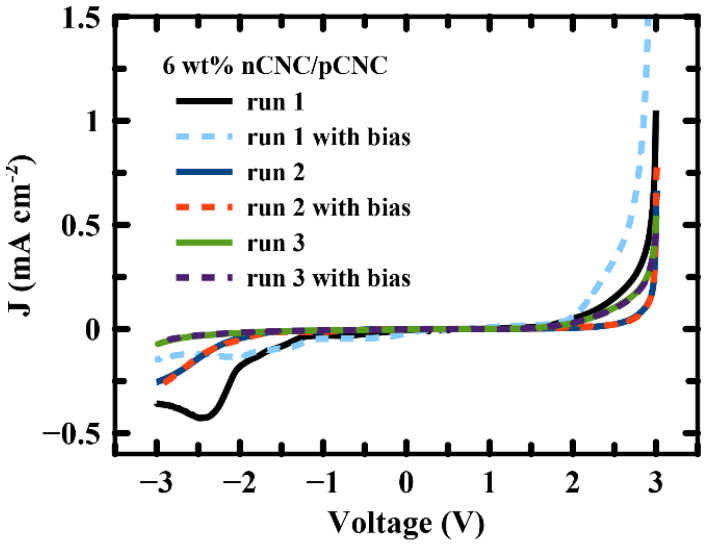

Figure 5. 4 Influence of distribution of counterions in the non-steady state and in the steady state on rectification.

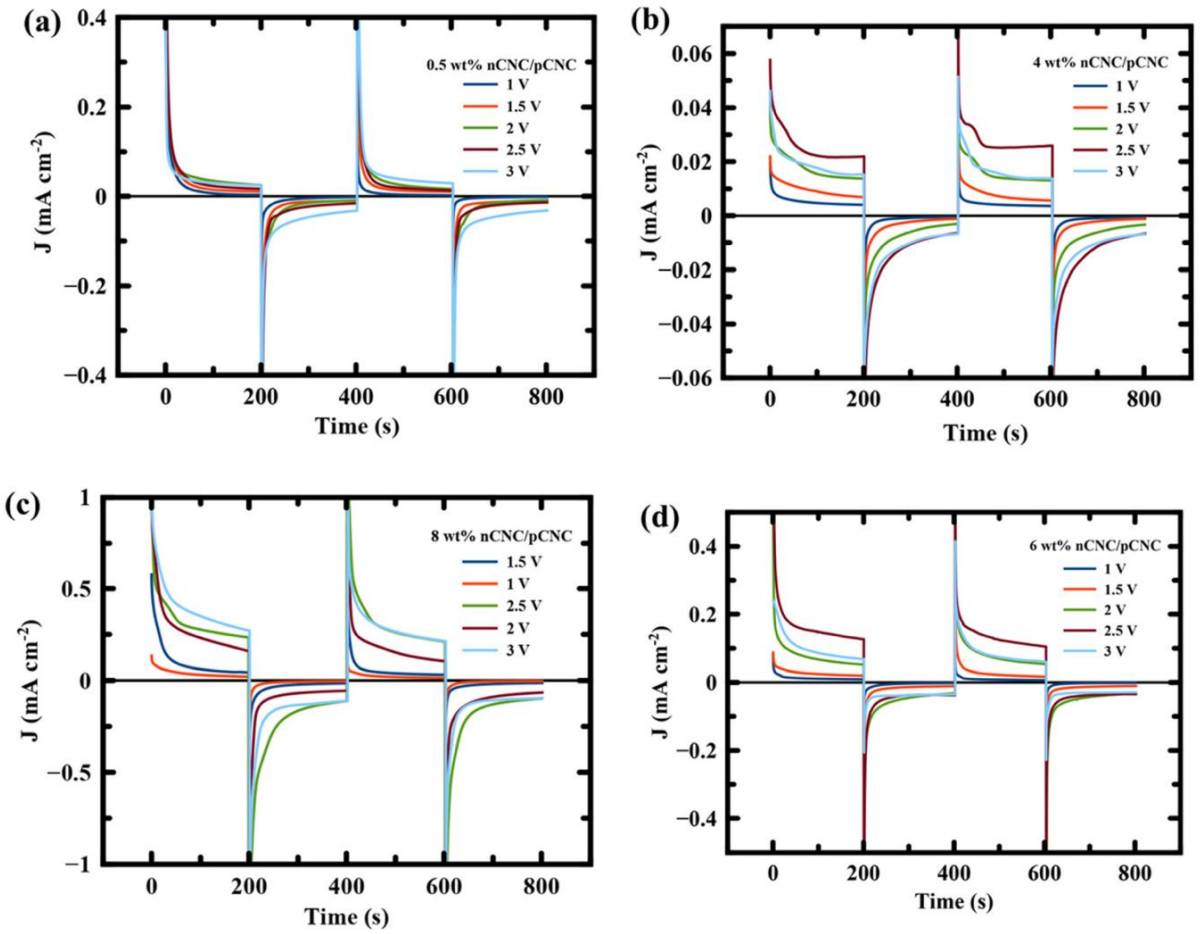

Figure 5. 5 The step biases were performed at various applied voltages.

5.3.1 Forward bias

Having confirmed the underlying assumption made by Yamamoto and Doi, that current is generated from H^+ and OH^- and the importance of gel asymmetry for rectification, we move to rationalize the experimental observations in the forward and reverse bias of the J(V) curve. For the forward bias, the nonreactive counterions migrate towards the interface between the two gels, creating an ion deficiency at the interface between the gel and electrode. The fixed charges in this region lead to the applied potential being localized at the gel electrode interface creating a large potential drop that accelerates the electrolysis reactions at the electrodes. The theory predicts Butler-Volmer like kinetics of water electrolysis at the surfaces of the electrodes. The ions generated diffuse through the system resulting in exponential currents described by equation 5.3 When the forward bias becomes large enough, the exponent becomes much larger than 1 and the equation could be further simplified to the following equation.

$$\frac{J}{J_o} = e^{\Delta V} \tag{5.6}$$

A simple relationship between the current and applied bias is obtained, whereby $J/J_o \rightarrow e^{\Delta V}$ when $\Delta V \rightarrow \infty$. Since $\Delta V = V - V_o$, we approximate $\Delta V \approx V$ to test the predictions of the electrochemical model. We plotted log (*J*) as a function of *V* (Figure 5.6), which according to the electrochemical model should be linearly proportional. Indeed, starting from 1.23 V the experimental data falls on the predicted linear fit (Figure 5.6b). Also, the proportionality constant between log (J) and V was calculated to be $J_o \approx e^{-7} \approx 1 mA cm^{-2}$ via linear regression analysis. J_o represents the exchange density and is a point were there is no net current in an electrochemical cell and is intrinsic to the electrode material.

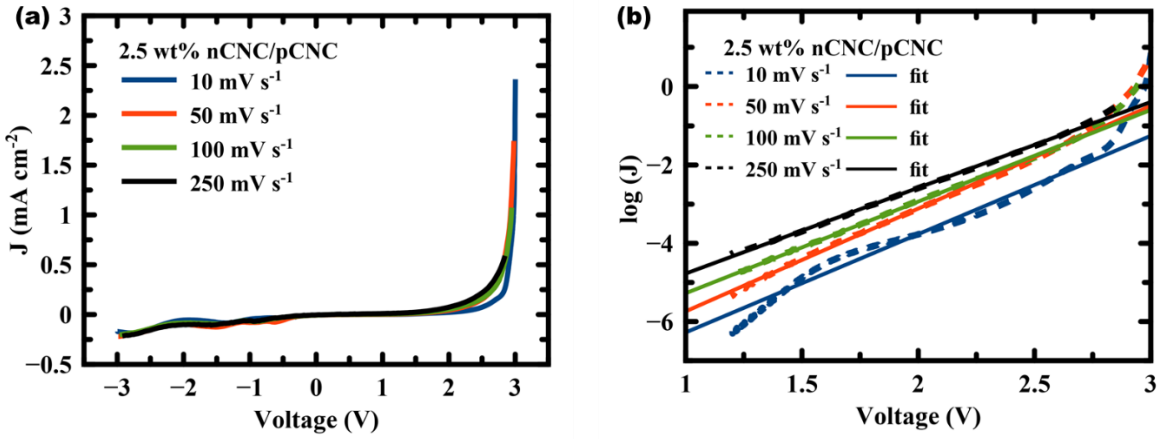

Figure 5. 6 (a) J(V) characteristics at different sweep rates and (b) Log J(V) curve and the corresponding data fit for the forward bias. Log J(V) curves obtained by taking terminal values of currents in in the forward bias at corresponding applied voltage and fitting of J~$e^{-\Delta V}$

The electrochemical model does not discuss the influence of sweep scan rate on the performance of the diode; however, it successfully predicts the exponential increase in current in the forward bias. The scan rate also considerably influences the magnitude of current and hence affects the rectification behaviour of PGDs. Increased scan rates result in lower maximum current in the forward bias (Figure 5.6a). The observed trend reinforces the characteristic behaviour of ionic current that has been observed in other ionic diode systems. At low scan rates, the *J*(*V*) characteristics are more asymmetric because there is sufficient time for ions redistribution in

response to the change in applied voltage. This results in higher current density and rectification ratios. Conversely, at high sweep scan rates, ion movement is sluggish causing fewer ions to migrate and thus leading to low currents and rectification ratios. Hence, a theoretical approach would be noteworthy to look into this as it may result in a quantitative relationship between the scan rate and the diode performance.

5.3.2 Backward bias

Conversely, in the negative bias, the nonreactive counterions migrate towards the nearest electrode, creating a depletion region at the interface between the two gels. These fixed charges in this region localize the applied potential at the gel-gel interface creating a large potential drop in this region that suppresses the electrochemical reaction at the electrodes and significantly reducing the rate of electrolysis. In addition, in this regime the overpotentials at the electrode surfaces are relatively small, and the diffusion of the H^+, OH^- is hindered by the floating counterions. As a result, the theory predicts much smaller currents for a given voltage and the relationship between the observed current and applied voltage is $J = A\sqrt{-V}$. As expected, by fitting J against applied voltage (Figure 5.7) we find a slope of ½ and a close match to the experimental data. In addition, the log-log plot of the J(V) data in the backward bias and linear regression fit of the data before the diode breakdown (0 to ~ -2V) (Figure 5.8) yields a slope of ~ 0.5. As such, the Yamamoto and Doi theory has been able to predict current behavior in both the backward and forward bias under potential sweep.

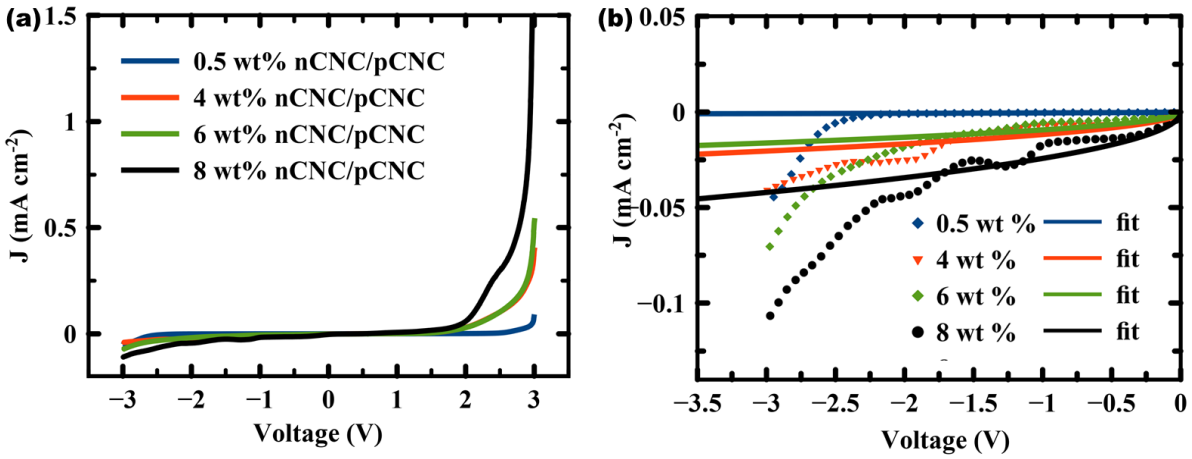

Figure 5. 7 J(V) curve and the corresponding data fit for the backward bias. Results were obtained by sweeping through voltages -3 to 3 V with the rate of 50 mV s^{-1}.

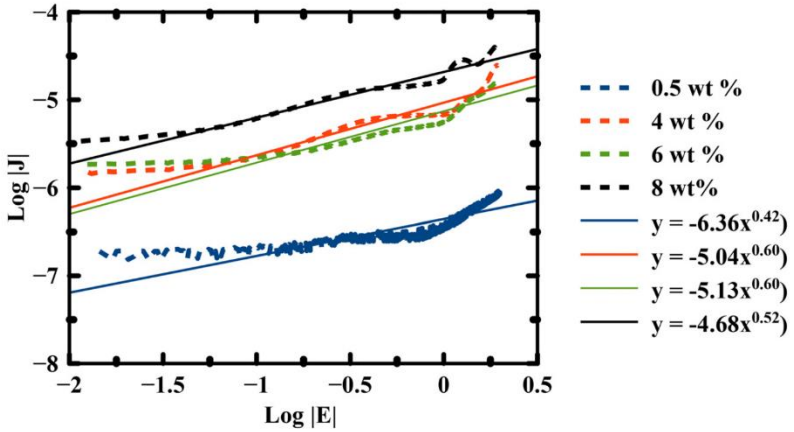

Figure 5. 8 Log–Log plot of J(V) curve (absolute values from 0 to ~ 2) in the backward bias and the corresponding linear regression fit.

5.4 Rectification under step voltage

Evident from the data presented above and from numerous reports on PGDs, the scan rate significantly influences the rectification behaviour under a continuous linear sweep. This is observed as changes in current for both the forward and backward bias. This is unsurprising since the applied potential field between the electrodes is continuously changing, therefore the ions are in a non-equilibrium state due to lagging. Hence, to analyze the steady-state currents at the electrodes in the forward bias (J_+), and backward bias (J_-), as a function of applied positive bias (V_+) and negative bias (V_-), an alternating voltage (step bias) was applied and the evolution of

current as a function of time was monitored. This enabled the establishment of a connection between the current and the formation of a double layer and the movement of ion.

Based on the assumptions of the Yamamoto theory, the observed current decays exponentially as the electric double layer discharges and reaches a steady current at equilibrium. In each case, when alternating between a positive bias and a negative bias, there is an initial spike in current followed by an exponential decay (Figure 5.5). As expected, the equilibrium current in the forward bias was much larger than the equilibrium current in the reverse bias, *i.e.*, $J_+ >> J_-$. The curves equilibrate within $\tau_{eq} \approx 50-100s$ suggesting the diffusion constant $D \approx L^2 / \tau_{eq} \approx 10^{-4} cm^2 / s$ (for this system L ≈ 1 mm) which coincides with the theoretical data for the OH^- and H^+ diffusion constants.[1] Fitting the step curves and with an exponential function and comparing the rates of decay for different ionizations of the gel (Figure 5.9), we observed that the wt.% does not affect the rectification behaviour of the system.

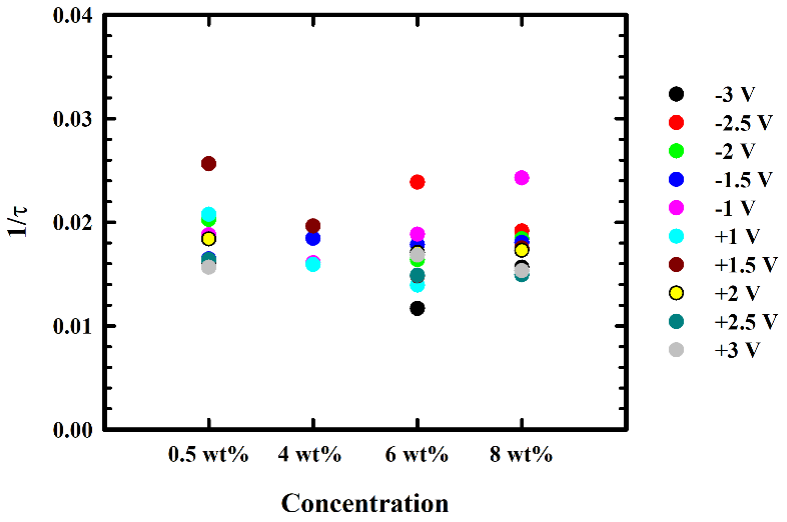

Figure 5. 9 Decay constant variation during alternating step bias at different applied potentials.

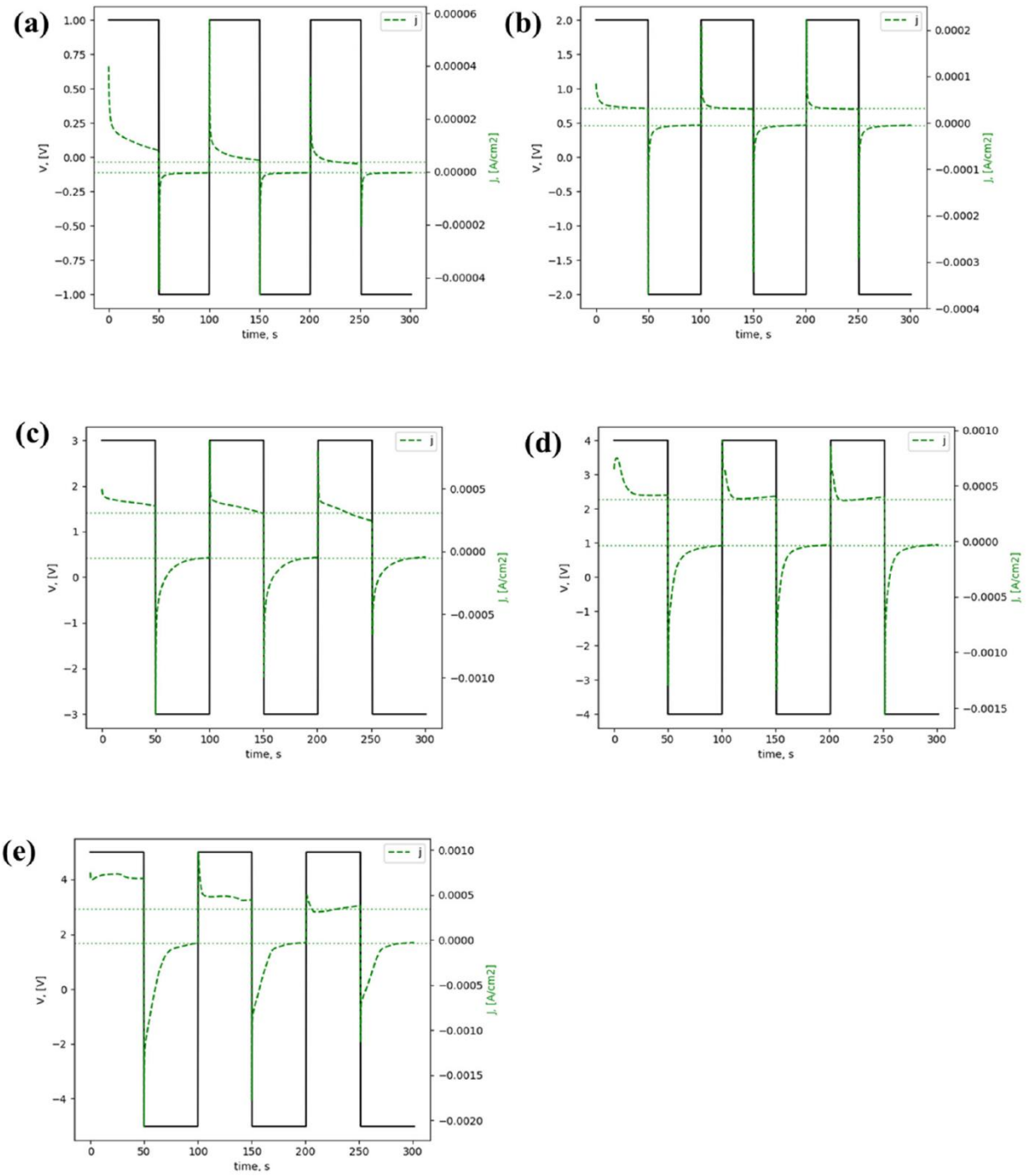

Figure 5. 10 Step biases performed at applied voltages of ±1 V, ±2 V , ±3 V , ±4 V and ±5 V.

The step biases were performed at applied voltages of ±1 V, ±2 V , ±3 V , ±4 V and ±5 V (Figure 5.10) , and the terminal values of $J_{\pm}$ for both the backward and forward bias were compiled as a plot of terminal, J, against applied voltage. The graph obtained (Figure 5.11) mimics the data for

the linear sweep. However, there is a difference in the magnitude of ionic currents in both the forward and backward biases. This discrepancy originates from the slow equilibration of OH^- and H^+ ions as they migrate from the electrodes to the junction between the gels. When a voltage sweep or step bias are applied, a double layer is formed at the interface between the gel and the electrode. The Maxwell-Wagner effect describes how the charge accumulation between the two interfaces occurs within the relaxation time, $\tau = \varepsilon / \sigma$, where ε is the dielectric constant and σ is the conductivity.[95] The relaxation time takes the form of the Maxwell-Wagner time of $\tau = \lambda_D^2 / D$, where λ_D is the Debye length and *D* is the diffusion constant. The double layer formation happens relatively fast within the Maxwell-Wagner time, which is in the range of 1-100 nanoseconds However, ions require additional 50-100 s for slow driven diffusion through the sample until they reach the gel junction and recombine to form water. Upon application of step bias the system can equilibrate to equilibrium currents of $J_{\pm}$. When sweep bias is applied (e.g., 50 mV s^{-1}) the voltage changes by 50mV/s × 60s = 0.3V within the equilibration time which in its turn changes the observed currents. Hence, a careful match against the electrochemical model requires a careful observation of the steady state currents which has been done under the step bias.

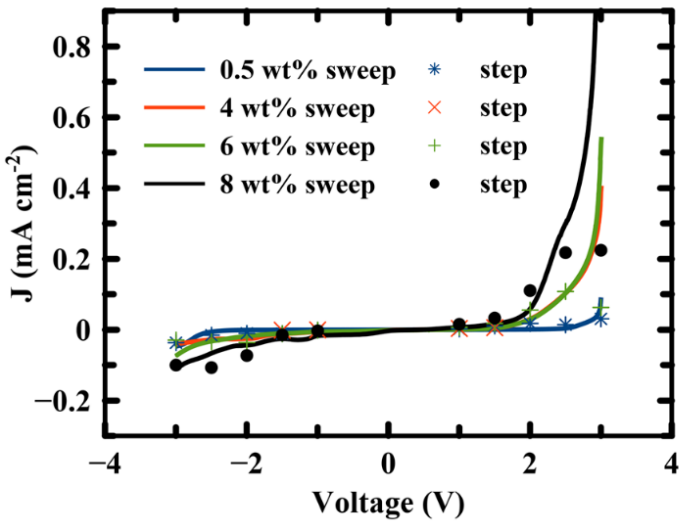

Figure 5. 11 nCNC/pCNC polyelectrolyte gel diode response under step voltage input. Green lines indicate the terminal value of the currents in the backward and forward bias

Based on the electrochemical model, the results discussed for the forward and backward bias highlighted the expected trends in current density. The magnitude of the observed current is also an important aspect that dictates the performance of the diode. Concentration, sweep scan rates, and gel thicknesses have been discussed to influence the magnitude of current. [74,89] The electrochemical model predicts that for increasing concentration, reverse currents increase and the forward currents decrease. Experimental data presented above [Figure 5.7(b)] and reported data agree with the prediction in the backward bias. However, in the forward bias, we observe the opposite trend with increased magnitude of currents with increasing concentration. The predicted decrease is a result of additional counterions that can electrostatically hinder the movement of OH^- and H^+ ions, resulting in less current.

Hence, the electrostatic screening from the counterions would have more influence on the migration of ions as compared to the electric field attraction from the electrodes. However, we predict that the influence of the counterions may only be significant after a threshold concentration. As such, we observed the opposite trend because we used very small concentrations of ions and so the attraction of the electric field influences the migration more in increased currents. In addition, reverse currents are expected to scale with the inverse of the diode thickness squared. As expected, reported experimental data show that the rectification ratio increases with gel thickness decrease, further providing experimental proof for the electrochemical model. [89] Yamamoto and Doi have not discuss the influence of the scan rate. Nevertheless, it has been shown that as the sweep scan rate increases, the performance of the diode deteriorates. This is due to the delayed response of ions to the applied voltage, which is a drawback for ionotronics.[3]

5.5 Summary

A polyelectrolyte gel diode based on a cellulose nanocrystal-agarose hydrogel which exhibits exceptional performance has been used to explain the mechanism behind the rectification of ionic current. Experimental results have been used to stress-test the electrochemical model proposed by Yamamoto and Doi, i.e., ion formation and transport in forward and backward biases. In conjunction with previously reported MD simulation results, further evidence has been provided

in favor of the electrochemical model, however, few discrepancies between the model and experimental results suggest the furthermore deeper investigation is needed.

First, we have verified that ions are generated at the surface of the electrodes. EIS experiments highlighted the presence of Faradaic current alongside capacitive double layer, proving the existence of redox reactions. Through sweep and step bias experiments, it was shown that the ions formed at the electrodes travel through the media and recombine at the interface. The equilibration of the step bias experiments suggested diffusion constants of 10^{-4}, which coincided with the diffusion constants of OH^- and H^+. The equilibration constant for the diffusing ions was not dependant on the concentration. We also proved that an asymmetric nature in the PGD is fundamental to current rectification, as the PGDs with two similar polarity gels showed no current rectification.

Exponential currents in the forward bias were observed and $J = A\sqrt{-V}$ in the backward bias, which coincided with predictions of the electrochemical model. These findings were similar for low scan rate sweep experiments and step experiments. Additionally, we also confirmed the dependency of the electrochemical model on the dopant concentration in the backward bias regime. We showed that the higher ionization did indeed lead to higher backward bias currents. However, we were not able to confirm the concentration dependency in the forward bias regime, where Yamamoto and Doi make a counter-intuitive claim that higher concentrations lead to lower forward bias currents. This suggests that a more careful analysis is needed with close control of the overpotentials at the surface of the electrodes.

This work contributes to our understanding of how to control ionic movement in ionic devices and points out the important factors that must be considered to improve the performance of such devices. Further work on the subject that may give a more in-depth analysis of the potential profiles in the system would entail using a 3-electrode setup; to monitor the potential changes as well a to achieve control of the overpotentials at the electrodes.

Chapter 6: Conclusions and Recommendation for Future Work

6.1 Conclusions

Modified cellulose nanocrystalline hydrogels were synthesized by Kudzanai Nyamayaro at the Chemistry Department (UBC). These were used to fabricate ionic diodes. The rheological properties of the hydrogels used to fabricate the diodes were studied in detail. The following conclusions can be drawn from this Ph.D. study:

First regarding the physical and rheological properties of the unmodified CNC and modified nCNC and pCNC the following can be concluded. The unmodified CNC has a zeta potential of -41.13 mV due to the negatively charged sulfonate groups introduced on the surface during their production (sulfuric acid treatment). The negative surface charge was increased by increasing the number of sulfonate groups to produce cationic pCNC. After surface modification, pCNCs maintain a negative surface charge and its zeta potential becomes about –50 mV. This resulted in increased electrostatic repulsions and as a matter of fact, increased the colloidal stability of the pCNC. Conversely, the nCNC has a positive surface potential of 44.2mV due to the introduction of quaternary ammonium salts from GTMAC. Due to the reversal of the surface potential, cationic cellulose nanocrystals have significantly different colloidal behaviors compared to the negatively charged CNC.

The rheological properties of the newly synthesized CNCs in suspension were studied as they are critical parameters in the performance optimization of diodes. To produce reproducible and reliable rheological measurements, a pre-shear experimental protocol was established. Before each measurement, pre-shear at a rate of 500 s^{-1} for 1 min was applied to all samples and these were left to recover their equilibrium structure for 30 min. It is important to mention that when deciding a particular pre-shear rate and subsequent recovery time, the material's response in both directions should be considered. This is to ensure the complete elimination of any pre-shear history from viscoelastic materials. If successfully eliminated, the response should be identical in both directions.

The rheological properties of various hydrogels at various concentrations were examined with and without sonication. Sonication is important to be applied in order to break the CNC clusters into

individual fibers to explore the full potential of these charged fibers in stabilizing the fabricated hydrogels through electrostatic repulsion and hydrogen bonding. After sonication, a reduction in linear viscoelastic moduli (G′ and G″) was observed in CNC and pCNC suspensions. On the contrary, the values of G′ and G″ of the sonicated nCNC suspensions increased over the whole range of the frequencies compared to the unsonicated ones. This was found to be due to the stronger hydrogen interactions between the individual fibers that form in the case of the nCNC. These observations were confirmed by linear viscoelastic measurements over a wide range of frequencies.

The newly synthesized cationic and anionic CNCs were used to fabricate a diode. The hydrogels were placed in plastic cases that made the diode, fabricated by 3-D printing using polylactic acid. The current response of the diode upon the application of voltage was investigated and the following conclusions were drawn: First, the current-voltage characteristics of the CNC-hydrogel diode are influenced by concentration, gel thickness, scanning frequency, and applied voltage. Secondly, the fabricated diodes exhibited good rectification performance for frequencies under 10mHz. No breakdown voltage was observed for voltages up to 5V. When the applied voltage was increased, the maximum current in the forward bias increased, although there was also a significant increase in the current in the reverse bias. This results in a decrease in the rectification ratio. Finally, the current-voltage characteristics of the diode were tested over four weeks and these observations indicated the long-term stability and performance of the diode. Overall, the fabricated diodes in this work were demonstrated to outperform (higher rectification ratio) other diodes based on cellulose hydrogels previously reported in the literature.

Last but not the least, the mechanism proposed by the Yamamoto–Doi model was explored using the experimental results of the present thesis in an attempt to validate this theory for the first time in the literature. It was concluded that the diode operates via a physical mechanism that involves the electrochemical generation of proton and hydroxyl ions at the electrodes to generate current. Exponential currents (J) in the forward bias were observed and $J = A\sqrt{-V}$ (with A inversely proportional to the gel ionization and V the potential) in the backward bias, which coincides with predictions of the electrochemical Yamamoto-Doi model. Finally, the dependence of the electrochemical model on the dopant concentration in the backward bias regime was confirmed.

As a general final remark/conclusion, the results of this Ph.D. thesis can be directly utilized to fabricate biodegradable diodes of good, reliable, and stable rectification performance.

6.1 Recommendation for future work

There are several opportunities and challenges in which this work could be continued.

- This study focused on the cationic and anionic CNC with Cl^- and Na^+ counter ions in the system. Investigating the effect of different counter ions on the rheological properties of the CNC suspensions would also be of interest. As the mobility of various ions is different, it is expected that the rectification and dynamic response of such diodes would be affected.

- It would be interesting to study the synergistic effects of various mixtures of pCNC and nCNC in suspension using rheological studies. Such mixtures of positive and negative polyelectrolyte hydrogels are referred to as coacervates which have found many applications lately.

- This study covered the current response of the diode when voltage was applied. It will be interesting to investigate the performance of these hydrogels as sensors based on the piezo-ionic effect i.e., generation of current upon the application of a mechanical force. Additionally, we envision the use of ionic diodes in actual devices such as energy harvesters and sensors. For example, a flexible device capable of converting mechanical energy to electrical energy has been reported in the literature. The device was based on a p–n organic junction diode assembly. As such, we hope that this study can be extended to fabricate similar CNC-based biodegradable devices.

- In this research, ITO (indium tin oxide) is employed as a material for the electrodes in the fabrication of the diodes. Thin films of indium tin oxide are optically transparent and electrically conductive material, but they are not flexible. Therefore, employing conducting polymers like PEDOT: PSS instead of ITO is proposed to extend this work.

- Furthermore, another possible future work would be the development of microchip-based cellulose nanocrystals polyelectrolyte diodes i.e. constructing different logic gates like AND gate and OR gate to produce a single output by making use of ionic diodes.

- Investigation and comparing non-water electrolysis diodes based on ionoelesomer[87] networks or electrode-oxidation[96] with the water electrolysis diodes in terms of their performance and stabilities.

References

(1) Yamamoto, T.; Doi, M. Electrochemical Mechanism of Ion Current Rectification of Polyelectrolyte Gel Diodes. *Nature Communications* **2014**, *5* (May), 1–8. https://doi.org/10.1038/ncomms5162.

(2) Feig, V. R.; Tran, H.; Bao, Z. Biodegradable Polymeric Materials in Degradable Electronic Devices. *ACS central science* **2018**, *4* (3), 337–348.

(3) Chun, H.; Chung, T. D. Iontronics. *Annual Review of Analytical Chemistry* **2015**, *8*, 441–462.

(4) Cayre, O. J.; Suk, T. C.; Velev, O. D. Polyelectrolyte Diode: Nonlinear Current Response of a Junction between Aqueous Ionic Gels. *Journal of the American Chemical Society* **2007**, *129* (35), 10801–10806. https://doi.org/10.1021/ja072449z.

(5) Klemm, D.; Heublein, B.; Fink, H.; Bohn, A. Cellulose: Fascinating Biopolymer and Sustainable Raw Material. *Angewandte chemie international edition* **2005**, *44* (22), 3358–3393.

(6) Chen, C.; Hu, L. Nanocellulose toward Advanced Energy Storage Devices: Structure and Electrochemistry. *Accounts of chemical research* **2018**, *51* (12), 3154–3165.

(7) Zhang, X.; Zhang, W.; Wang, Y.; Deng, Y. Flexible and Transparent Fiber-Based Ionic Diode Fabricated from Oppositely Charged Microfibrillated Cellulose. *Fiber Society 2012 Fall Meeting and Technical Conference in Partnership with Polymer Fibers 2012: Rediscovering Fibers in the 21st Century* **2012**.

(8) Nyamayaro, K.; Triandafilidi, V.; Keyvani, P.; Rottler, J.; Mehrkhodavandi, P.; Hatzikiriakos, S. G. The Rectification Mechanism in Polyelectrolyte Gel Diodes. *Physics of Fluids* **2021**, *33* (3), 32010.

(9) Shafiei Sabet, S. Shear Rheology of Cellulose Nanocrystal (CNC) Aqueous Suspensions. University of British Columbia 2013.

(10) Lenfant, G.; Heuzey, M.; van de Ven, T. G. M.; Carreau, P. J. Gelation of Crystalline Nanocellulose in the Presence of Hydroxyethyl Cellulose. *The Canadian Journal of Chemical Engineering* **2017**, *95* (10), 1891–1900.

(11) Danesh, M.; Mauran, D.; Hojabr, S.; Berry, R.; Pawlik, M.; Hatzikiriakos, S. G. Yielding of Cellulose Nanocrystal Suspensions in the Presence of Electrolytes. *Physics of Fluids* **2020**, *32* (9), 93103.

(12) Ranjbar, D. Rheology and Dye Adsorption of Surfactant-Cellulose Nanocrystal Complexes. University of British Columbia 2019.

(13) Gahrooee, T. R.; Moud, A. A.; Danesh, M.; Hatzikiriakos, S. G. Rheological Characterization of CNC-CTAB Network below and above Critical Micelle Concentration (CMC). *Carbohydrate Polymers* **2021**, *257*, 117552.

(14) Tang, Y.; Wang, X.; Huang, B.; Wang, Z.; Zhang, N. Effect of Cationic Surface Modification on the Rheological Behavior and Microstructure of Nanocrystalline Cellulose. *Polymers* **2018**, *10* (3), 278.

(15) Habibi, Y.; Lucia, L. A.; Rojas, O. J. Cellulose Nanocrystals: Chemistry, Self-Assembly, and Applications. *Chemical reviews* **2010**, *110* (6), 3479–3500.

(16) Le Gars, M.; Douard, L.; Belgacem, N.; Bras, J. Cellulose Nanocrystals: From Classical Hydrolysis to the Use of Deep Eutectic Solvents. In *Smart Nanosystems for Biomedicine, Optoelectronics and Catalysis*; IntechOpen, 2019.

(17) Revol, J.-F.; Godbout, L.; Dong, X.-M.; Gray, D. G.; Chanzy, H.; Maret, G. Chiral Nematic Suspensions of Cellulose Crystallites; Phase Separation and Magnetic Field Orientation. *Liquid Crystals* **1994**, *16* (1), 127–134.

(18) Yu, H.; Qin, Z.; Liang, B.; Liu, N.; Zhou, Z.; Chen, L. Facile Extraction of Thermally Stable Cellulose Nanocrystals with a High Yield of 93% through Hydrochloric Acid Hydrolysis under Hydrothermal Conditions. *Journal of Materials Chemistry A* **2013**, *1* (12), 3938–3944.

(19) Viet, D.; Beck-Candanedo, S.; Gray, D. G. Dispersion of Cellulose Nanocrystals in Polar Organic Solvents. *Cellulose* **2007**, *14* (2), 109–113.

(20) Chen, L.; Wang, Q.; Hirth, K.; Baez, C.; Agarwal, U. P.; Zhu, J. Y. Tailoring the Yield and Characteristics of Wood Cellulose Nanocrystals (CNC) Using Concentrated Acid Hydrolysis. *Cellulose* **2015**, *22* (3), 1753–1762.

(21) Camarero Espinosa, S.; Kuhnt, T.; Foster, E. J.; Weder, C. Isolation of Thermally Stable Cellulose Nanocrystals by Phosphoric Acid Hydrolysis. *Biomacromolecules* **2013**, *14* (4), 1223–1230.

(22) Araki, J.; Wada, M.; Kuga, S.; Okano, T. Flow Properties of Microcrystalline Cellulose Suspension Prepared by Acid Treatment of Native Cellulose. *Colloids and Surfaces A: Physicochemical and Engineering Aspects* **1998**, *142* (1), 75–82.

(23) Zhang, J.; Jiang, N.; Dang, Z.; Elder, T. J.; Ragauskas, A. J. Oxidation and Sulfonation of Cellulosics. *Cellulose* **2008**, *15* (3), 489.

(24) Varma, A. J.; Kulkarni, M. P. Oxidation of Cellulose under Controlled Conditions. *Polymer Degradation and Stability* **2002**, *77* (1), 25–27.

(25) Yu, H.-Y.; Chen, R.; Chen, G.-Y.; Liu, L.; Yang, X.-G.; Yao, J.-M. Silylation of Cellulose Nanocrystals and Their Reinforcement of Commercial Silicone Rubber. *Journal of Nanoparticle Research* **2015**, *17* (9), 1–13.

(26) Hasani, M.; Cranston, E. D.; Westman, G.; Gray, D. G. Cationic Surface Functionalization of Cellulose Nanocrystals. *Soft Matter* **2008**, *4* (11), 2238–2244.

(27) Kan, K. H. M.; Li, J.; Wijesekera, K.; Cranston, E. D. Polymer-Grafted Cellulose Nanocrystals as PH-Responsive Reversible Flocculants. *Biomacromolecules* **2013**, *14* (9), 3130–3139.

(28) Thakur, V. K. *Nanocellulose Polymer Nanocomposites: Fundamentals and Applications*; John Wiley & Sons, 2014.

(29) Domingues, R. M. A.; Gomes, M. E.; Reis, R. L. The Potential of Cellulose Nanocrystals in Tissue Engineering Strategies. *Biomacromolecules* **2014**, *15* (7), 2327–2346.

(30) Barbosa, A. M.; Robles, E.; Ribeiro, J. S.; Lund, R. G.; Carreño, N. L. V; Labidi, J. Cellulose Nanocrystal Membranes as Excipients for Drug Delivery Systems. *Materials* **2016**, *9* (12), 1002.

(31) Fleming, K.; Gray, D. G.; Matthews, S. Cellulose Crystallites. *Chemistry–A European Journal* **2001**, *7* (9), 1831–1836.

(32) Schyrr, B.; Pasche, S.; Voirin, G.; Weder, C.; Simon, Y. C.; Foster, E. J. Biosensors Based on Porous Cellulose Nanocrystal–Poly (Vinyl Alcohol) Scaffolds. *ACS applied materials & interfaces* **2014**, *6* (15), 12674–12683.

(33) Wu, T.; Li, J.; Li, J.; Ye, S.; Wei, J.; Guo, J. A Bio-Inspired Cellulose Nanocrystal-Based Nanocomposite Photonic Film with Hyper-Reflection and Humidity-Responsive Actuator Properties. *Journal of Materials Chemistry C* **2016**, *4* (41), 9687–9696.

(34) Sayed, D. M.; El-Deab, M. S.; Elshakre, M. E.; Allam, N. K. Nanocrystalline Cellulose Confined in Amorphous Carbon Fibers as Capacitor Material for Efficient Energy Storage. *The Journal of Physical Chemistry C* **2020**, *124* (13), 7007–7015.

(35) Qiao, C.; Chen, G.; Zhang, J.; Yao, J. Structure and Rheological Properties of Cellulose Nanocrystals Suspension. *Food Hydrocolloids* **2016**, *55*, 19–25.

(36) Foster, E. J.; Moon, R. J.; Agarwal, U. P.; Bortner, M. J.; Bras, J.; Camarero-Espinosa, S.; Chan, K. J.; Clift, M. J. D.; Cranston, E. D.; Eichhorn, S. J. Current Characterization Methods for Cellulose Nanomaterials. *Chemical Society Reviews* **2018**, *47* (8), 2609–2679.

(37) Marchessault, R. H.; Morehead, F. F.; Koch, M. J. Some Hydrodynamic Properties of Neutral Suspensions of Cellulose Crystallites as Related to Size and Shape. *Journal of Colloid Science* **1961**, *16* (4), 327–344.

(38) Onogi, S.; Asada, T. Rheology and Rheo-Optics of Polymer Liquid Crystals. In *Rheology*;

Springer, 1980; pp 127–147.

(39) Shafiei-Sabet, S.; Hamad, W. Y.; Hatzikiriakos, S. G. Rheology of Nanocrystalline Cellulose Aqueous Suspensions. *Langmuir* **2012**, *28* (49), 17124–17133.

(40) Lee, H.; Kim, C.; Sun, J. Stretchable Ionics–a Promising Candidate for Upcoming Wearable Devices. *Advanced Materials* **2018**, *30* (42), 1704403.

(41) Arbring Sjöström, T.; Berggren, M.; Gabrielsson, E. O.; Janson, P.; Poxson, D. J.; Seitanidou, M.; Simon, D. T. A Decade of Iontronic Delivery Devices. *Advanced Materials Technologies* **2018**, *3* (5), 1700360.

(42) Lee, H.; Kim, C.; Sun, J. Stretchable Ionics – A Promising Candidate for Upcoming Wearable Devices. *Advanced Materials* **2018**, *30* (42), 1704403. https://doi.org/10.1002/ADMA.201704403.

(43) Zhao, R.; Zhang, X.; Xu, J.; Yang, Y.; He, G. Flexible Paper-Based Solid State Ionic Diodes. *RSC advances* **2013**, *3* (45), 23178–23183.

(44) Wang, Z.; Li, H.; Tang, Z.; Liu, Z.; Ruan, Z.; Ma, L.; Yang, Q.; Wang, D.; Zhi, C. Hydrogel Electrolytes for Flexible Aqueous Energy Storage Devices. *Advanced Functional Materials* **2018**, *28* (48), 1804560.

(45) Bisri, S. Z.; Shimizu, S.; Nakano, M.; Iwasa, Y. Endeavor of Iontronics: From Fundamentals to Applications of Ion-Controlled Electronics. *Advanced Materials* **2017**, *29* (25), 1607054.

(46) Yuk, H.; Lu, B.; Zhao, X. Hydrogel Bioelectronics. *Chemical Society Reviews* **2019**, *48* (6), 1642–1667.

(47) Frilette, V. J. Preparation and Characterization of Bipolar Ion Exchange Membranes. *The Journal of Physical Chemistry* **1956**, *60* (4), 435–439.

(48) Simon, D. T.; Gabrielsson, E. O.; Tybrandt, K.; Berggren, M. Organic Bioelectronics: Bridging the Signaling Gap between Biology and Technology. *Chemical Reviews* **2016**,

116 (21), 13009–13041.

(49) Wan, C.; Xiao, K.; Angelin, A.; Antonietti, M.; Chen, X. The Rise of Bioinspired Ionotronics. *Advanced Intelligent Systems* **2019**, 1900073.

(50) Ferro, M. D.; Melosh, N. A. Electronic and Ionic Materials for Neurointerfaces. *Advanced Functional Materials* **2018**, *28* (12), 1704335.

(51) Yang, C.; Suo, Z. Hydrogel Ionotronics. *Nature Reviews Materials* **2018**, *3* (6), 125.

(52) Fuller, T. F.; Harb, J. N. *Electrochemical Engineering*; John Wiley & Sons, 2018.

(53) Zaman, M.; Xiao, H.; Chibante, F.; Ni, Y. Synthesis and Characterization of Cationically Modified Nanocrystalline Cellulose. *Carbohydrate Polymers* **2012**, *89* (1), 163–170.

(54) Kim, U.-J.; Kuga, S.; Wada, M.; Okano, T.; Kondo, T. Periodate Oxidation of Crystalline Cellulose. *Biomacromolecules* **2000**, *1* (3), 488–492.

(55) Lin, N.; Dufresne, A. Surface Chemistry, Morphological Analysis and Properties of Cellulose Nanocrystals with Gradiented Sulfation Degrees. *Nanoscale* **2014**, *6* (10), 5384–5393.

(56) Wang, Z.-M.; Li, L.; Xiao, K.-J.; Wu, J.-Y. Homogeneous Sulfation of Bagasse Cellulose in an Ionic Liquid and Anticoagulation Activity. *Bioresource Technology* **2009**, *100* (4), 1687–1690. https://doi.org/https://doi.org/10.1016/j.biortech.2008.09.002.

(57) Beck, S.; Méthot, M.; Bouchard, J. General Procedure for Determining Cellulose Nanocrystal Sulfate Half-Ester Content by Conductometric Titration. *Cellulose* **2015**, *22* (1), 101–116.

(58) Rietveld, H. M. Line Profiles of Neutron Powder-diffraction Peaks for Structure Refinement. *Acta Crystallographica* **1967**, *22* (1), 151–152.

(59) Rietveld, H. M. A Profile Refinement Method for Nuclear and Magnetic Structures. *Journal of applied Crystallography* **1969**, *2* (2), 65–71.

(60) Lewis, L.; Derakhshandeh, M.; Hatzikiriakos, S. G.; Hamad, W. Y.; MacLachlan, M. J. Hydrothermal Gelation of Aqueous Cellulose Nanocrystal Suspensions. *Biomacromolecules* **2016**, *17* (8), 2747–2754.

(61) Shafiei-Sabet, S.; Hamad, W. Y.; Hatzikiriakos, S. G. Ionic Strength Effects on the Microstructure and Shear Rheology of Cellulose Nanocrystal Suspensions. *Cellulose* **2014**, *21* (5), 3347–3359.

(62) Shojaeiarani, J.; Bajwa, D.; Holt, G. Sonication Amplitude and Processing Time Influence the Cellulose Nanocrystals Morphology and Dispersion. *Nanocomposites* **2020**, *6* (1), 41–46.

(63) Ureña-Benavides, E. E.; Ao, G.; Davis, V. A.; Kitchens, C. L. Rheology and Phase Behavior of Lyotropic Cellulose Nanocrystal Suspensions. *Macromolecules* **2011**, *44* (22), 8990–8998.

(64) Oguzlu, H.; Boluk, Y. Interactions between Cellulose Nanocrystals and Anionic and Neutral Polymers in Aqueous Solutions. *Cellulose* **2017**, *24* (1), 131–146.

(65) Bruel, C.; Tavares, J. R.; Carreau, P. J.; Heuzey, M.-C. The Structural Amphiphilicity of Cellulose Nanocrystals Characterized from Their Cohesion Parameters. *Carbohydrate polymers* **2019**, *205*, 184–191.

(66) Bonn, D.; Denn, M. M.; Berthier, L.; Divoux, T.; Manneville, S. Yield Stress Materials in Soft Condensed Matter. *Reviews of Modern Physics* **2017**, *89* (3), 35005.

(67) Khandal, D.; Riedl, B.; Tavares, J. R.; Carreau, P. J.; Heuzey, M.-C. Tailoring Cellulose Nanocrystals Rheological Behavior in Aqueous Suspensions through Surface Functionalization with Polyethyleneimine. *Physics of Fluids* **2019**, *31* (2), 21207.

(68) Van Den Berg, M. E. H.; Kuster, S.; Windhab, E. J.; Sagis, L. M. C.; Fischer, P. Nonlinear Shear and Dilatational Rheology of Viscoelastic Interfacial Layers of Cellulose Nanocrystals. *Physics of Fluids* **2018**, *30* (7), 72103.

(69) Ranjbar, D.; Hatzikiriakos, S. G. Effect of Ionic Surfactants on the Viscoelastic Properties

of Chiral Nematic Cellulose Nanocrystal Suspensions. *Langmuir* **2019**.

(70) T. Raeisi Gahrooee, A. Abbasi Moud, M. D. and S. G. H. Rheological Characterization of CNC-CTAB Network Below and Above CMC. *Carbohydrate Polymers* **2020**.

(71) Choi, J.; Rogers, S. A. Optimal Conditions for Pre-Shearing Thixotropic or Aging Soft Materials. *Rheologica Acta* **2020**, *59* (12), 921–934.

(72) Rogers, S. A.; Erwin, B. M.; Vlassopoulos, D.; Cloitre, M. Oscillatory Yielding of a Colloidal Star Glass. *Journal of Rheology* **2011**, *55* (4), 733–752.

(73) Rajalaxmi, D.; Jiang, N.; Leslie, G.; Ragauskas, A. J. Synthesis of Novel Water-Soluble Sulfonated Cellulose. *Carbohydrate research* **2010**, *345* (2), 284–290.

(74) Boluk, Y.; Zhao, L.; Incani, V. Dispersions of Nanocrystalline Cellulose in Aqueous Polymer Solutions: Structure Formation of Colloidal Rods. *Langmuir* **2012**, *28* (14), 6114–6123.

(75) Ballauff, M.; Brader, J. M.; Egelhaaf, S. U.; Fuchs, M.; Horbach, J.; Koumakis, N.; Krüger, M.; Laurati, M.; Mutch, K. J.; Petekidis, G. Residual Stresses in Glasses. *Physical review letters* **2013**, *110* (21), 215701.

(76) Rogers, S. A.; Lettinga, M. P. A Sequence of Physical Processes Determined and Quantified in Large-Amplitude Oscillatory Shear (LAOS): Application to Theoretical Nonlinear Models. *Journal of rheology* **2012**, *56* (1), 1–25.

(77) Dimitriou, C. J.; Ewoldt, R. H.; McKinley, G. H. Describing and Prescribing the Constitutive Response of Yield Stress Fluids Using Large Amplitude Oscillatory Shear Stress (LAOStress). *Journal of Rheology* **2013**, *57* (1), 27–70.

(78) Liimatainen, H.; Sirviö, J.; Sundman, O.; Hormi, O.; Niinimäki, J. Use of Nanoparticular and Soluble Anionic Celluloses in Coagulation-Flocculation Treatment of Kaolin Suspension. *Water research* **2012**, *46* (7), 2159–2166.

(79) Jin, E.; Guo, J.; Yang, F.; Zhu, Y.; Song, J.; Jin, Y.; Rojas, O. J. On the Polymorphic and

Morphological Changes of Cellulose Nanocrystals (CNC-I) upon Mercerization and Conversion to CNC-II. *Carbohydrate polymers* **2016**, *143*, 327–335.

(80) Roman, M.; Winter, W. T. Effect of Sulfate Groups from Sulfuric Acid Hydrolysis on the Thermal Degradation Behavior of Bacterial Cellulose. *Biomacromolecules* **2004**, *5* (5), 1671–1677.

(81) De France, K. J.; Hoare, T.; Cranston, E. D. Review of Hydrogels and Aerogels Containing Nanocellulose. *Chemistry of Materials* **2017**, *29* (11), 4609–4631.

(82) Awadhiya, A.; Kumar, D.; Rathore, K.; Fatma, B.; Verma, V. Synthesis and Characterization of Agarose–Bacterial Cellulose Biodegradable Composites. *Polymer Bulletin* **2017**, *74* (7), 2887–2903.

(83) Singh, G.; Chandoha-Lee, C.; Zhang, W.; Renneckar, S.; Vikesland, P. J.; Pruden, A. Biodegradation of Nanocrystalline Cellulose by Two Environmentally-Relevant Consortia. *Water research* **2016**, *104*, 137–146.

(84) Lasrado, D.; Ahankari, S.; Kar, K. Nanocellulose-based Polymer Composites for Energy Applications—A Review. *Journal of Applied Polymer Science* **2020**, *137* (27), 48959.

(85) Dai, L.; Cheng, T.; Duan, C.; Zhao, W.; Zhang, W.; Zou, X.; Aspler, J.; Ni, Y. 3D Printing Using Plant-Derived Cellulose and Its Derivatives: A Review. *Carbohydrate polymers* **2019**, *203*, 71–86.

(86) Le Goff, K. J.; Gaillard, C.; Helbert, W.; Garnier, C.; Aubry, T. Rheological Study of Reinforcement of Agarose Hydrogels by Cellulose Nanowhiskers. *Carbohydrate polymers* **2015**, *116*, 117–123.

(87) Gao, D.; Lee, P. S. Rectifying Ionic Current with Ionoelastomers. *Science* **2020**, *367* (6479), 735–736.

(88) Kim, H. J.; Chen, B.; Suo, Z.; Hayward, R. C. Ionoelastomer Junctions between Polymer Networks of Fixed Anions and Cations. *Science* **2020**, *367* (6479), 773–776.

(89) Nyamayaro, K.; Keyvani, P.; D'Acierno, F.; Poisson, J.; Hudson, Z. M.; Michal, C. A.; Madden, J. D. W.; Hatzikiriakos, S. G.; Mehrkhodavandi, P. Toward Biodegradable Electronics: Ionic Diodes Based on a Cellulose Nanocrystal–Agarose Hydrogel. *ACS Applied Materials & Interfaces, 12(46), pp.52182-52191* **2020**.

(90) Triandafilidi, V.; Hatzikiriakos, S. G.; Rottler, J. Poisson–Boltzmann Modeling and Molecular Dynamics Simulations of Polyelectrolyte Gel Diodes in the Static Regime. *Soft Matter* **2020**, *16* (4), 1091–1101.

(91) Allen, J. B.; Larry, R. F. *Electrochemical Methods Fundamentals and Applications*; John Wiley & Sons, 2001.

(92) Duan, J.; Xie, W.; Yang, P.; Li, J.; Xue, G.; Chen, Q.; Yu, B.; Liu, R.; Zhou, J. Tough Hydrogel Diodes with Tunable Interfacial Adhesion for Safe and Durable Wearable Batteries. *Nano energy* **2018**, *48*, 569–574.

(93) Zhao, Y.; Dai, S.; Chu, Y.; Wu, X.; Huang, J. A Flexible Ionic Synaptic Device and Diode-Based Aqueous Ion Sensor Utilizing Asymmetric Polyelectrolyte Distribution. *Chemical communications* **2018**, *54* (59), 8186–8189.

(94) Han, J. H.; Kim, K. B.; Kim, H. C.; Chung, T. D. Ionic Circuits Based on Poly Electrolyte Diodes on a Microchip. *Angewandte Chemie - International Edition* **2009**, *48* (21), 3830–3833. https://doi.org/10.1002/anie.200900045.

(95) Tamura, R.; Lim, E.; Manaka, T.; Iwamoto, M. Analysis of Pentacene Field Effect Transistor as a Maxwell-Wagner Effect Element. *Journal of applied physics* **2006**, *100* (11), 114515.

(96) So, J. H.; Koo, H. J.; Dickey, M. D.; Velev, O. D. Ionic Current Rectification in Soft-Matter Diodes with Liquid-Metal Electrodes. *Advanced Functional Materials* **2012**, *22* (3), 625–631. https://doi.org/10.1002/adfm.201101967.